Doctoral Thesis

Theoretical and Experimental Study of Hydrodynamic Pair Interactions in Sheet Flow

Imran Saeed

Department of Physics

Ulsan National Institute of Science and Technology

2023

Theoretical and Experimental Study of Hydrodynamic Pair Interactions in Sheet Flow

Imran Saeed

Department of Physics

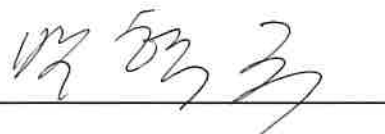Ulsan National Institute of Science and Technology

Theoretical and Experimental Study of Hydrodynamic Pair Interactions in Sheet Flow

A thesis/dissertation submitted to

Ulsan National Institute of Science and Technology

in partial fulfillment of the

requirements for the degree of

Doctor of Philosophy

Imran Saeed

12.01.2022 of submission

Approved by

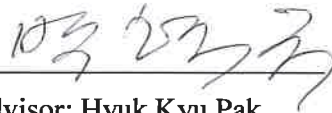_____

Advisor

Hyuk Kyu Pak

Theoretical and Experimental Study of Hydrodynamic Pair Interactions in Sheet Flow

Imran Saeed

This certifies that the thesis/dissertation of Imran Saeed is approved.

12.01.2022 of submission

Signature

Advisor: Hyuk Kyu Pak

Signature

Tsvi Tlusty

Signature

Joonwoo Jeong

Signature

Yoon-Kyoung Cho

Signature

John Thomas King

Abstract

Hydrodynamic interaction between two particles is symmetric at a low Reynolds number uniform flow, creating a hydrodynamic pair. When this pair is sufficiently far from other particles/pairs in the flow it moves with a constant velocity depending on pair length and tilt. In a high concentration of particles, this symmetry is frequently broken due to the presence of other nearby particles, leading to rapid formation/breaking of pairs and high-frequency disturbances in their velocities. Our results show that pair formation dominates the hydrodynamic interaction and controls the spreading of particles both in parallel and perpendicular directions to the background flow. In a continuous medium, pair formation leads to disturbances that propagate as a function of the mean speed of particles. We also study the pair formation dynamics in the regular periodic arrangement of particles in the one-dimensional chain and the two-dimensional square, and triangular geometries with periodic boundary conditions. In the disordered phase, measurements show a sub-population of long-lived particle pairs. Modeling and simulation of the ordered crystalline phase identify the pairs as effective quasiparticles, emerging at the Dirac cones of the spectrum and inducing the melting of the crystal. When the intrinsic threefold symmetry of the hydrodynamic interaction matches that of the crystal, the cones connect to a multicritical, monkey-saddle van Hove singularity, forming a flat band of slow low-frequency excitations whose divergent density drives a sharper melting transition. We compute structure factor, radial distribution, autocorrelation function, and power spectrum evolution in time for these arrangements and compared these with the experiment in which particles flow in microfluidic channels.

Table of Contents

List of Figures

1   INTRODUCTION

Hydrodynamic Interaction (HI) is a specific feature that governs the fundamental dynamics of colloidal and biological systems. Understanding the HI is important for a wide variety of scientific, technological, and biological problems. Colloidal particles, available in the size from a few tens of nanometers to hundreds of micrometers, can be used to model dynamical systems with a wide range of Reynolds and Peclet numbers. In the regime of exceptionally low Reynolds and Peclet numbers, collective dynamics are governed by coupled thermal motions [1], [2]. In sedimenting system or suspension of bubbles carried by external flow at a higher Peclet number, dynamics are governed by the balance between drag force and external force, and HI leads to a net reduction of drag force on the collective motion of particles [3-6]. In a viscous fluid, any small movements of a particle generate a disturbance in the surrounding fluid, which propagates through the fluid, interacts with other neighboring particles, and reflects back and forth thus creating collective interactions. These interactions are long-ranged and arise as a result of a difference in speed between a particle and its surrounding fluid [7], [8]. At an incredibly low Reynolds number, the inertial effect can be neglected in comparison to large viscous forces.

HI among rigid objects immersed in viscous fluid was studied extensively in the early literature [9-13]. Despite many theoretical [14-18] and experimental [1-5] contributions on this topic, most works done so far focus on studying the motion of particles settling under the influence of gravity and the collective Brownian diffusion of a colloidal system in planar geometry without background flow. In comparison, particle motion carried by external flow at a negligibly small Reynolds number has drawn much less attention. The effect of HI on sedimenting particles is opposite to that of flow-driven particles. In the case of free fall, for two nearby spheres falling along the line joining their centers, the drag force on each of them will be smaller and they will become faster compared to a single particle. Similarly, drag reduction for two nearby spheres moving along the line parallel to the external flow will cause them to move slower. The separation between the two spheres does not change until a third sphere approaches nearby and breaks the symmetry between the two particles in the pair. If this happens, one particle in the pair joins the third one creating a new pair, and simultaneously freeing the other one which then moves at a different speed. Studies of thermal diffusion [19-21] of micron-sized particles in a thin quasi-2D channel have shown that due to the long-range HI between neighboring particles, there are markedly different collective motions in the parallel and perpendicular to the separation direction compared with distant particles. It was found that interaction decays as $\frac{1}{r^2}$, and large distance pair interaction is independent of concentration.

Periodic motion for sedimenting particles in the viscous fluid was studied both experimentally [22] and theoretically [23]. HI leads to the attraction between two particles trapped in a ring-like circular

optical trap [24]. The collective motion of colloids trapped in the optical vortex was demonstrated both in experiments [25] and in simulations [26]. A mathematical model based on a two-dimensional stream function was particularly useful in explaining the acoustic phonon-like behaviors observed in the periodic array of water droplets [27-30]. A similar approach explained the wave propagation in the colloid particle system moving on a circular path in a helical optical trap [31]. The sedimentation dynamics of particles are governed by the hydrodynamic interactions between individual particles, the interplay between the dynamics of a small number of particles on the microscopic level, and the collective many-body effects at the macroscopic level. The fundamental difference in HI between sedimenting particles and those carried by fluid flow is that the sedimenting particles with separation parallel to the gravitation direction become accelerated, whereas the external flow-driven particles become decelerated. In a large pool with sufficiently higher Peclet and small Reynolds numbers, collective dynamics are dominated by the symmetric interaction between neighboring particles and the symmetry breaking due to background particles at a microscopic level. When two spheres get sufficiently close to each other, their mutual interaction becomes dominant over the hydrodynamic effects from all other spheres and they experience instantaneous gradients, affecting both the magnitude and direction of their velocities. These gradients are the same for both spheres until they interact with another pair. The separation between two particles of the pair and the separation between two individual pairs are correlated with the density of the medium. In a dense medium, pairs are formed with much shorter inter-particle separations and larger pair-to-pair separations with high-frequency formation/breaking of pairs. While in a dilute medium, interaction occurs slowly, and pairs remain stable for a longer time with larger inter-particle separation and smaller inter-pair separation. These interactions collectively contribute to the dispersion of particles with higher frequencies and shorter wavelengths disturbance in a dense region. Disturbance propagates in the reverse direction to the particle motion at the mean speed of particles. Analysis of a large number of pairs in a big swarm of particles reveals that their correlated motion follows a two-dimensional stream function. The pair parallel to the flow moves slower compared with the pair perpendicular to the flow. Pairs with positive angles move in opposite transverse directions compared to pairs with negative angles.

1.1 Brief historical background

Modern hydrodynamics begins with the Navier-Stokes (1821) equation that describes the flow of fluids. Poiseuille (1838) developed an equation for laminar flow with careful experiments and Stokes (1845) verified Poiseuille's results theoretically. Stokes (1851) linearized the general equation for the motion of viscous incompressible fluid to obtain the time-dependent form of creeping motion. Darcy and Overbeek (1876) extended Stokes' solution for the translation of ellipsoid in viscous fluid parallel to its principal axis. Lambs (1879) provided historical and technical information on the solution of the creeping motion equation [1]. Stitcher (1899) derived the porosity function for beds of uniform spheres

in the flow of water through soil [36]. Lorentz (1896) calculated the motion of a sphere in the presence of a wall using the method of reflection [37]. Ladenburg (1907) determined the effect of a cylindrical tube on the axial motion of a centrally positioned sphere [38]. Cunningham (1910) estimated a decrease in terminal velocity due to particle settling [39]. Einstein (1911) developed a theory for suspension viscosity and showed that the apparent increase in the viscosity of liquid could be related to the volumetric concentration of particles [40]. Oseen (1910) modified Stokes equation of creeping flow by partial inclusion of inertial effects [41]. He pointed out errors in Stokes formulation and provided a solution for a moving sphere in a fluid. Smoulchowski (1912) used the method of reflection to study the sedimentation of an assemblage of spheres and HI between two spheres moving in viscous fluid [42]. Stimson and Jeffery (1918) solved the problem of HI between two spheres analytically [6]. Faxen (1922) correlated the translational and rotational velocities of a spherical particle with force, torque, and stresslet via three equations known as Faxen laws under low Reynolds number creeping flow conditions. Guth and Simha (1936) modified Jeffery's results by considering the wall effect and interaction between particles [43]. Blake (1922) introduced the concept of hydraulic radius for predicting resistance to flow through porous media. Kozeny and Carman (1927) developed a semi-empirical relationship by modifying Blake's formulation. Meksyn (1937) solved Oseen's equation for an elliptical cylinder in a viscous fluid for a small Reynolds number and found that lift and drag curves as a function of the angle of incidence are similar to those of normal aerofoils [44]. Dean (1943) studied the two-dimensional motion of incompressible viscous liquid past a projection [45] by using the conformal mapping technique originally proposed by Muschelisvili to solve the biharmonic equation for stream function. Happel (1958) studied the viscous flow of multiparticle assembly. He assumed random assemblage as a collection of cells, each cell containing a single particle surrounded by fluid and keeping the ratio of particle volume to cell volume the same as the particle density. Due to the interaction with neighboring particles, cells may be distorted but they are assumed to keep a spherical shape [47]. Uchida assumed cubic cells instead of spherical [48]. Miyagi investigated the steady viscous flow passing through an infinite row of parallel cylinders of equal radius based on Stokes equations of motion and made a numerical discussion on the drag coefficient versus the diameter-distance ratio of the row [10]. Hasimoto presented the solution of the Stokes equation for the periodic arrangement of obstacles using the Fourier series analysis. It was found that the ratio of drag force on any one of the obstacles in periodic assembly is larger than for isolated and does not differ much among the three lattice types studied. The same method is applied to a two-dimensional square array of cylinders and drag on one of the cylinders is found to agree with that calculated by using elliptic functions [46]. Happel studied the motion of two spheres falling along the axis of cylinders in the direction parallel to the line joining their centers. Velocities were measured as a function of their center-to-center distance at a low Reynolds number. The experimental results agreed very well with theoretical findings which predicted that two spheres will fall faster than an isolated sphere [11]. Brenner evaluated force on the

wall due to the relative motion of particles and viscous flow confined in the cylinder by applying momentum and energy conservation theorems. He found that finite shearing force exists on the wall, even though it may be infinitely distant from the particles [47]. Segre and Silberg investigated the radial displacement of particles in Poiseuille flow experimentally. They found that macroscopic particles collect into a thin annular region while falling through a straight tube in the laminar regime. The effect is proportional to the tube length, the mean velocity of particles, and the fourth power of the ratio of particle radius to tube radius [48]. Cox and Brenner did a theoretical investigation for the effect of a solid wall on the translation and rotational motion of particles at low Reynolds numbers [49]. They used the method of asymptotic expansion and extended their results to include the general motion of a particle in an arbitrary Stokes field with solid boundaries. O'Neill presented an asymptotic theory to solve the problem of two equal spheres almost in contact and rotating with equal and opposite angular velocities. He discussed the relevance of his results to the free settling of the spheres under the influence of gravity [50]. Batchelor and Green studied HI between two small freely moving spheres of different radii. They evaluated the relative velocity of two sphere centers and force dipole strength as a function of the distance vector separating the two centers [51]. Liron and Mochon gave two alternative solutions for Stokes flow due to force singularity between two parallel plates using an imaging technique and a Fourier transform analysis. They found that force singularity parallel to the wall has far-field behavior of source and image, whereas normal components die out exponentially [52]. The migration velocity of single and pair of spherical particles parallel to plane walls was investigated theoretically by using the singular perturbation technique by Vasseur and Cox. They also performed an experimental investigation of the migration phenomenon by recording the trajectory of spherical particle settling through viscous fluid bounded by vertical walls and found that particles always migrate away from the walls until it reaches an equilibrium position at the axis of the duct [53]. Sangtae Kim presented an analytical solution of Stokes flow past three spheres by using vector harmonics. He extended his theory to a special configuration of N spheres and confirmed the result with experiments [54]. Cichocki and Felderhof proposed an algorithm for the computation of fluid suspension with periodic boundary conditions using Hasimoto's solution of the linear Navier-Stokes equation for point sources located at the lattice point of a simple cubic system [55]. Meiners and Quake reported direct measurement of HI between two microspheres held at varying distances using optical tweezers. They found time-delayed anti-correlation between the positions of two beads and explained it in terms of the standard Oseen equation [56]. Dufresne and his colleagues used the imaging method to measure the collective relative diffusion of two colloidal spheres near a flat plate. They found that the bounding surface modifies the sphere-sphere dynamics even at large separations [57].

1.2   Recent studies

During the last century, there has been a lot of research on HI between spheres (whether falling under gravity, thermal diffusion, or held together as a fixed obstacle to external viscous flow at creeping conditions). The mode of research has changed a lot from the complicated analytical solutions of Stimson and Jeffery to simpler imaging velocimeter techniques. However, research in the field has remained full of new surprises. Instead of large ducts and cylinders, experimentalists have now started to use microfluidic channels and lab-on-a-chip devices to study these interactions [57-60]. This has allowed using a thin planar 2D flow inside which interactions are tractable and strongly coupled [30]. It has been found that interaction in 2D flows produces rich, many-body, and long-range interactions that scale like $\frac{1}{r^2}$ [21]. On the theoretical side, this has let the researcher describe Stokes flow in terms of much simpler 2D potential flow and stream functions instead of Oseen tensors and asymptotic expansions [45]. Tlusty and his colleagues have applied the symmetric hydrodynamic interaction between two spheres to phonon-type vibration between a periodic arrangement of particles carried by external flow [26-30]. Darnton and his colleagues proposed that the Navier-Stokes equation in 2D low Reynolds number flow has two distinct solutions, one valid for deep curtain and the other applicable to thin wide flow [45]. Boaz and Cronin used the optical trap technique to measure micro-meter velocity fields in fluid flow. The result was validated by comparison with independent video-based measurements and applied to obtain the velocity map of the flow field past a microscopic wedge [50]. Direct measurement of HI between two colloidal spheres has shown that the time scale for this interaction is much shorter compared to the vorticity diffusion time scale and it develops on a sonic time scale [34]. Reichart and Stark studied the dynamics of microspheres trapped in optical vortices by holographic optical traps and found that most unstable modes converge into limit cycles which can be explained by the formation of particle doublets [26]. Video microscopy study of the Brownian motion of microspheres suspended in water and confined between two plates revealed that the pairs exert anti-drag on one another when moving perpendicular to the line joining their centers. At large distances, the pair interaction is found to be independent of particle concentration which can be explained on the basis dipolar form of flow induced by the particle motion [20]. Short-time dynamics of quasi-two-dimensional geometries showed that dynamic structure factor, hydrodynamic function, and diffusion coefficients are related in the same manner as their three-dimensional counterparts [14]. Jezewskaa and Felderhof performed a theoretical study on the sedimentation of particles in periodic boundary conditions with three particles per unit cells of a simple cubic lattice [23]. The emergence of collective normal vibrational modes in a one-dimensional microfluidic crystal of water in oil droplets is observed. These phonons were the result of symmetry breaking of the flow field which induces long-range interaction [27]. The range of coupling for colloids confined in a thin sheet is found to increase dramatically compared with bulk fluid. At a distance of about a hundred radii, the mobilities for rigid

and relative motions differ by a factor of 2, whereas in bulk they are practically indistinguishable [61]. Simulation of solid spheres in regular square arrays bounded by parallel walls revealed the propagation of particle displacement waves, deformation, and rearrangements of particle lattice [32]. Hydrodynamic pair attractions are reported for colloidal particles driven through the water along a circular path by an optical ring. A simple analytical model explains that the curvature of the optical ring breaks the symmetry of HI, resulting in particle pairing [24]. Pairing interaction in these traps can be tuned experimentally. Even though these systems are overdamped, HI and driving optical forces give rise to non-decaying excitations and collective modes reflect the fluctuation of particle pairs [62]. An optical technique for the manipulation of complex collective behavior of hydrodynamically coupled micro-particles is presented by Kimura [25]. The effect of particle activity on the emergence of collective modes in linear chains is analyzed through the simulation method. It is found that particle activity induces a new mode of instability that can persist within the limit of large background flow or vanishingly small activity [33].

1.3 Outline of thesis

This work started as a continuation of Professor Tsvi's findings of one-dimensional phonons [27] in a chain of water-droplets carried by external flow in the microfluidic channel. We were looking to find similar effects by using solid microspheres with or without periodic arrangements. It was known to us that the symmetric nature of forces in hydrodynamic interactions causes two particles forming a Hydordynamic Pair to exert the same force on each other, and the pair should remain stable. Therefore, if we observe particles carried by external flow for a long time we will certainly find a considerable number of pairs moving following the two-dimensional stream function. Experiments for tracking the pair interactions were quite successfully and we observed that pairing is the dominant mode of interaction. Next, we wanted to set up initial conditions experimentally and let the ensemble evolve in time. We designed an optical trap with a spatial light modulator to trap many particles for this purpose. However, it was found that trap forces are too weak to hold the moving particles together for a long enough time before any reasonable uniform flow can be achieved in the microfluidic channel. At best we were only able to study two-particle interactions by using an optical trap, and even in that experiment drag force was provided by moving the stage and not by external flow, while keeping the particles trapped at the mean position close to each other. Therefore, we switched to computational approaches for the ordered arrangements and studied the random phase only in experiments.

We present experimental and simulation results for HI between particles carried by external flow in a planar geometry, at a Reynolds number small enough such that the effects of inertial momentum transfer are ignored and a Peclet number large enough such that thermal diffusion can be ignored. In Chapter 2, a basic theoretical approach to the problem is presented. The complex velocity

potential function is used to describe the flow field generated by N-particles and a simultaneous solution of N-coupled equations gives the velocity field at each particle position that governs the collective motion of particles. Dispersion relations for 1D and 2D arrangements of particles are derived. These formulations are used to deduce the analytical density of states, the group velocity of hydrodynamic phonon, and van Hove singularities points. Next, we explained the methodology of simulation and analysis, computation of radial distribution function, structure factor, autocorrelation function, dispersion relation, and density of states. A comparison is made between square, triangular, and random geometries of particles in two-dimensional arrangements with periodic boundary conditions. Density variation in experimental and computational flow is analyzed using FFT. We observed that density variation in 2D-flow follows the dispersion relation similar to 1D crystal. Chapter 3 introduces the concepts of quasiparticles and flat bands in hydrodynamics using the Schrodinger equation for the hydrodynamic phonon in the quasi-2D assembly of particles. It is found that the Hamiltonian operator H_k can be written as a linear combination of Pauli matrices. Eigenvectors and eigenvalues of the Schrodinger equation are used to derive the dispersion relation for hydrodynamic interaction. The formulations are then applied for the hydrodynamic interactions in square and hexagonal lattices. The dispersion spectrum of all interactions is analyzed and compared with the spectrum of nearest-neighbor interaction. Dirac points, van Hove singularities, and the density of states for each type of lattice are discussed. The melting of hydrodynamic crystal is analyzed by computing the time-dependent structure factor, radial distribution functions, and mean square deviations of the crystal. Finally, we introduce the pair-induced melting and propagation of Mach cone in hydrodynamic crystal. Chapter 5 explains the numerical algorithm for the simulation and analysis of particles in square and triangular geometries. Fourier's analysis, particle tracking, structure factor, and radial distribution function are studied. Derivations of two-dimensional stream function for circular boundaries in external flow, dispersion relation, and matrix form for perturbation in velocities of a 1D chain of particles are given in Appendix.

2   METHODOLOGY

2.1   Theoretical model

In a three-dimensional unbounded flow of near-zero Reynolds number, the hydrodynamic drag force on a sphere of radius R is given as $\mathrm{F} = -6\pi\mu R U_p$. In the case of more than one particle in a sheet-like channel, we need to consider two additional effects, one from the boundaries and the other from the hydrodynamic interactions among constituent particles. The drag force on each particle from the background flow is balanced by the friction due to the channel floor and ceiling. The flow field from each particle can be represented by the infinitesimally separated source and sink called a hydrodynamic dipole. The complex velocity potential function describing the flow field generated by n-particles can be represented as a summation of n-complex velocity potential functions. A simultaneous solution of n-coupled equations will give the potential function of each particle and can explain the collective motion of particles.

A circular boundary in 2D flow can be represented as a combination of a hydrodynamic dipole and a uniform stream. The complex potential w at point z for a single pair of source and sink separated by $2d$ in x direction with the same strength m in a uniform stream of velocity U is written as [1]

$$w = \phi + i\psi = Uz - m\ln(z - d) + m\ln(z + d) \tag{2.1}$$

Here, ϕ is a velocity potential and ψ is a stream function. This gives rise to an elliptically closed streamline surrounding the source and sink [2] on which the flow field from the source-sink combination cancels out the contribution from the background flow. In the limit of $d \to 0$, there is a closed (circle) streamline with a radius $R \equiv \sqrt{\frac{2md}{U}}$ and the corresponding stream function at position $r \geq R$ can be written as

$$\psi = Uy - \frac{UR^2 y}{x^2 + y^2} \tag{2.2}$$

This stream function represents a fixed circular boundary with a radius R in uniform flow and can be used to represent circular particles in sheet flow. The corresponding velocity components can be written as

$$u_x = \frac{\partial \psi}{\partial y} = U - \frac{UR^2(x^2 - y^2)}{(x^2 + y^2)^2} = U - \frac{UR^2 \cos(2\theta)}{r^2} \tag{2.3}$$

8

$$u_y = -\frac{\partial \psi}{\partial x} = -\frac{UR^2(2xy)}{(x^2+y^2)^2} = -\frac{UR^2 \sin(2\theta)}{r^2} \tag{2.4}$$

This is the velocity field in the reference frame of the center of a particle with a radius R. If an isolated particle moves with a relative velocity $u_{iso} = KU$, the velocity field in the reference frame of the background flow is

$$u_x = -\frac{U(1-K)R^2 \cos(2\theta)}{r^2} \tag{2.5}$$

$$u_y = -\frac{U(1-K)R^2 \sin(2\theta)}{r^2} \tag{2.6}$$

In the case of two nearby identical particles with radius R separated by distance r, due to the invariance of Eq. (2.5) and (2.6) under the reflection with respect to the center of two-particle positions, two particles feel the same hydrodynamic field from each other. The velocity field felt by each particle due to the presence of the other particle should be multiplied by the friction balance coefficient K and add the isolated velocity u_{iso} to the above result.

$$u_{1x} = u_{2x} = u_{iso} + Ku_x = u_{iso} - \frac{u_{iso}(1-K)R^2 \cos(2\theta)}{r^2} \tag{2.7}$$

$$u_{1y} = u_{2y} = Ku_y = -\frac{u_{iso}(1-K)R^2 \sin(2\theta)}{r^2} \tag{2.8}$$

Since the interaction between two-nearby particles is a function of the separation and the angle only, the pair oriented perpendicular (parallel) to the flow will move faster (slower) than the mean speed of an isolated particle u_{iso}.

For the n-particle system, Eq. (2.7) and (2.8) can be generalized as

$$u_{ix} = u_{iso} - \sum_{j \neq i}^{N} \frac{c_o \cos(2\theta_{ij})}{r_{ij}^2} \tag{2.9}$$

$$u_{iy} = -\sum_{j \neq i}^{n} \frac{c_o \sin(2\theta_{ij})}{r_{ij}^2} \tag{2.10}$$

where $c_o = u_{iso}(1-K)R^2$.

For a one-dimensional chain of n particles in which $u_y = 0$ and $\cos(2\theta_{ij}) = 1$, Eq. (2.9) can be written as

$$u_{ix} = u_{iso} - \sum_{j \neq i}^{N} \frac{c_o}{(x_i - x_j)^2}. \tag{2.11}$$

The central particle in the chain will move forward at a speed

$$u_c = u_{iso} - \frac{c_o}{a^2} \left[\frac{1}{(n-1)^2} + \cdots + \frac{1}{2^2} + 1 + 0 + 1 + \frac{1}{2^2} + \cdots + \frac{1}{(n-1)^2} \right] \tag{2.12}$$

In the limit of $n \to \infty$,

$$u_c = u_{iso} - \frac{c_o}{a^2} \left(\frac{\pi^2}{3} \right) \tag{2.13}$$

Therefore, due to the hydrodynamic interaction among the particles, the 1D chain moves slower than the isolated particle and the net drag effect decreases with the number density of particles, known as collective drag reduction or peloton effect. Equations (2.9) and (2.10) have been previously used to explain the hydrodynamic phonons in the microfluidic crystal [27], simulating the dynamics of a regular array of spherical particles [32], and modeling the collective behavior of active particles in the one-dimensional chain[33].

For the simulation of HI between particles, there are the basic two assumptions: HI occurs in zero time irrespective of the mutual separation of particles, and in the absence of HI all particles will move with the same velocity i.e., u_{iso}. To meet the first assumption, the Reynolds number (Re) for the flow is very small($< 10^{-3}$) such that vorticity diffusion time [34] $\frac{l^2}{v}$ is significantly shorter than the inertial momentum transfer time $\frac{l}{u}$. To meet the second assumption, the Peclet number (Pe) for the flow must be large enough so that thermal effects cannot overtake HI, but not too large so that the inertial momentum transfer becomes a dominant factor. In this sense, we limit the flow parameters at Pe >10 and Re $<10^{-3}$. Figure 2.1 shows the Peclet number and average speed of particles depending on the Reynolds number for various particle radii. According to this, particles with radii larger than $20\mu m$ should move slower than 40µm/sec, and a sphere with radii smaller than $0.5\mu m$ should move faster than 10µm/sec. Furthermore, the above approximation assumes that all particles are of essentially the same size, equidistant from the floor and ceiling of the channel, and undergo the same resistive force characterized by constant friction coefficient K.
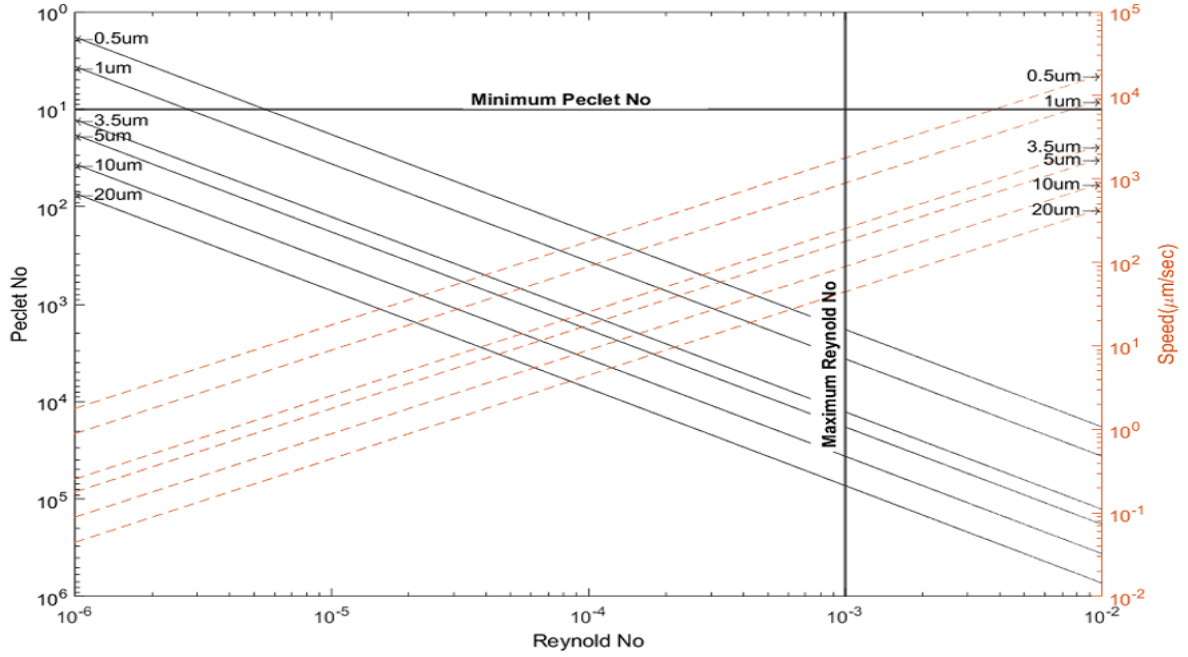
Figure 2.1. *Peclet number (black lines) as a function average speed (orange lines) of particles depending on Reynolds number for various particle radii in aqueous solution at room temperature.*

2.2 Dispersion relation for the 1D chain of particles

Hydrodynamic interaction among particles with the periodic arrangement in flow leads to hydrodynamic phonons. Due to the symmetry of $f(-r) = f(r)$ in the hydrodynamic interaction, a possible wave equation for these phonons is a first-order wave equation written as [30]

$$\zeta \frac{\partial A(x,t)}{\partial x} = \mu \frac{\partial A(x,t)}{\partial t} \tag{2.14}$$

Here, ζ is the drag coefficient and μ is the friction coefficient for particles.

For a chain of n-particles with an average inter-particle distance of a in the direction of the flow, HI among particles leads to a hydrodynamic phonon. Adding small fluctuation δx_{ij} to each inter-particle distance x_{ij}, in the moving frame of reference with constant velocity u_{iso}, $x_i = \mathrm{x}_i + \delta x_i$, $x_{ij} = \mathrm{x}_{ij} + \delta x_{ij}$ and $y_{ij} = 0$, Eq. (2.9) becomes

$$u_{ix} = \dot{x}_i + \delta \dot{x}_i = -c_o \sum_{j \neq i}^{n} \frac{\left(x_{ij} + \delta x_{ij}\right)^2 - y_{ij}^2}{r_{ij}^4} \tag{2.15}$$

For an infinite one-dimensional chain with periodic separation, $r_{ij} = x_{ij} = ja$, $y_{ij} = 0$, and each δx_{ij} can be written in terms of n-nearest neighbors of ith particle.

$$\delta \dot{x}_i = -\sum_{j \neq i}^{n} \frac{2c_o x_{ij} \delta x_{ij}}{r_{ij}^4} = -\sum_{j=1}^{\frac{n}{2}} \frac{2c_o(\delta x_{i-j} - \delta x_{i+j})}{j^3 a^3} \tag{2.16}$$

By substituting the plane wave solution into the above equation for small-amplitude fluctuations with $\delta x = A(x,t) \propto \exp[i(kx - \omega_x t)]$, one can get the following equation

$$\omega_x(k) = \frac{6C_s}{\pi^2 a} \sum_{j=1}^{n} \frac{\sin(jka)}{j^3}, \qquad \text{where} \quad C_s = \frac{2\pi^2}{3} \frac{c_o}{a^2} \tag{2.17}$$

This dispersion relation explains the existence of hydrodynamic phonons for the 1D periodic particle system which is analogous to the acoustic phonons in a 1D confined crystal. The dispersion relation for perturbation along the y-direction can be derived with a similar approach.

$$\omega_y = \frac{6C_s}{\pi^2 a} \sum_{j=1}^{n} \frac{\sin(jka)}{j^3} \tag{2.18}$$

After the Fourier series expansion of the above expressions, the dispersion relations in longitudinal and transverse directions can be obtained, respectively, as follows (see Appendix II for details).

$$\omega_x = \omega_y = k\left(1 + 2\left(\frac{k}{2\pi}\right)^2 - 3\left(\frac{k}{2\pi}\right)\right) \tag{2.19}$$

2.3 Finite Particle Interaction in 1D chain

It is important to understand HI between a finite number of particles before we study the more complicated collective dynamics. The two-fold symmetry of HI implies that the dipolar force is invariant under parity, $f(-r) = -f(r)$. Thus, the hydrodynamic forces that a pair of particles exert on each other are equal, and isolated pairs should therefore be stable (Fig. 2.2 b). The mean speed and its direction for the two-particle system are determined by their mutual separation and inclination. The pair will remain stable until it encounters a third particle. In the three-particle system in which the line connecting the particle centers is parallel to the flow direction, we can modify Eq. (2.11) to the relative speed of particles

$$u_{x_{12}} = c_o \left(\frac{1}{(x_{12}^2 + x_{23}^2)^2} - \frac{1}{x_{23}^2} \right) \qquad (2.20)$$

$$u_{x_{23}} = c_o \left(\frac{1}{x_{12}^2} - \frac{1}{(x_{12}^2 + x_{23}^2)^2} \right) \qquad (2.21)$$

Here, $u_{x_{12}} = u_{x_2} - u_{x_1}$ is the difference in speed between particle 2 and particle 1. For the flow direction from particles 1 to 3, $u_{x_{12}}$ is always negative and $u_{x_{23}}$ is always positive independent of initial conditions implying that the center particle moves toward the first particle forming the pair, thereby isolating the third particle (Fig. 2.2c). Following the same approach, we can write down three equations for the relative speeds of a four-particle system (Fig. 2.2 d). In this case, two pairs are formed and the distance between these two pairs increases in time. Therefore, two pairs

(a) Single particle will move slower than background flow and appear to move toward the right in moving frame at fluid velocity in left direction.

(b) Two particles with the same speed keeping the inter-distance, but slower than the single particle case.

(c) Central particle in **Three** particles case moves slowest until it become in contact with first particle forming pair, which than moves slower than isolated third particle.

(d) In **four** particles case, an upstream pair will continue to move away. If it is located downstream, it will reach central particle and shift to upstream like three particles case. Every other scenario will also unfold in the same manner.

Figure 2.2. Formation of pairs with finite number of particles in a 1D linear chain driven by uniform flow in rightward direction.

continue to move away from each other and behave like two isolated pairs. In the case of systems of more than four particles, particles upstream form pairs with smaller pair-lengths (distance between two particles forming the pair) and with increasing distance between neighboring pairs over time, whereas those in the downstream region form pairs with larger pair-lengths and smaller inter-pair distance. If we consider a chain of N-particles with periodic boundary conditions such that the last particle in the chain can see the first particle of the chain, particles in the chain will start oscillating between the isolated and pairing positions leading to one-dimensional phonons. This oscillating character of the

chain can be visualized for as small as three particles' interactions and is not limited to linear one-dimensional interactions, but has been also observed experimentally for particles confined to move on the circular path in optical vortex [24-26].
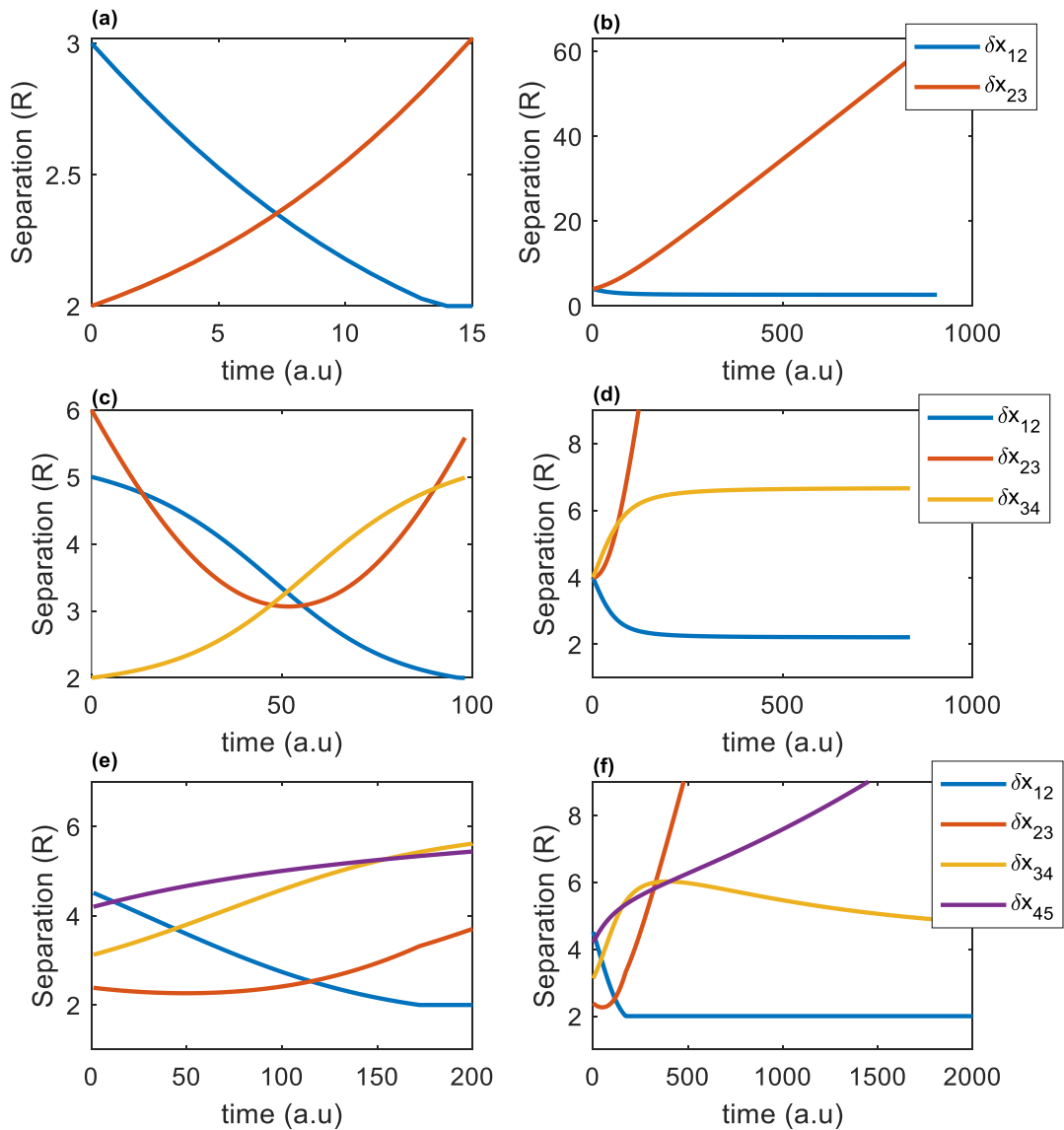
Figure 2.3. *Relative separations between finite number of particles as a function of time starting with different initial conditions. (a-b) Short and long-time behaviours for three particles with different initial conditions at t=0. Pair is formed only between particle 1 and 2. (c-d) Short and long-time behaviours for four particles with different initial conditions at t=0. Two pairs are formed, particles 1, 2 have a smaller inter-particle separation and moving slower than the pair formed by particles 3, 4. (e-f) Short and long-time behaviours for five particles. Here, curves are independent of the initial position of particles.*

2.4 One-dimensional chain of particles

Hydrodynamic interaction between particles in periodic arrangement of particles forming a 1D linear chain in the flow direction leads to phonon [27]. We have analyzed the motion of particles in a 1D chain of particles for a variety of periodic separations/random arrangements of the particles. We used periodic boundary conditions such that the last particle in the chain is connected to the first particle. Hard boundary conditions are used to prevent the particles from overlapping. Data analysis is made using both the Eulerian and Langrangian approaches. It is found that conversion from the Eulerian approach to the Langrangian approach can be made by subtracting the mean speed of particles. An interesting feature of the Eulerian approach is that group velocity is not zero anywhere along the dispersion curve. This implies that there are no singularities in the density of states when viewed by a stationary observer. The relative separation between immediate neighbors $\delta x_i(x_i, t_i) = x_{i+1}(t_i) - x_i(t_i)$ can be calculated as a function of position x_i and time t_i. Figure 2.4 a-b shows the dispersion curve obtained from the
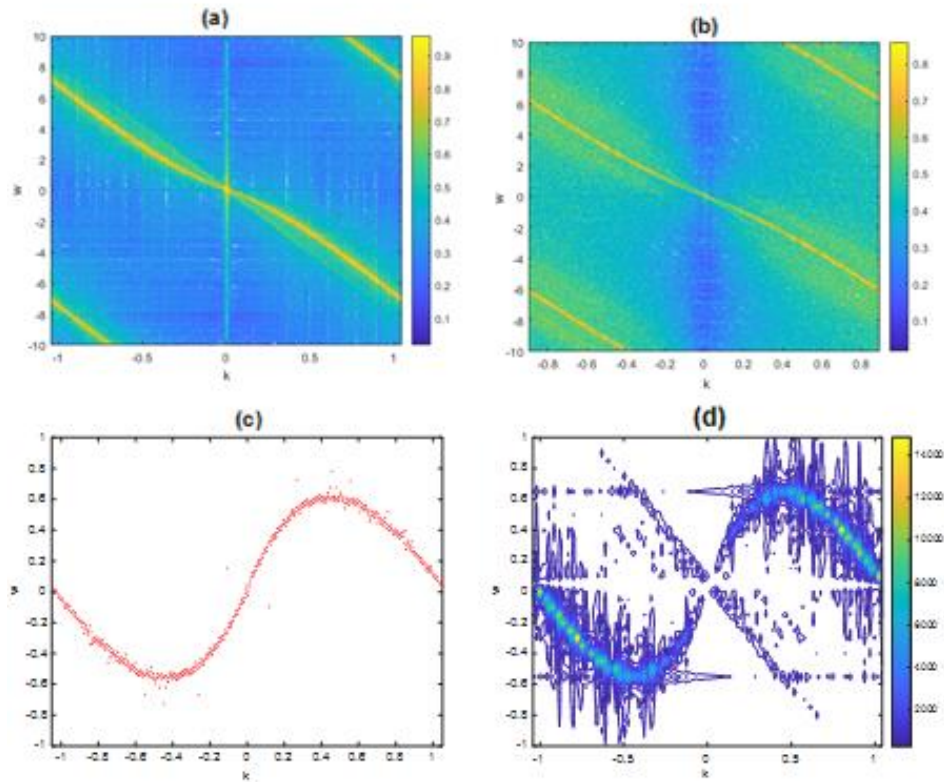
Figure 2.4 *Dispersion for 1D chain in a Eulerian and Langrangian frame. (a) Using relative separation δx_{ij} (x_{ij}, t_i) in Eulerian frame with $j = i + 1$. (b) Calculated by dividing the field of view into length segments of size a, and counting number density of particles in each segment $\rho(x, t)$. (c) Dispersion computed using $\omega_m = \omega_s - Ck$. (d) Dispersion in Langrangian frame.*

power spectrum of the relative separation between particles as they traverse the stationary field of view. The dispersion curve of ω vs. k remains symmetric about the central line $\omega = -Ck$ independent of

particle separation, size, and concentration. The slope of the central line C is found to change only with the speed of an isolated particle u_{iso}. The dispersion relation for the moving frame in Eq. (2.17) can be obtained by using the relation $\omega_m = \omega_s - Ck$, (Fig. 2.4 c-d). As the mean periodic distance a is increased, the sinusoidal contribution decreases becoming a linear line, corresponding to the state that HI occurs only between the nearest neighbors and the majority of particles form pairs. In each quasi-isolated pair fluctuations in interaction lead to continuous formations and breakups of pairs.

2.5 Finite number of particles in a square lattice

Hydrodynamic interaction between particles arranged in the square lattice is simulated to visualize its effect on the collective motion of particles. Equations (2.9) and (2.10) are modified to find the relative velocity of particles.

$$u_{x_{ij}} = \sum_{k \neq i,j}^{n} c_o \left(\frac{(y_{ik}^2 - x_{ik}^2)}{(x_{ik}^2 + y_{ik}^2)^2} - \frac{(y_{jk}^2 - x_{jk}^2)}{(x_{jk}^2 + y_{jk}^2)^2} \right) \tag{2.22}$$

$$u_{y_{ij}} = \sum_{k \neq i,j}^{n} 2c_o \left(\frac{y_{ik} x_{ik}}{(x_{ik}^2 + y_{ik}^2)^2} - \frac{y_{jk} x_{jk}}{(x_{jk}^2 + y_{jk}^2)^2} \right) \tag{2.23}$$

Here, $c_o = u_{iso} R^2 (1 - K)$. New positions of the particles can be systematically updated after each time step of dt with respect to any arbitrary reference particle which itself is moved with speed calculated by Eqs. (2.21) and (2.22). Choosing $dt \leq \frac{R}{u_{iso}}$ makes the above calculation invariant to the choice of u_{iso}. By measuring the separations in units of R, the analysis becomes dimensionless and can be applied to particle motion of any size and speed as long as they experience the same resistance due to the channel. To avoid particles from penetrating each other in the simulation, we used the hard boundary constraints

$$\begin{aligned} x_{ij}(t + dt) &= u_{x_{ij}}(t)dt + x_{ij}(t) \\ y_{ij}(t + dt) &= u_{y_{ij}}(t)dt + y_{ij}(t) \end{aligned} \qquad \begin{cases} x_{ij} \geq 2R\cos\theta_{ij} \\ y_{ij} \geq 2R\sin\theta_{ij} \end{cases}$$

We analyzed the pairing effects in the moving crystal by dividing the field of view into three regions (Fig. 2.5) and measured the first neighbor distance and inclination (tilt angle) in each region with time. At $t = 0$, all particles are distributed in the central region. As time goes on, due to the hydrodynamic interactions particle system expands into left and right regions. Simulation is repeated for a wide range of initial conditions, highly ordered to a random arrangement and high density to extremely low density. The long-time behavior of particle assemblies was found to remain independent of the initial conditions.

The density of particles (Fig. 2.6), mean pairs length, and inclination in three regions saturate around a fix that is independent of initial periodic separation. A similar analysis was conducted by E. Wajnryb et al. [32] for square lattice and observed the propagation of displacement waves, deformation, and rearrangement of particles. They found that the system (Fig. 2.7) develops striking structural features, several rows of particle pairs separate from the main body of the array, forming a shape similar to airplane wings. The front part of the array has an approximately hexagonal particle ordering, and the middle part retains the square ordering. The rear part has a square particle arrangement but with a different orientation than the original one. An unbounded lattice will expand indefinitely until the collective interaction between particles is reduced effectively to the two-body interaction.
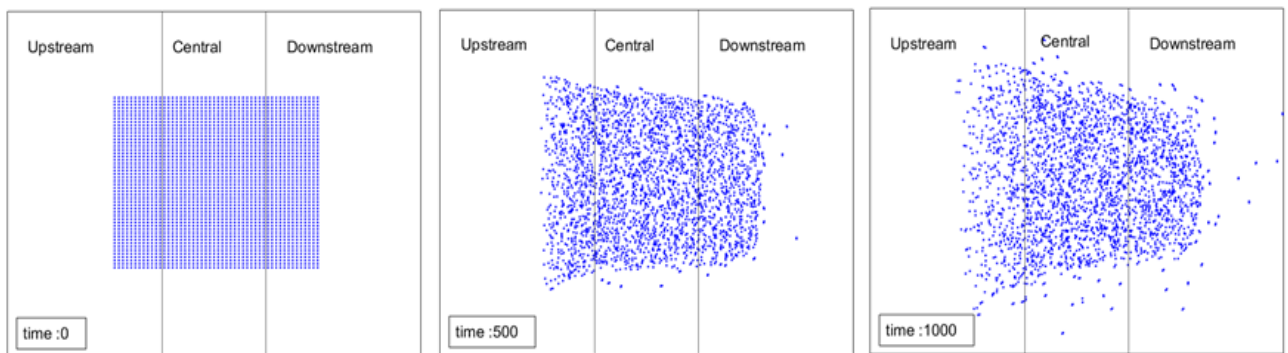
Figure 2.5. *Simulation result for finite square lattice in unbounded conditions. Pairs in upstream region are mostly parallel to flow and those in downstream region are mostly vertical, tilt angle and pair length in three regions become in equilibrium with time depending on density of particles.*
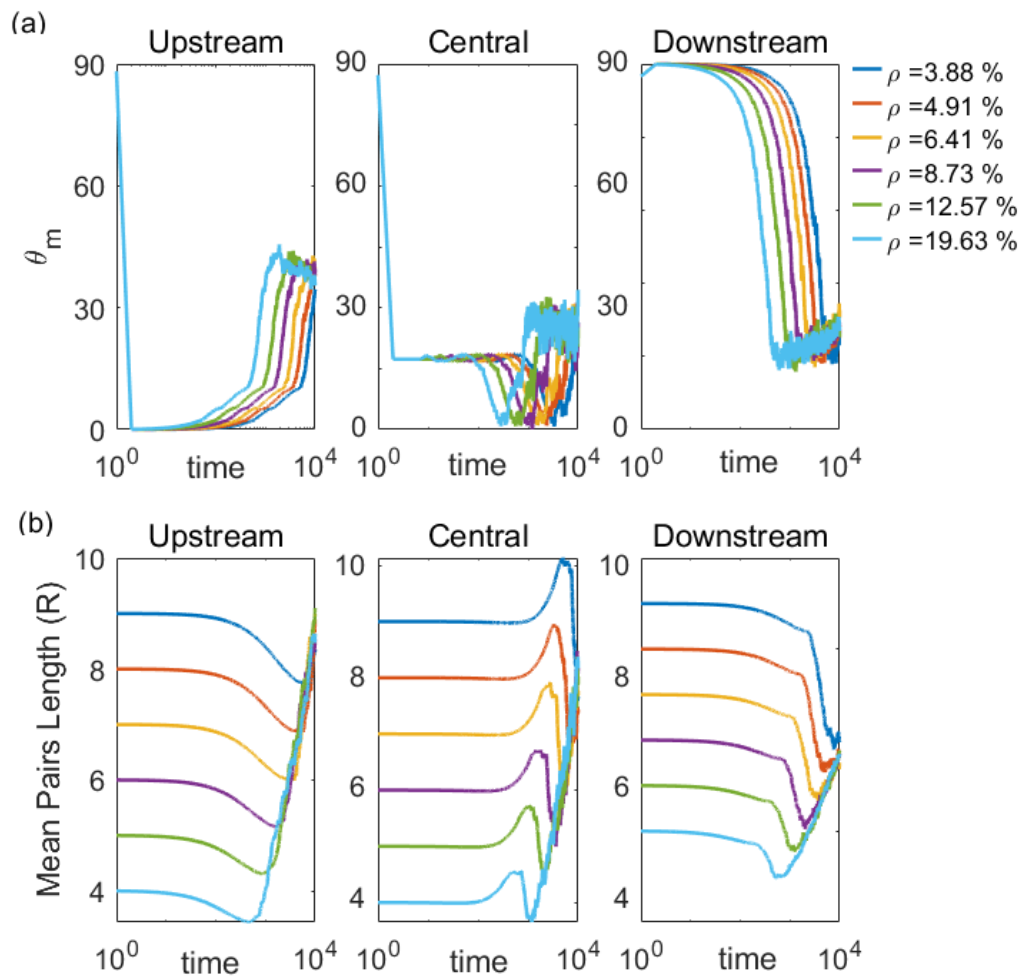
Figure 2.6. *Comparison of particles' relative distance and tilt in the simulation of finite square lattice. After finite transient period mean pairs tilt angle and length equilibrate in three regions. Long-time behaviour of interactions remains independent of initial density and arrangement of particles.*
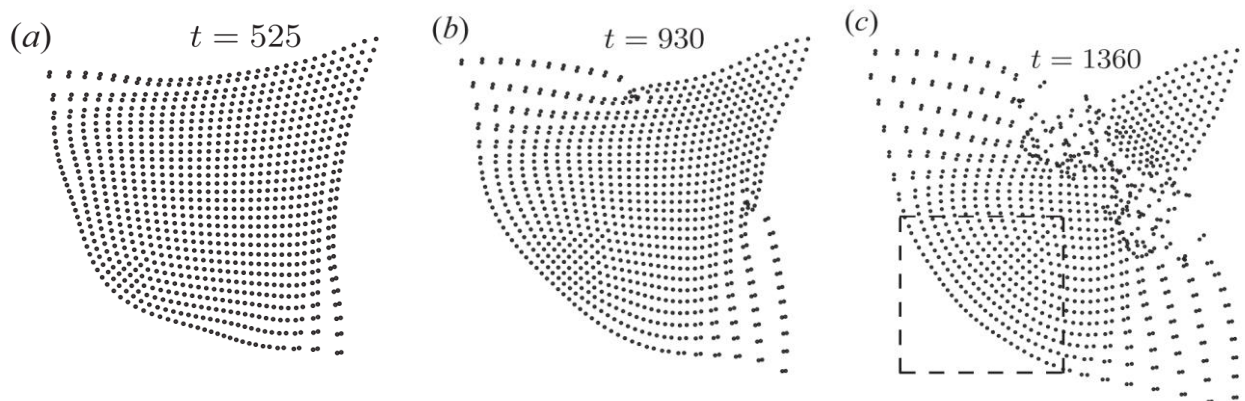
Figure 2.7. *Evolution of a force-driven square array of $N=961$ particles, moving in the diagonal direction. Channel width $H/d=1.1$ and initial particle spacing $W/d=5$. Simulation result [32]*

2.6 Density Waves in continues stream of particles

The motion of particles carried by external flow at approximately uniform density was analyzed using Fourier methods. We recorded the motion of particles for a long time in a fixed frame, which is divided into a small number of length segments (Fig. 2.8 a), and density variation across each length segment is computed. Fourier spectrum for the density variation (Fig. 2.8b-c) shows peaks forming on the line $\omega = -Ck$. The slope C of this line is found to be equal to the mean speed of particles. The dispersion relation for the moving frame (Fig. 2.8 d-g) can be reproduced by using the relation $\omega_m = \omega_s - uk$. These curves are fitted with a single fitting parameter $C_s \sim 0.31u$. This value corresponds to the difference in mean speeds for pairs moving in the opposite direction due to inclination angles with the flow direction. Pairs with an inclination angle between $-\pi/4$ to $\pi/4$ move slower then u_{iso} with maximum speed when they are within touching distance range. Therefore, mean speed can be written as

$$\bar{u} = -\frac{u_{iso}(1-K)R^2}{4R^2}\left[\frac{2}{\pi}\int_{-\frac{\pi}{4}}^{\frac{\pi}{4}}\cos(2\theta)\,d\theta\right] = -\frac{1}{2\pi}u_{iso}(1-K) \tag{2.24}$$

Pairs with the angle between $-\pi/2$ to $-\pi/4$ and $\pi/4$ to $\pi/2$ move faster than u_{iso} with average value $u_{iso} + \frac{1}{2\pi}u_{iso}(1-K)$. Therefore, the relative speed of traveling density waves is $\frac{1}{\pi}u_{iso}(1-K)$. These results are also verified by the computer simulation for the fixed length of the 2D channel. Particles are added at one end of the fixed channel at random positions and removed from the computation when they leave the channel keeping the overall density of the particles fixed. Density fluctuations in the channel follow Burgers equation [32][83]. A locally dense region expands in time due to HI and pairing. These pairs move at different speeds across the channel. This effect is therefore transformed in the opposite direction of the flow. As new particles are injected into the channel by an external pressure source, the interplay between the back pressure and external pressure gives rise to the Burgers shock waves.
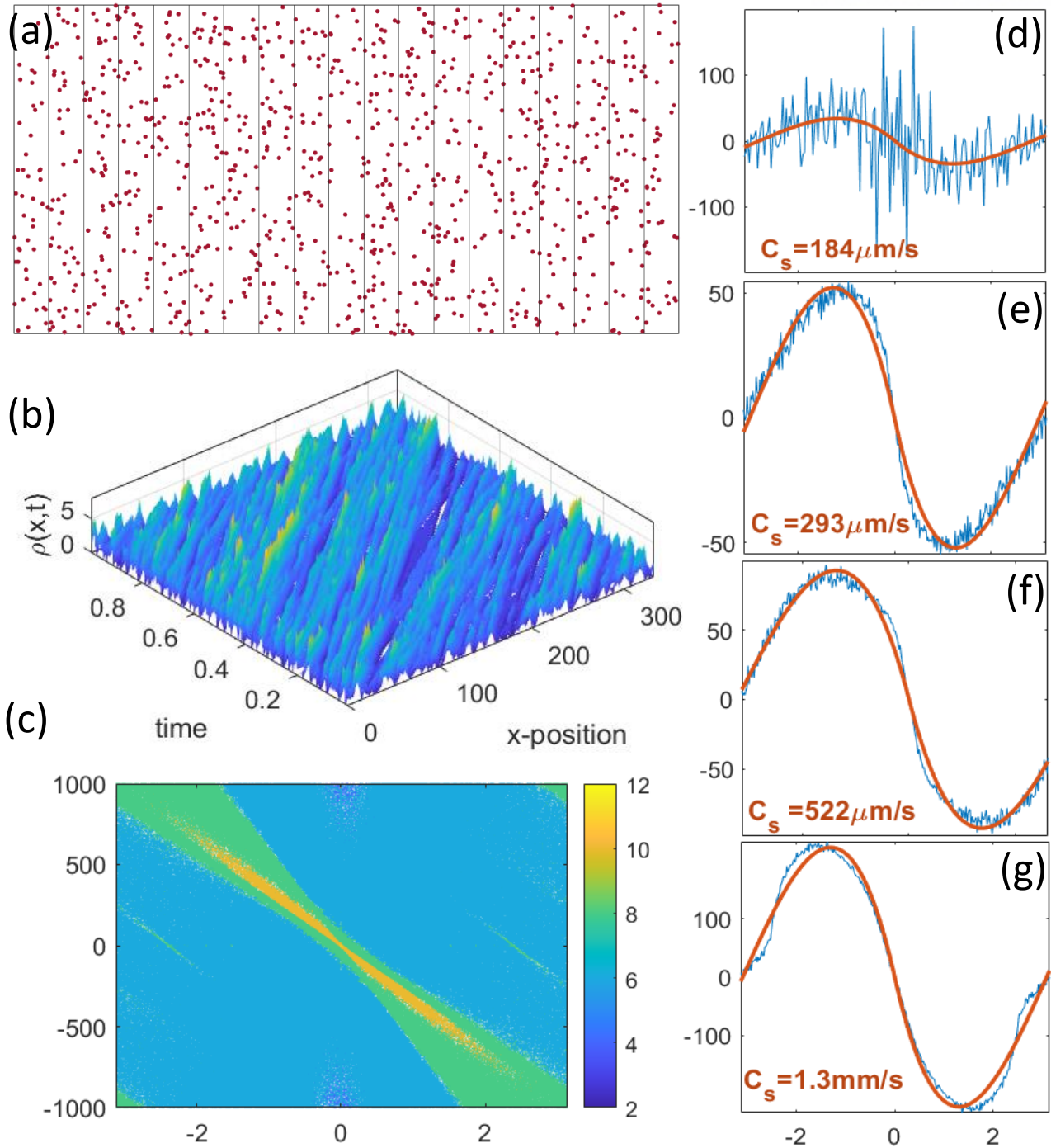
Figure 2.8. *Fourier analysis of unbounded 2D flow in experiment/simulation. (a) Snapshot for particle system with the random arrangement in 2D flow (simulation). The field of view is divided into small length segments. (b) Density of particles in each length segment as a function of space and time. (c) Fourier spectrum for $\rho(x,t)$ shows peaks on central line $\omega = Ck$. (d-g) Dispersion curve obtained from density variation in 2D flow experiments. The solid line is a fitted result using Eq. (3.17) with single fitting parameter C_s. (d) $u_{iso} \sim 1750\ \mu m/sec, \rho=0.8\ \%, f_s = 1KHz,$ and $R=3.5\mu m.$ (e) $u_{iso} \sim 1000\ \mu m/sec, \rho=0.7\%, f_s = 1KHz,$ and $R=3.5\mu m.$ (f) $u_{iso} \sim 1000\ \mu m/sec, \rho=0.14\ \%, f_s = 1KHz,$ and $R=3.5\mu m.$ (g) $u_{iso} \sim 700\ \mu m/sec, \rho=0.3\ \%, f_s = 1KHz,$ and $R=3.5\mu m.*

2.7   Pairs interactions in the experiment

Hydrodynamic interaction between two nearby particles is symmetric. Therefore, they move together at approximately the same speed until they meet a third particle, which breaks their symmetry. When two particles are close to each other they move as a pair at a slightly different speed compared to the background particles. The horizontal pairs move slower, and the vertical pairs move faster than the isolated particles. We investigated the motion of a very large number of pairs in the microfluidic channel. The mean horizontal and vertical speeds of pairs were weighted as a function of the angle with the flow. The Reynolds and Peclet numbers were $Re \cong 10^{-4} - 10^{-3}$, and $Pe \cong 10^{3} - 10^{4}$, allowing to safely disregard the inertial and thermal forces. Colloidal spheres of diameter 1-20 μm diameter were used in microfluidic channels with a gap size in the range of 10-50 μm. The flow rate in the channel was controlled via a syringe pump. The motion of particles was recorded digitally at 100 fps and tracked using MATLAB with a C11440 camera (Hamamatsu). For the moving frame measurement, the camera is fixed on the translation stage moving at the mean speed of particles. The aerial density of particles in the field of view was in the range of 1-7 percent. Instantaneous velocities of particles were measured by using video microscopy. Inter-particle separations for each frame were used to find the nearest neighboring pairs in all image frames. One end of the channel was kept open to make sure that particle flow remains steady and to avoid pressure buildup in the channel which can cause flow reversal. Due to the inverse-square decay of the hydrodynamic force, intra-pair forces are typically much stronger than interactions with the surrounding particles, and one would expect to see weakly interacting metastable pairs. Analysis of particle trajectories verified this prediction: a significant fraction of the particles, typically about 5-20 %, traverse in pairs, geometrically defined as couples of particles much closer to each other than to the next-nearest neighbor by a factor of ~3.5, such that their interactions with other particles are at least tenfold weaker (Fig. 2.9 d). Particle pairs are arranged in order of increasing pair length and inclination of pairs. The mean instantaneous velocity of pairs is multiplied by the pair length and plotted as a function of inclination with the flow after normalization (Fig. 2.9 a). The pairs move significantly faster than the entire population relative to the center of mass (Fig. 2.9 c). These weakly-interacting couples persist through typical lifetimes of $10-20 R/u$ (Fig 2.10) until they approach other particles. Results show that pair mean velocity follows the two-dimensional stream function and decays as by inverse square law (Fig. 2.9 b). To exclude the possibility that the system is significantly affected by non-hydrodynamic interactions, such as van der Waals or electrostatic forces, we compared the measurements to simulations of particle ensembles with purely hydrodynamic interaction, which exhibited similar velocity and lifetime distributions (Fig. 3.2).
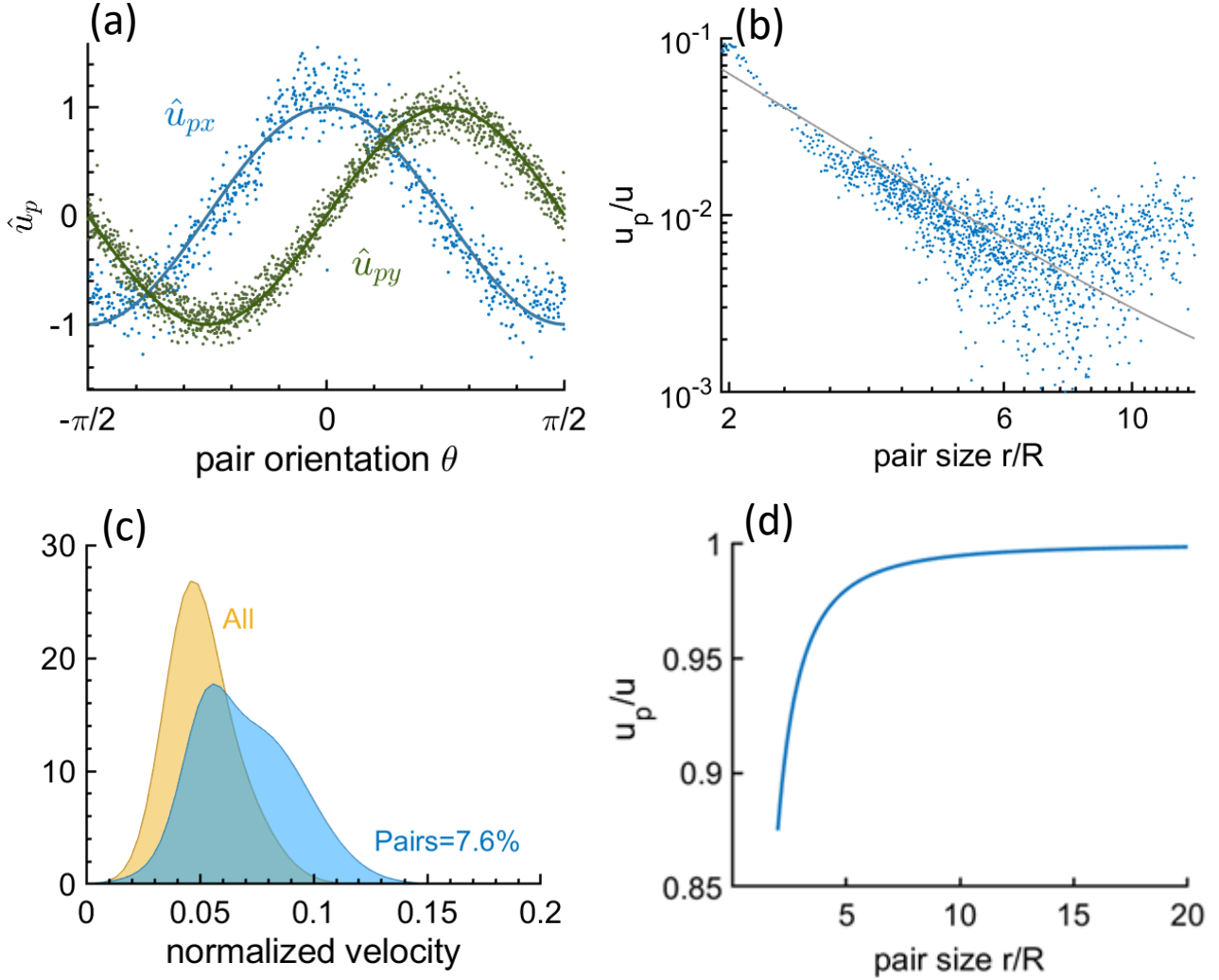
Figure. 2.9. *Experimental analysis of pair interactions (a-b) The measured pair velocity up, showing the direction $u^p \sim (\cos 2\theta \ ; \ \sin 2\theta)$ and the magnitude $|u_p| \sim r^{-2}$. Solid lines are the theoretical predictions. Here, $u_{iso} = 187 \mu m/s$, $K = 0.49$, $R = 3.5 \mu m$ and flow rate is 2nl/sec. (c) Distribution of velocity w.r.t. center of mass (in units of u) of all particles (gold) and in the pairs (blue, 7:6 % of all particles). (d) Pair velocity as function of pair size r/R. Pairs with minimum first neighbour distance $r_1 < 5R$ and second neighbour distance $r_2 \geq 3.5 \, r_1$ are sorted as pairs for evaluation*

2.8   Auto-correlation function and lifetime of pairs

To investigate the lifetime of pairs, the autocorrelation function for a substantial number of hydrodynamic pairs as a function of the first neighbor distance was computed from both the simulated and experimental results. We found that the pairs with smaller separations have the shortest correlation time. The autocorrelation function for two particles moving together can be written as

$$R_{xx}(\tau) = \frac{\sum_{t=k+1}^{T}(\Delta r_t - \Delta \bar{r})(\Delta r_{t-k} - \Delta \bar{r})}{\sum_{t=1}^{T}(\Delta r_t - \Delta \bar{r})^2} \tag{2.26}$$

We can also use Fourier transform to calculate the energy spectral density $S(\omega)$

$$S_{xx}(\omega) = \left|\int_0^{\infty} \Delta r(t)\exp(-i\omega t)\,dt\right|^2 = \frac{1}{N}\left|\sum_{j=1}^{N}\Delta r(j)\exp\left(-\frac{i2\pi jk}{N}\right)\Delta t\right|^2$$

$$R_{xx}(\tau) = \frac{1}{2\pi}\int_{-\infty}^{\infty}S_{xx}(\omega)\exp^{i\omega t}\,d\omega = \frac{1}{2\pi}\sum_{k=-\frac{N}{2}}^{\frac{N}{2}}S(k)\exp\left(\frac{i2\pi jk}{N}\right)\Delta \omega \tag{2.27}$$
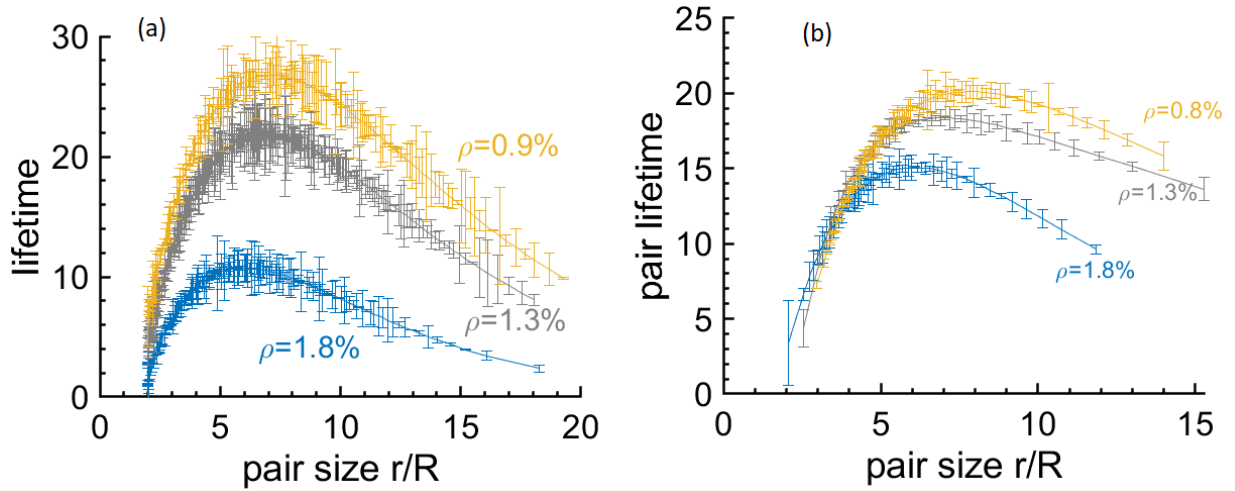
Figure 2.10. *Comparison of lifetime of pairs between (a) simulation and (b) experiment.*

Autocorrelation functions of the pairs are computed for a substantial number of pairs in simulation and experiments. The lifetime of the pairs is defined as the time for the correlation function to decrease by 25%. Particles forming pairs are close to each other and move with the maximum velocity gradients compared to the background particles, hence they reach out to the nearby particles at a faster rate. The correlation function is maximum for the pairs with intermediate pair-lengths and they persist for a lifetime of 10-20R/u (Fig. 2.10). pairs are selected on the basis that their next neighbor separation is 3.5 times larger compared to the nearest neighbor distance and are tracked for a significant period while they traverse the field of view. Video Frame per second and particle speed is adjusted such that $\Delta t_{frame} < R/u$, this also helps in identifying the particle by using the relative displacement from one frame to the next. We have used the Eulerian approach, though it limits the time for observation of an individual particle due to the limited size of the field of view. However, in this case, channel size does

not hinder the long-time observation of particles and videos can be produced for exceedingly long durations.

2.9   Unbounded finite collection of particles

HI causes the denser collection of particles to expand in time, but as interaction propagates out reflection from the outer layer pushes the inner particles back toward the center, thus a finite assembly will oscillate for a finite time depending on its size and an infinite assembly ensemble will oscillate indefinitely. It takes a finite amount of time for particles at edges to move out. Dispersion time for particles depends on their initial density and the overall size of the collection (Fig. 2.11). To visualize the size and density effect, the random distribution of particles is used and the density and aerial size of distribution are increased stepwise. Simulation is stopped when the density in the central region $(100 \times 100R^2)$ is reduced to 50% of its initial value. Intuitively the stopping time for simulation increases with aerial size and decreases with density. We can further deduce that whenever there is a

Figure 2.11. *Expansion of unbounded finite collection of particles in simulation with different density and lattice size. The simulation is stopped when the density in central $100 \times 100R^2$ reduces to half of its initial value.*

higher local density at some point in a large collection of particles, HI between particles forces it to expand, and surrounding particles pushes it back, which will cause oscillation and formation/breaking of pairs.
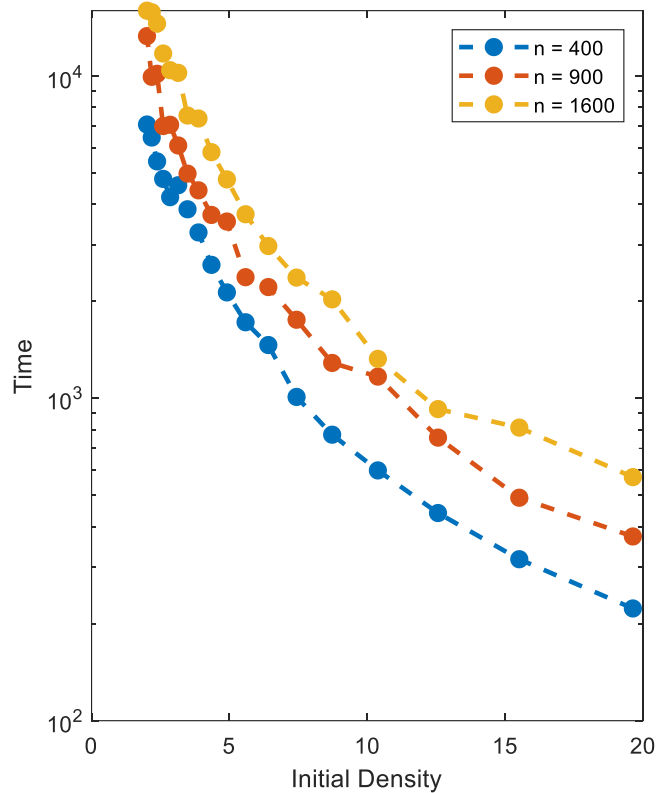
2.10 Group velocity and van Hove singularity

Dispersion relation in Eq. (2.19) can be used to derive the group velocity for hydrodynamic phonons

$$v_g = \frac{d\omega}{dk} = C_s \left[1 - 3\left(\frac{ka}{2\pi}\right) + 2\left(\frac{ka}{2\pi}\right)^2 \right] \tag{2.27}$$

The group velocity v_g becomes zero at $k = 1.32/a$ leading to singularity, analogous to van Hove Singularities (vHSs) in solid crystals. We simulated the motion of particles in a one-dimensional chain with periodic boundary conditions (Fig. 2.12 a). Fourier amplitudes for the relative separation of particles in a moving frame were found to be distributed with peaks at $k = 1.32/a$ leading to the conclusion that there is an analogy between a moving 1D hydrodynamic crystal and a stationary solid crystal. The above relation can be simplified by assuming $C_s = 1, a = 1$. At the singularity point, $d\omega/dk = 0 \rightarrow \omega = 0.6046 = \pi/3^{3/2}$. Hence the density of states $\rho(\omega')d\omega' = d\omega'/v_g$ can be written

$$\rho(\omega') = i\sqrt{3}\left(\frac{1}{1-\omega'\left(\omega'+i\sqrt{1-\omega'^2}\right)} + \frac{1}{\left(\omega'+i\sqrt{1-\omega'^2}\right)^{\frac{3}{2}}-1} \right), \qquad \omega' = \frac{\omega}{\pi/3^{3/2}} \tag{2.28}$$

The plot for analytical density shows peaks at singularity points (Fig. 2.12 c). We can use Eq. (2.15) for small perturbations in a linear chain (see Appendix III)

$$\begin{bmatrix} \delta\dot{x}_1 \\ \delta\dot{x}_2 \\ \delta\dot{x}_3 \\ \cdot \\ \cdot \end{bmatrix} = \frac{3}{\pi^2 \begin{bmatrix} \left(\Sigma\frac{1}{x_{1j}^3}\right) & \frac{1}{x_{12}^3} & \frac{1}{x_{13}^3} & \cdot & \cdot \\ \frac{1}{x_{12}^3} & \left(\Sigma\frac{1}{x_{2j}^3}\right) & \frac{1}{x_{23}^3} & \cdot & \cdot \\ \frac{1}{x_{13}^3} & \frac{1}{x_{23}^3} & \left(\Sigma\frac{1}{x_{3j}^3}\right) & \cdot & \cdot \\ \cdot & \cdot & \cdot & \cdot & \cdot \end{bmatrix}} \begin{bmatrix} \delta x_1 \\ \delta x_2 \\ \delta x_3 \\ \cdot \\ \cdot \end{bmatrix} \tag{2.29}$$

This equation is solved analytically for eigenfrequencies with a periodic arrangement of 1000 particles in a one-dimensional chain. External white noise is added to the system in proportion to the period of the lattice. The real space coordinate of particles is used in MATLAB solver to get the eigenfrequency for the above matrix. Plot for the real and imaginary parts (Fig. 2.12 b) peaks near singular points. Solutions are used to solve for each particle velocity in the chain. The real and imaginary solutions are plotted separately (Fig. 2.12 d-g). The particles near the center move toward each other and eventually pairs of particles oscillate back and forth in the chain.
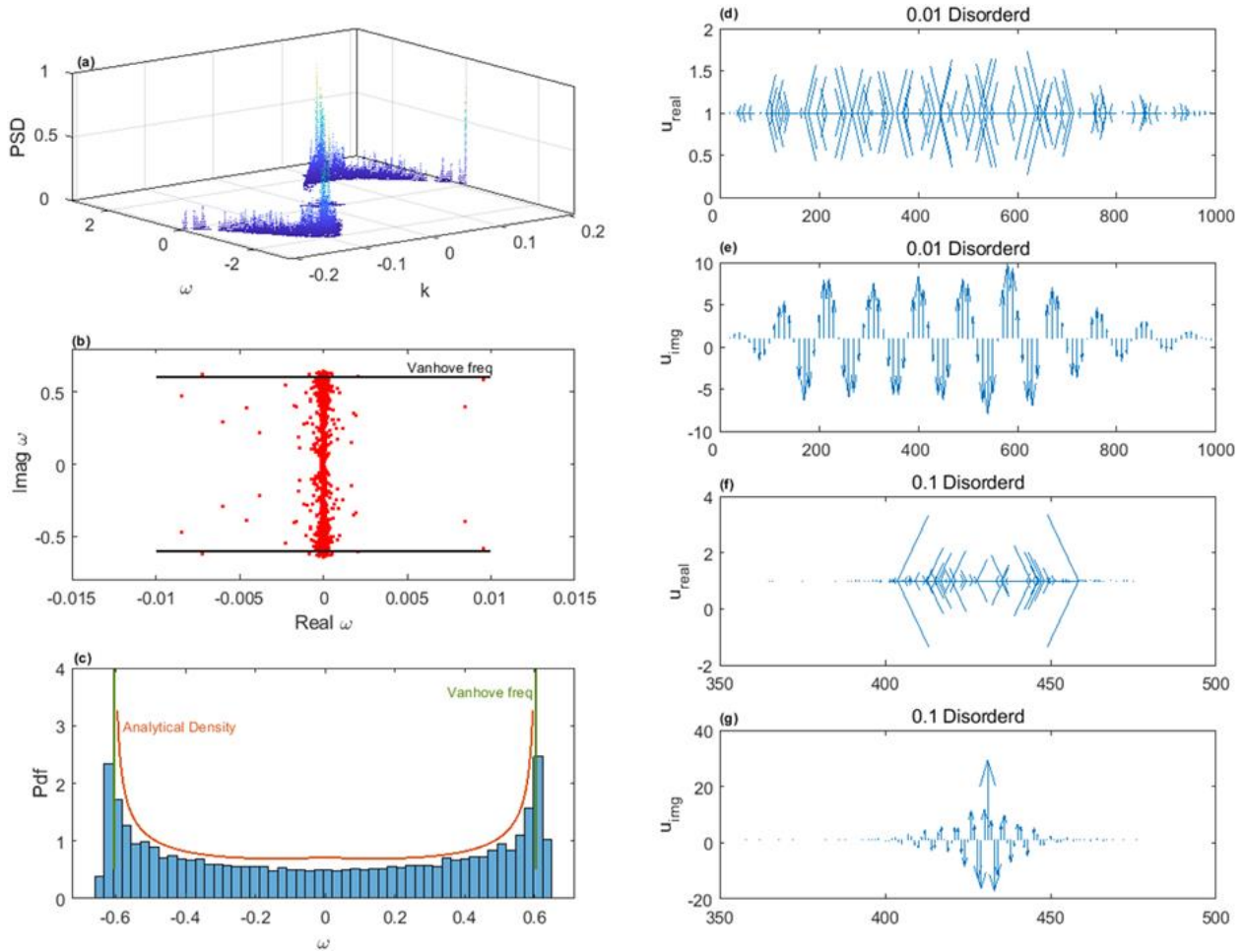
Figure 2.12. *(a) Van Hove singularities in 1D chain of particles visualised as peak in power spectral density (simulation result). (b) Real and imaginary part of eigenvalues of Eq. (2.29) for crystal arrangement with 1% noise. (c) Density distribution from the eigen matrix is compared with analytical density of Eq. (2.28). (d–g) Result for real and oscillating particle velocities obtained from the solution of eigen matrix with 10% and 1% noise,. Here, arrow size indicates the magnitude of particle velocity.*

2.11 Brillouin zone and reciprocal space in a two-dimensional lattice

To define Brillouin zones we use Bloch's theorem for two lattices which can be written as

$$\phi_k\,(r\,+\,R) = \;e^{2\pi ik\cdot R}\,\phi_k(r) \tag{2.30}$$

Here, $\phi_k(r)$ is a Bloch function for position R and wave vector k. R is a lattice vector between a pair of unit cells: $R\;=\;ua\,+\,vb$; u and v are integers and the dot product $k\cdot R\;=\;k_a u\,+\,k_b v$. Let us consider the two-dimensional oblique lattice where the basis vectors, a and b, are not orthogonal and there is no symmetry relationship between their lengths. An operation that translates by the lattice vector R (which we may call t^R) is given as follows.

$$t^R\,\phi_k(r) = \;exp^{(2\pi ik\cdot R)}\,\phi_k(r) = e^{2\pi i(k_a u + k_b v)}\phi_k(r) \tag{2.31}$$

The above expression makes sense if we define the *k-space* in the basis vector a^* and b^* such

$$a^*\perp b, \text{ and } b^*\perp a, \text{ and } a^*\cdot a = 1,\ \ b^*\cdot b = 1. \tag{2.32}$$

Therefore,

$$a^* = 2\pi\frac{b\times\hat{n}}{|a\times b|},\ \ b^* = \frac{\hat{n}\times a}{|a\times b|} \tag{2.33}$$

Here, $\hat{n}$ is a unit vector normal to the two-dimensional system. The vectors, a^* and b^*, can be used to build up an entire lattice of points K_{hk} defined such that $K_{hk}\;=\;ha\,+\,kb$, where h and k are integers. If we have two k vectors k_1 and k_2 which differ by K_{hk} , i.e., $k_1\;=\;k_2\;+\;K_{hk}$.

$$\exp^{2\pi ik_1\cdot R}\;\;=\;e^{2\pi i\big((k_2+K_{hk})\cdot R\big)}\,,$$

where $K_{hk}\cdot R = uh + kv$ is an integer, hence k_1 and k_2 are equivalent. Any basis function that transforms according to the irreducible representation labeled by k_2 belongs to the equivalent irreducible representation labeled by k_1 . It can be found that any representation outside of the range $-\frac{\pi}{a}<\;k<\frac{\pi}{a}$ is redundant. We can do this geometrically by enclosing the region in the reciprocal space that surrounds $k=0$ such that all enclosed k points are closer to $k=0$ in comparison to any other lattice point. This will be the region of space enclosed by the set of planes that are perpendicular bisectors to the lattice vectors connecting the origin in k -space to its nearest neighbor reciprocal lattice

points. This region is the first Brillouin zone. Primitive vector for a simple hexagonal lattice $\vec{a} = a\hat{x}$, $\vec{b} = \frac{a}{2}(\hat{x} + \sqrt{3}\hat{y})$, $\hat{n} = \hat{z}$ as shown in Fig. 2.15 a. The corresponding primitive vectors can simply be determined by using Eq. (3.34).

$$a^* = 2\pi \frac{\frac{a}{2}(\hat{x} + \sqrt{3}\hat{y}) \times \hat{z}}{\frac{\sqrt{3}}{2}a^2 c} = \frac{2\pi}{a}\left(\hat{x} - \frac{1}{\sqrt{3}}\hat{y}\right) \tag{2.34}$$

$$b^* = 2\pi \frac{\hat{z} \times a\hat{x}}{\frac{\sqrt{3}}{2}a^2 c} = \frac{4\pi}{\sqrt{3}a}\hat{y} \tag{2.35}$$

Comparing the magnitude of $|a^*| = |b^*| = \frac{4\pi}{\sqrt{3}a}$ reciprocal lattice vectors with magnitudes of the primitive vector $|a| = |b| = a$, shows that reciprocal lattice is also another simple hexagonal lattice with lattice constant $\frac{4\pi}{\sqrt{3}a}$, but rotated through $\frac{\pi}{6}$ about the c-axis with respect to the direct lattice as shown in Fig. 2.15 b.

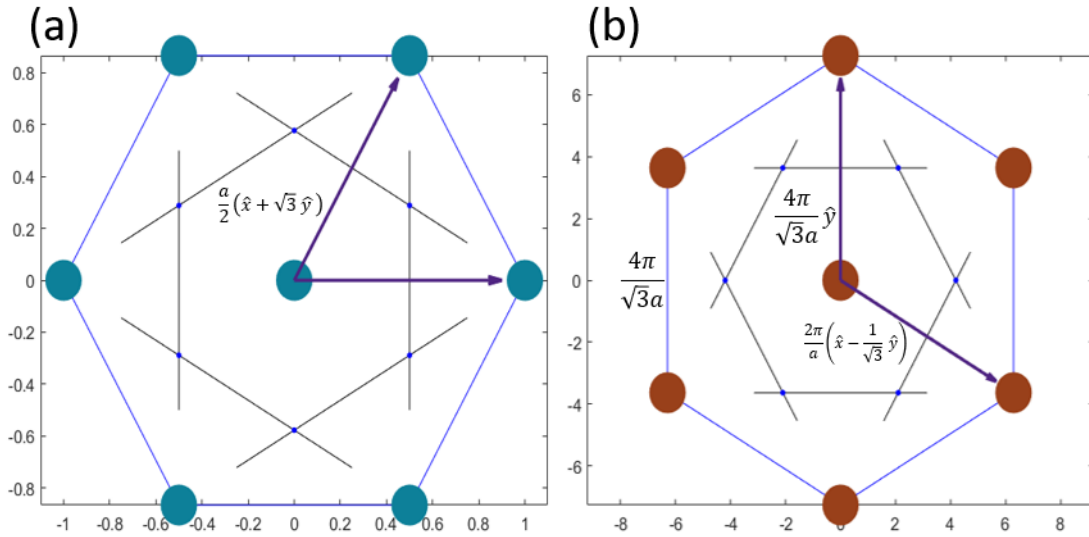**Figure 2.13.** *(a) Direct lattice for hexagonal crystal with lattice constant a in real space. (b) Reciprocal lattice is also hexagonal with lattice constant $4\pi/(\sqrt{3}a)$ in 2D k-space. The region enclosed by bisector lines is first Brillouin zone. Vertices of the first Brillouin zone are Dirac points (small blue dots). Reciprocal lattice is rotated through $\pi/6$ in comparison to direct lattice.*

3 QUASIPARTICLES, FLAT BANDS, and MELTING of HYDRODYNAMIC MATTER

The idea of quasiparticles was introduced by Landau in 1941 [63] and ever since has provided insight into emergent collective phenomena in a wide variety of physical systems. The term quasiparticle is specifically used when an entity is observed to have properties that its parts do not possess on their own. It is also implied for the phenomenon which arises when a microscopic collection behaves as if it contained different weakly interacting particles. A few examples of quasiparticles are as follow

1. As the motion of an electron is disturbed in a complex way when it travels through a semiconductor compared to a vacuum, it behaves as though it has a different effective mass. Such an electron is called an electron quasiparticle [64].

2. The aggregate motion of electrons in the valence band of the semiconductor [65] behaves as though the material instead contained positively charged quasiparticles called electron holes.

3. A phonon is a quantum particle related to the vibration of atoms in a crystal structure.

4. A roton is a collective excitation associated with the rotation of a superfluid (a fluid with zero viscosity that flows without any loss of kinetic energy). When stirred, it forms vortices that continue to rotate indefinitely. Superfluidity occurs in two isotopes of helium (helium-3 and helium-4) when they are liquified by cooling to cryogenic temperatures.

5. A plasmon is a quantum particle derived from plasma oscillation.

6. Several other kinds of quasi-particles have been discovered by experiments or theoretical predictions, such as the Dirac fermions, Weyl fermions, and Rarita-Schwinger-Weyl fermions. Furthermore, a few quasiparticles beyond particle physics have also been demonstrated in materials, for example, type-II Dirac/Weyl fermions, nodal line, quadratic or cubic Weyl fermions, hourglass fermions, and high-fold fermions.

The quasiparticles in solid-state materials have provided a tabletop platform to imitate the particles in high-energy physics. The topological phase transitions also give a route to study the interaction between elementary particles. These phenomena are typically called quasiparticles if they are related to fermions and called collective excitations if they are related to bosons, although the precise distinction is not universally agreed upon. Thus, electrons and electron holes (fermions) are typically called quasiparticles, while phonons and plasmons (bosons) are typically called collective excitations.

In the present work, we discuss the collective phenomenon in the classical dissipative system of hydrodynamically interacting particles and describe some similarities to the well-known phenomenon in quantum matter, especially to the notion of quasiparticles and flat bands.

We consider a viscous fluid driving micron size particles inside a microfluidic-channel. The spacing between the channel floor and ceiling is such that particles cannot overlap thus making an effective two-dimensional system. However, particles do feel friction due to channel surfaces and move slightly slower than driving fluid. Reynolds number for the flow is very small $\sim 10^{-4}$ such that we can neglect inertial terms, and the Peclet number for the flow is large enough $\sim 10^{4}$ such that we forget about the thermal effect. We assume uniform laminar flow in the channel. Since particles perturb the uniform streamlines around the other particles, thus effectively interact with each other by perturbing the drag force. The streamlines that each particle emits have the shape of the hydrodynamic dipole.

$$f(r) \sim \frac{1}{r^2} \begin{pmatrix} \cos(2\theta) \\ \sin(2\theta) \end{pmatrix}$$

If angle θ is replaced by $\pi - \theta$, we get the same force, which implies that each particle pushes the other particles in the same direction with a force that has the same magnitude. If two particles are sufficiently far from other

Figure 3.1. The experimental system with $l = 7$ μm particles whose areal density is $\rho = 1.8$ % in a channel of height 10 μm (Top). Arrows denote particle velocity w.r.t. the mean velocity u $= 200$ μm/s. Notable are pairs of particles moving at similar velocities. as depicted in the schematic (Bottom)

particles and the system is sufficiently dilute with aerial densities $< 10\%$, they will move together with the same velocity in the same direction as a pair until or unless they come across other nearby particles. The hydrodynamic force f(r) exerted on a particle by another particle at a distance $r = (r, \theta)$, where θ is the angle with respect to the flow direction, has a magnitude decaying as the distance squared, r^{-2} , and has a direction 2θ. This twofold symmetry implies that the dipolar force is invariant under parity, f($-r$) = f(r). Thus, the hydrodynamic forces that a pair of particles exert on each other are equal, and the isolated pairs should therefore be stable due to the dissipative nature of the forces. Momentum conserving forces, in contrast, is anti-symmetric, f($-r$) = $-$f(r), and thereby destabilizing the pairs. This reveals that interaction does not obey Newton's third law and momentum is leaking out of the system at channel walls. To make the particles flow, the momentum loss needs to be compensated by constantly pumping momentum through the pressure gradient along the channel. Due to the inverse-square decay of the hydrodynamic force, intra-pair forces are typically much stronger than interactions with the surrounding particles, and one would expect to see weakly-interacting metastable pairs. When
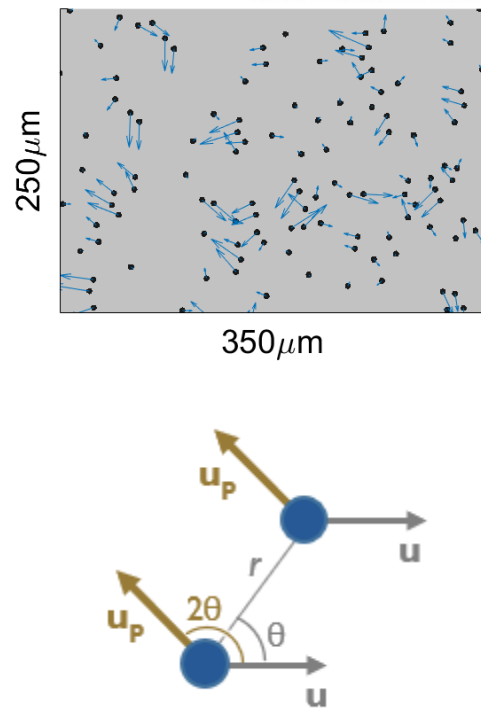
particles are separated far away from each other, therefore, ignoring the hydrodynamic interaction among them, we can say the system is in a ground state. When two particles approach each other forming a hydrodynamic pair, the pair is in a weakly excited "quasi-particle" state.

Experimental measurement reveals that pairs are indeed stable. Figure 3.1 is an experimental picture showing that a significant fraction of the particles are moving in the same direction. A pair oriented at an angle θ moves at a velocity $\boldsymbol{u}_p \sim u(R/r)^2 (\cos 2\theta; \sin 2\theta)$, as verified in the experiment Fig. 2.9 a. Velocities are measured with respect to the center of mass. Isolated particles move more or less with a center of the mass and pairs are much faster (Fig. 2.9 c) with interaction decaying as inverse square (Fig. 2.9 b). Another important result derived from these experiments is that pairs live long $\sim 10 - 20 R/u$ (Fig. 2.10).

To exclude the possibility that the system is significantly affected by non-hydrodynamic interactions, such as van der Waals or electrostatic forces, we compared the measurements to the simulations of particle ensembles with purely hydrodynamic interaction (Fig. 3.2). Here we used the same density of particle as in the experiment and simulated the flow with the periodic condition. Both experiment and simulation give compelling evidence that supports pairing as the main mechanism which dominates the interaction.

Modeling and simulation of the ordered crystalline phase identify the pairs as quasiparticles, emerging at the Dirac cones of the spectrum, as explained in later sections. In square crystals, the quasiparticles stimulate supersonic pairing avalanches, bringing about the melting of the crystal. In hexagonal crystals, the intrinsic threefold symmetry of the hydrodynamic interaction matches that of the crystal, therefore, the spectrum forms a flat band dense with ultra-slow, low-frequency phonons whose collective interactions induce a much sharper melting transition.
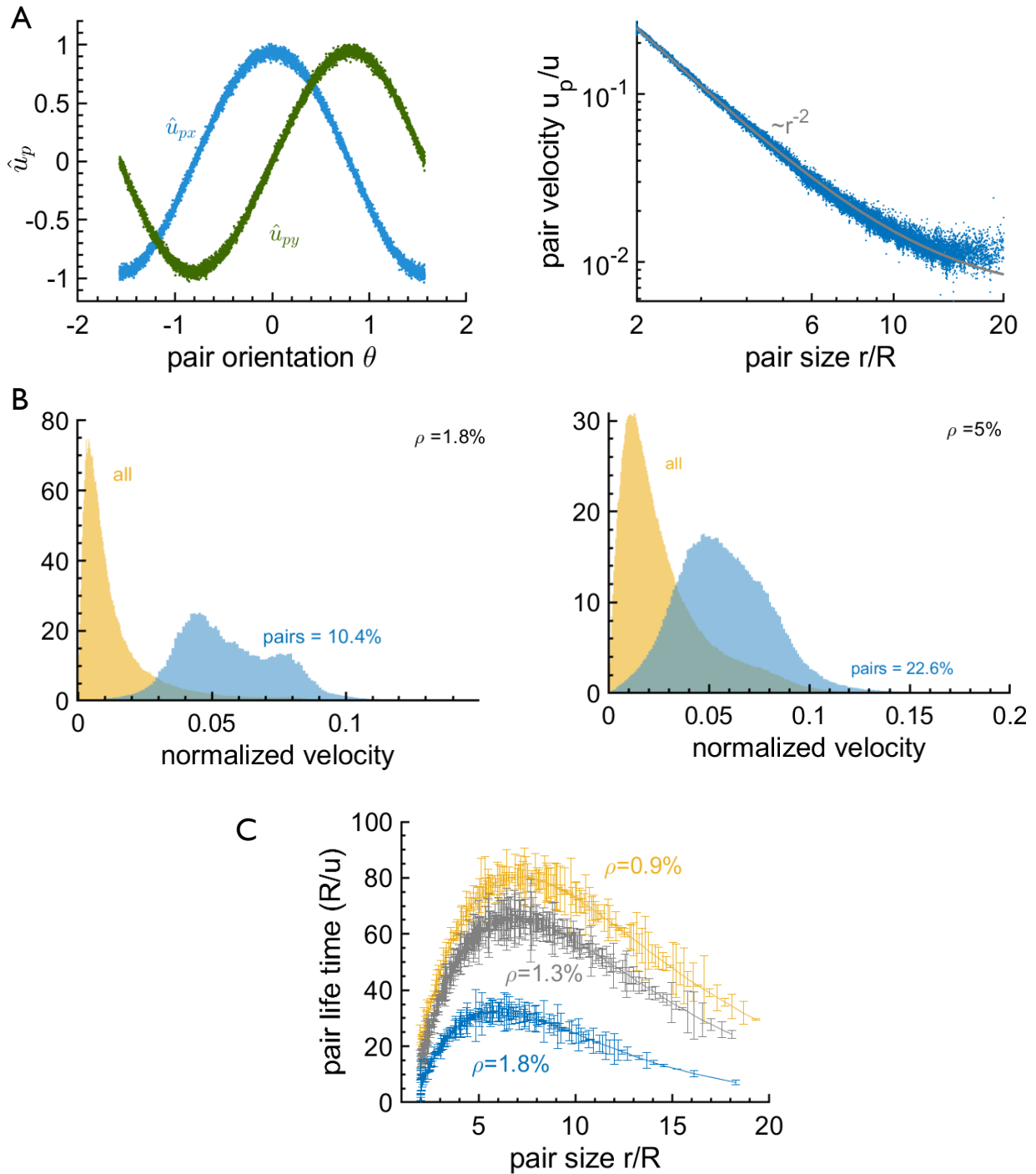
Figure 3.2. *Analysis of pair interactions (simulation) for comparison with experiment. A. The pair velocity u_p in simulations, showing the direction $\hat{u}_p \sim (\cos 2\theta \,;\, \sin 2\theta)$ (Left) and the magnitude $|u_p| \sim r^{-2}$ (Right), with a geometric factor $\alpha = 0{:}34$ estimated from the experiment. Solid lines are the theoretical predictions (as in the experiment, Fig. 2.9b). B. Distribution of velocity w.r.t. centre of mass (in units of u) of all particles (gold) and in the pairs (blue) in simulations, for areal densities $\rho = 1{:}8\%$ (left), and 5:0 % (right) (as in the experiment, Fig. 2.9c). C. Lifetime of pairs (in R=u units) as a function of pair size r=R for areal densities $\rho = 0.9, 1.3$ and 1.8 % in simulations (as in the experiment, Fig. 2.9 d).*

3.1 Schrodinger-like hydrodynamic equation of motion

The hydrodynamically-interacting particle ensemble exhibit complicated chaotic dynamics in the fully-disordered phase and non-linear mode-coupling in the ordered, crystalline phase. To compute their trajectories, one could in principle solve the underlying Stokes equations consistently with the moving boundaries of the particles, albeit this is in general a rather cumbersome procedure. One possible approach is expanding the hydrodynamic interactions as a multipole series over "hydrodynamic image charges" induced by the particles' solid boundaries. The procedure is remarkably similar to electrostatics since the same Laplace equation solves the Hele-Shaw flow potential. For example, if we consider two finite particles of size, then the first image in the interaction will be a dipole $\sim \left(\frac{l}{r}\right)^2$, followed by an infinite series of multiple reflections, $\left(\frac{l}{r}\right)^4$, $\left(\frac{l}{r}\right)^6$,... Thus, in an ensemble of particles, one in principle needs to sum over all possible multiple scattering paths among all the particles. Fortunately, since the system is always dilute ($\leq 7\%$ areal density), we can neglect all the higher terms and take only the first reflections. Thus, we can use the following two well-established approximations: (i) unless the particles at most touch each other, their induced velocity perturbations are approximated by the isolated dipole field Eqs. (3.6-7); (ii) the total hydrodynamic force acting on a particle can be simply computed as the sum of the pairwise interactions with all other particles. In the low-Reynolds regime, inertia is negligible, so the drag force is balanced by the driving force and the hydrodynamic interactions. The resulting system of N-coupled equations of motion is

$$\gamma \dot{\boldsymbol{r}}_i = \boldsymbol{F} + \sum_{j \neq i} \boldsymbol{f}(\boldsymbol{r}_{ij}) \quad \text{where } i, j = 1, 2, \dots, N. \tag{3.1}$$

Here, $\boldsymbol{F}$ is an external force on each particle and $\boldsymbol{f}(\boldsymbol{r}_{ij})$ is the hydrodynamic force exerted by the jth particle on the ith particle given as

$$f(r_{ij}) = \alpha . \gamma u \left(\frac{l}{r_{ij}}\right)^2 \begin{bmatrix} \cos(2\theta_{ij}) \\ \sin(2\theta_{ij}) \end{bmatrix}, \tag{3.2}$$

where $r_{ij} = r_i - r_j$ are the distance vectors. In polar coordinates, $r_{ij} = (r_{ij}, \theta_{ij})$. The geometric factor $\alpha \sim O(1)$ depends on the shape of the particles (e.g., disks, spheres, in the experiment for spherical particles $\alpha = 0.3{-}0.5$). Equation (3.2) implies that $f_{ji} = f_{ij}$, since the angles obey $\theta_{ji} = \pi + \theta_{ij}$. This implies that an isolated pair moves at a uniform velocity $u_p = \frac{f(r_{ij})}{\gamma} = \alpha u \cdot \left(\frac{R}{r}\right)^2 (\cos 2\theta, \sin 2\theta)$. Therefore, the hydrodynamic interaction between the two nearby particles decays following the inverse square law and is symmetric such that both particles feel the same force

with the same sign. This seems to contradict Newton's third law. While the microscopic molecular forces in the fluid obey Newton's law, when two particles in our system are moving together, the net force they exert on each other is essentially zero and their separation remains fixed until or unless they are acted upon by a third particle. Velocities of both particles will be different from the isolated particle depending on their separation r_{ij} and inclination θ_{ij}. At steady-state, the hydrodynamic interactions in Eq. (3.1) vanish by symmetry, $\sum_{j \neq i} f^{ij} = 0$, and the lattice moves uniformly at a velocity $u = \frac{F}{\gamma}$, relative to the surrounding fluid.

$$\delta \dot{r}_i = \sum_{j \neq i} f(r_{ij}) \equiv \mathcal{F}_i(\{r_j\})$$

Expansion of the equations of motion in small deviations of the lattice positions around the steady-state positions, $\delta r_i \equiv r_i - \bar{r}_i$, yields a linear dynamic equation

$$\delta \dot{r} = H \, \delta r \tag{3.3}$$

where δr is the $2N$-vector of the N particle deviations around the steady state positions. The tensor H^{ij} explains the 2D hydrodynamic interaction between the i_{th} and j_{th} particles and $H^{ij} = \left. \frac{\partial \mathcal{F}_i}{\partial r_j} \right|_{r_j = \bar{r}_j}$ is a generalized spring constant that multiplies the deviation δr to give the hydrodynamic force.

$$H^{ij} = 2 \left(\frac{l}{r_{ij}} \right)^3 \begin{bmatrix} \cos 3\theta_{ij} & \sin 3\theta_{ij} \\ \sin 3\theta_{ij} & -\cos 3\theta_{ij} \end{bmatrix} \tag{3.4}$$

$$\delta \dot{r}_{i\alpha} = \sum_{\substack{j \neq i \\ \beta}} H^{ij}_{\alpha\beta} \delta r_{j\beta}, \qquad \text{where } H^{ij}_{\alpha\beta} = \left. \frac{\partial \mathcal{F}_{i\alpha}}{\partial r_{j\beta}} \right|_{r_j = \bar{r}_j} \tag{3.5}$$

Here, α and β are x and y components of each H^{ij}. Therefore, H is a $2N \times 2N$ matrix composed of 2×2 blocks H^{ij}. Since H^{ij} is a function of $3\theta_{ij}$, H has a three-fold symmetry. This unusual symmetry of H stems from its definition as the derivative of the force, $H = \frac{\delta f}{\delta r}$ in which the dipolar force f has a two-fold symmetry $f \sim \frac{e^{i2\theta}}{r^2}$. Note that H is translation invariant (H_{ij} is a function of only $(r_j - r_i)$) and anti-symmetric, $H_{ji} = -H_{ij}$. Due to the translationally invariant property, $\sum_j H^{ij} \delta r_j = \sum_j H^{ij} [\delta r_j + C]$ for arbitrary lattice vector C. Therefore, $\sum_j H^{ij} = 0$ and $H_{ii} = -\sum_{j \neq i} H^{ij}$. The anti-

symmetric property causes the vanishing diagonal elements of $H^{ij} = 0$. Therefore, H of a crystal is skew-Hermitian with N purely imaginary eigenvalues, representing N phononic modes.

The deviation $\delta \boldsymbol{r}_j$ of each particle from its mechanical equilibrium $\bar{\boldsymbol{r}}_j$ can be expressed by the normal mode of plane waves $\delta \boldsymbol{r}_j(t) = \Psi_k(t)\exp[i\boldsymbol{k} \cdot \bar{\boldsymbol{r}}_j] = \psi_k \exp[i(\boldsymbol{k} \cdot \bar{\boldsymbol{r}}_j - \omega t)]$. Here, $\Psi_k(t) = \psi_k e^{-i\omega_k t}$ is a 2D polarization vector in k -space. Equation (4.2) is similar to the time-dependent Schrodinger equation

$$i\hbar \frac{\partial}{\partial t}|\boldsymbol{\psi}_k(t)\rangle = \mathcal{H}_k|\boldsymbol{\psi}_k(t)\rangle \tag{3.6}$$

Therefore, Eq. (3.3) is a Schrodinger-like equation

$$-i\omega_k \boldsymbol{\psi}_k \exp[i(\boldsymbol{k} \cdot \bar{r}_i - \omega_k t)] = \sum_j H^{ij}(\bar{r}_j - \bar{r}_i)\,\boldsymbol{\psi}_k \exp[i(\boldsymbol{k} \cdot \bar{r}_j - \omega_k t)]$$

$$\omega_k \boldsymbol{\psi}_k = i \sum_j H^{ij}(\bar{r}_j - \bar{r}_i)\exp[i\boldsymbol{k} \cdot (\bar{r}_j - \bar{r}_i)]\boldsymbol{\psi}_k$$

$$H_k \psi_k \ = \ \omega_k \psi_k \tag{3.7}$$

The last equation is a time-independent Schrodinger equation with an eigenvector ψ_k and eigenfrequency ω_k. Here, H_k is the hydrodynamic Hamiltonian in k -space and a 2×2-matrix, which is a Fourier transform of $H_{ij} \ = \ H(r_j - r_i)$,

$$H_k \ = \ i \sum_j H(r_j - r_i)e^{\,ik \cdot (r_j - r_i)} \tag{3.8}$$

In this equation, an imaginary unit i is multiplied for convenience, such that H_k becomes Hermitian. Therefore, H_k is a Hermitian operator and eigenfrequency ω_k is a real number. There are N operators H_k (one for each k) with N real phonon eigenfrequencies ω_k. Since any 2×2 Hermitian matrix can be written uniquely as a linear combination of Pauli matrices, with all coefficients being real numbers, H_k can be written in terms of Pauli matrices

$$\mathcal{H}_{\boldsymbol{k}} = i \sum_j H^{ij}(\bar{r}_j - \bar{r}_i)\exp[i\boldsymbol{k} \cdot (\bar{r}_i - \bar{r}_j)] = \Omega_x \sigma_z + \Omega_y \sigma_x$$

$$\mathcal{H}_{\boldsymbol{k}} = i \sum_j 2\left(\frac{\ell}{\bar{r}_{ij}}\right)^3 \begin{bmatrix} \cos 3\theta_{ij} & \sin 3\theta_{ij} \\ \sin 3\theta_{ij} & -\cos 3\theta_{ij} \end{bmatrix} \exp[i\boldsymbol{k} \cdot (\bar{r}_i - \bar{r}_j)]$$

$$= i \sum_j 2 \left(\frac{\ell}{\bar{r}_{ij}} \right)^3 \left(\sin 3\theta_{ij} \begin{bmatrix} 0 & 1 \\ 1 & 0 \end{bmatrix} + \cos 3\theta_{ij} \begin{bmatrix} 1 & 0 \\ 0 & -1 \end{bmatrix} \right) \exp\left[i\boldsymbol{k} \cdot (\bar{\boldsymbol{r}}_i - \bar{\boldsymbol{r}}_j) \right]$$

$$H_k = \sum_{j \neq 0} 2 \left(\frac{\ell}{\bar{r}_j} \right)^3 \left(\sin 3\theta_j\, \boldsymbol{\sigma}_x + \cos 3\theta_j\, \boldsymbol{\sigma}_z \right) \sin\left(\boldsymbol{k} \cdot \bar{\boldsymbol{r}}_j \right) \tag{3.9}$$

Here, $\sigma_x = \begin{pmatrix} 0 & 1 \\ 1 & 0 \end{pmatrix}$ and $\sigma_z = \begin{pmatrix} 1 & 0 \\ 0 & -1 \end{pmatrix}$ are Pauli matrices.

H_k can be written in terms of Pauli matrices

$$H_k = \Omega_k \cdot \sigma = \Omega_x \sigma_z + \Omega_y \sigma_x \tag{3.10}$$

The contributions of the long-range hydrodynamic interaction to H_k are Fourier sums,

$$\Omega_k = \begin{bmatrix} \Omega_x \\ \Omega_y \end{bmatrix} \sim \sum_{j \neq 0} \frac{2}{\bar{r}_j^3} \begin{bmatrix} \cos 3\theta_j \\ \sin 3\theta_j \end{bmatrix} \sin\left(k \cdot \bar{r}_j \right) \tag{3.11}$$

Due to the crystal's parity symmetry, Ω_x and Ω_y are always real. Since Ω_x and Ω_y are odd functions of k, H_k is also odd under parity, $H_{-k} = -H_k$. where $\bar{r}_j = r_j (\cos \theta_j;\ \sin \theta_j)$ are the distances of the steady-state lattice positions from an arbitrary origin particle. Due to the crystal's parity symmetry, Ω_x and Ω_y are always real. Since x and Ω_x are odd functions of k, H_k is also odd under parity, $H_{-k} = -H_k$. One can also represent the Hamiltonian with left and right circularly polarized unit vectors.

Hereafter, we measure the physical quantities by the relevant scales of the crystal: Distances are measured in the unit of a, the typical distance between the particles (and wavevectors in $1/a$). In a lattice, a is the lattice constant. Times are measured in the unit of the timescale $\tau = \frac{a}{u}$ for a perturbation to traverse a distance a. From Eq. (3.2), $u \sim u_o \frac{\ell^2}{a^2}$, where ℓ is the size of the particle and u_o is the speed of an isolated particle relative to the background flow speed. Therefore, the hydrodynamic time scale is

$$\tau_{hydro} \cong \frac{a}{u} = \frac{a}{u_o \dfrac{\ell^2}{a^2}} = \frac{a^3}{u_o \ell^2} \tag{3.12}$$

and the frequencies are measured in $1/\tau$.

3.2 Dispersion relation

By solving the eigenvalue equation $H_k \psi_k = \omega_k \psi_k$, we can find the dispersion relation.

$$\Omega_x \sigma_z + \Omega_y \sigma_x - \omega_k \begin{pmatrix} 1 & 0 \\ 0 & 1 \end{pmatrix} = 0 \qquad (3.13)$$

$$\begin{vmatrix} \Omega_x - \omega_k & \Omega_y \\ \Omega_y & -\Omega_x - \omega_k \end{vmatrix} = 0$$

$$\Omega_x^2 + \Omega_y^2 = \omega_k^2$$

The corresponding eigenfrequencies and eigenvectors are

$$\omega_k = \pm|\boldsymbol{\Omega_k}| = \pm\left(\Omega_x^2 + \Omega_y^2\right)^{\frac{1}{2}}$$

$$\psi_k^+ = \frac{1}{\sqrt{2}} \begin{bmatrix} \cos\frac{\alpha}{2} \\ \sin\frac{\alpha}{2} \end{bmatrix}, \quad \psi_k^- = \frac{1}{\sqrt{2}} \begin{bmatrix} -\sin\frac{\alpha}{2} \\ \cos\frac{\alpha}{2} \end{bmatrix} \qquad (3.14)$$

where the angle $\alpha = \arg(\Omega x + i\Omega y) = \tan^{-1}\left(\frac{\Omega y}{\Omega x}\right)$. On a circular basis, the eigenvectors are

$$\psi_k^\pm = \frac{1}{\sqrt{2}} \begin{bmatrix} \pm e^{\pm i\frac{\alpha}{2}} \\ e^{\mp i\frac{\alpha}{2}} \end{bmatrix} \qquad (3.15)$$

3.3 Nearest neighbor interaction in square crystal.

We consider a square arrangement and assume that each particle interacts with its nearest neighbor only as shown in Fig. 3.3. By using Eq. (3.11), we can write

$$\boldsymbol{\Omega_k} = \begin{bmatrix} \Omega_x \\ \Omega_y \end{bmatrix} \sim 2 \begin{bmatrix} \cos 0 \\ \sin 0 \end{bmatrix} \sin(a\boldsymbol{k} \cdot \hat{x}) - 2 \begin{bmatrix} \cos 3\pi \\ \sin 3\pi \end{bmatrix} \sin(a\boldsymbol{k} \cdot \hat{x})$$

$$+ 2 \begin{bmatrix} \cos\frac{3\pi}{2} \\ \sin\frac{3\pi}{2} \end{bmatrix} \sin(a\boldsymbol{k} \cdot \hat{y}) - 2 \begin{bmatrix} \cos -\frac{3\pi}{2} \\ \sin -\frac{3\pi}{2} \end{bmatrix} \sin(a\boldsymbol{k} \cdot \hat{y})$$

$$= 2 \begin{bmatrix} \sin(ak_x) + \sin(ak_x) & + & 0 & + & 0 \\ 0 & + & 0 & - & \sin(ak_y) - & \sin(ak_y) \end{bmatrix} = 4 \begin{bmatrix} \sin(ak_x) \\ -\sin(ak_y) \end{bmatrix}$$

$$\omega_k = \pm|\boldsymbol{\Omega_k}| = \pm\left(\Omega_x^2 + \Omega_y^2\right)^{\frac{1}{2}}$$

37

$$= \pm 4\sqrt{\sin^2(ak_x) + \sin^2(ak_y)} = \pm 2^{\frac{3}{2}}\sqrt{2 - \cos(2ak_x) - \cos(2ak_y)} \tag{3.16}$$

If the wave vector is measured in the units of $\frac{1}{a}$, the dispersion relation for the NN interaction in the square lattice is

$$\omega_{\boldsymbol{k}} = \pm 2^{\frac{3}{2}}\sqrt{2 - \cos(2k_x) - \cos(2k_y)} \tag{3.17}$$

Two distinctive features of the spectrum are: (i) four Dirac points (X points, $k = k_D$), where the positive and negative bands meet, forming a double cone, and (ii) four corresponding vHSs that occur at saddle points within the BZ ($k = \frac{1}{2}k_D$) where the density of states diverges logarithmically, $g(\omega) \sim \log|\omega - \omega_o|$, both features are hallmarks of quasiparticle spectra (Fig. 3.4 a-b). Dirac points occur at the wavevector k_D for which the hydrodynamic interaction vanishes $H = 0 \rightarrow \omega = 0$, corresponding to $\Omega_x = \Omega_y = 0$. Equation (3.11) implies thus when $\sin(k \cdot r_j) = 0$, corresponding to

Figure 3.3. *NN interactions for square lattice.*

$k_D \cdot r_j = \pm\pi$. Double Dirac cones meet at the Dirac points corresponding to $\omega = 0$, where the forces on the particles in each pair are equal and the hydrodynamic interaction force on the pair vanishes. Therefore, the corresponding pairing modes are marginally stable at finite amplitudes.

For square crystals, if we consider only the nearest-neighbor interactions, $\bar{r}_j = \pm a\hat{\boldsymbol{x}}$ or $= \pm a\hat{\boldsymbol{y}}$. The corresponding Dirac points are $\boldsymbol{k_D} = (\pm\pi, 0)$ when $\bar{r}_j = \pm a\hat{x}$ and $(0, \pm\pi)$ when $\bar{r}_j = \pm a\hat{y}$. $\boldsymbol{k_D}$ are halves of the reciprocal space base vectors, $\frac{1}{2}b_1$, $\frac{1}{2}b_2$, and their combinations,

$$k_D = \frac{1}{2}\beta_1 b_1 + \frac{1}{2}\beta_2 b_2 \quad \beta_1, \beta_2 \in \{-1, 0, 1\}. \tag{3.18}$$

These points are midpoints of the 1st BZ edges.
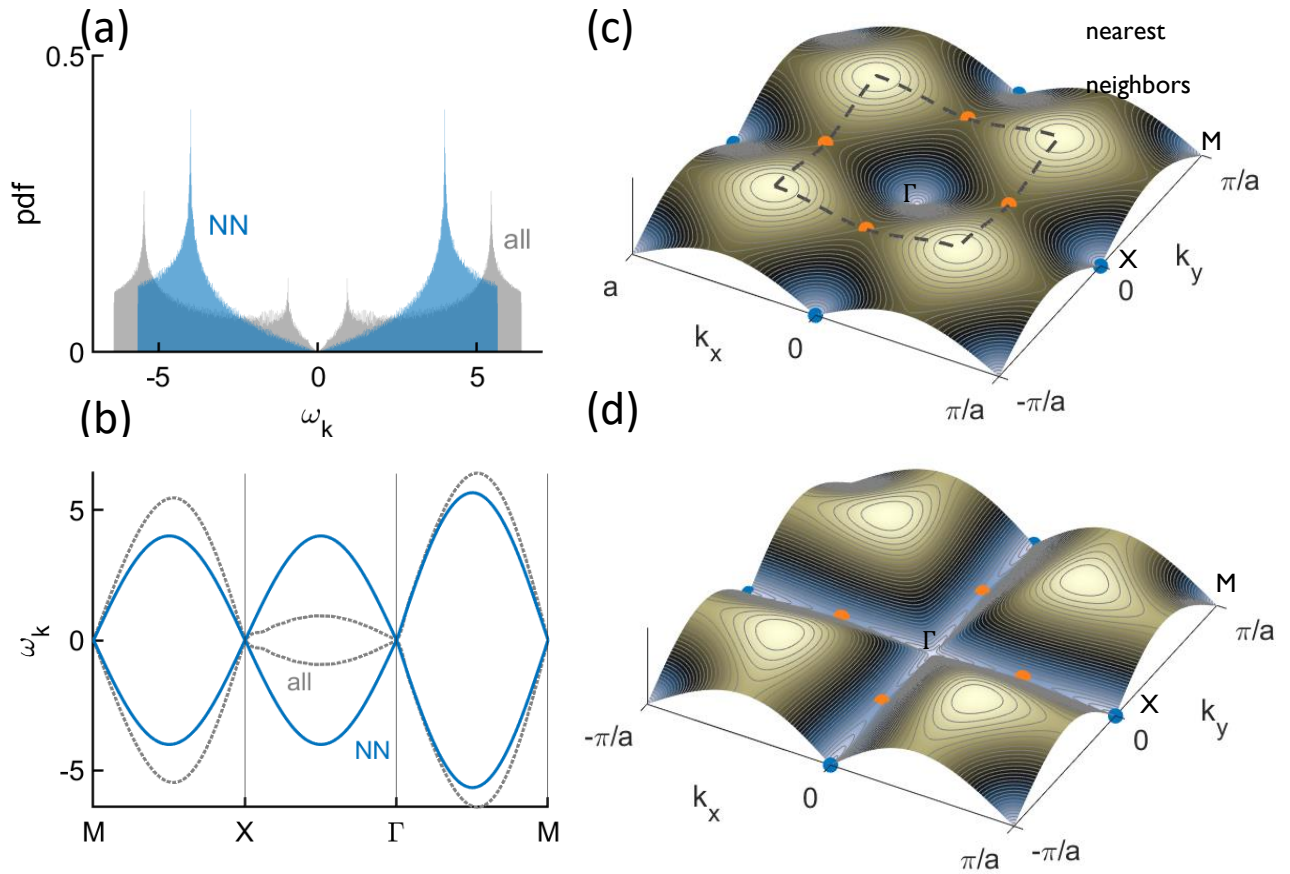
Figure 3.4. *(a) Comparison of density of states for square lattice with all (blue) and first eight NN interactions. (b) Band structure. (c) ω_k plot for all ineteraction showing four vHS points (blue). (d) NN interaction dispersion plot.*

The periodicity of the spectrum allows one to define a smaller effective BZ (dashed black square in Fig. 3.4 c. This zone would be a primitive cell in a crystal with a doubled lattice constant, $2a$, another indication for pairing and quasiparticles. In this effective BZ, one can see the pairing mode as an optical phonon, with neighboring particles moving in opposite directions albeit, owing to the parity symmetry, the pairing modes have zero frequency, unlike standard optical phonons.

Considering all hydrodynamic interactions masks the pairing symmetry of the nearest-neighbor spectrum but preserves the topology of its critical points (Fig. 3.4 d) also verified in the simulation (Fig. 3.12). The excitations at the Dirac points are pairing modes that generate lines of pairs. The Dirac cone describes long-wavelength acoustic modes of the pair lines. Due to the parity symmetry, the forces on particles in each pair are equal, and the pairing modes, $k = k_D$, are therefore marginally stable also

when their amplitude is finite. In the nearest-neighbor spectrum, the Dirac and the acoustic cones are identical in shape, indicating the equal sound velocity of pairing modes and standard phonons (*i.e.,* the points Γ, X, and M are identical). With all interactions considered, the cones are flattened towards the center, slowing down the propagation of modes in the Γ-X direction.
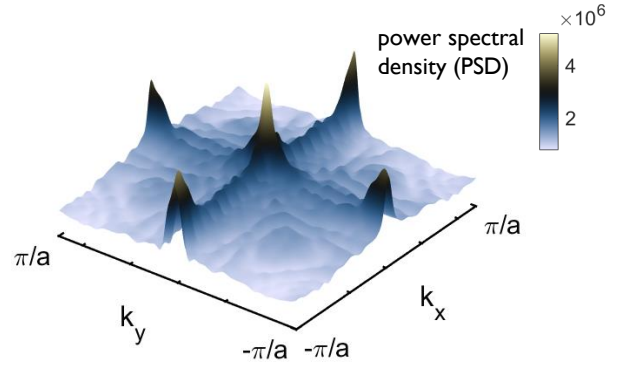

Figure 3.5. PSD *in a simulation starting from a white-noise perturbation(square lattice) shows strong selection of the pairing modes at the Dirac points.*

For their purely real frequencies, the phonons excited in the linear dynamics (Eq. (3.12)) are marginally stable. Hence, any instability or damping can only stem from the nonlinear coupling of the phonons. To examine this possibility, we followed the progression of the power spectral density (PSD) in a simulation starting with a white noise (Fig. 3.5). Evolution of the PSD indicates a strong selection of low-frequency excitations, presumably due to multi-phonon scattering events, with sharp peaks at the Dirac pairing modes.

3.4   Nearest neighbor interaction for the hexagonal crystal

Hexagonal crystals are unique as the only class of 2D Bravais lattices whose symmetry matches the intrinsic threefold symmetry of the hydrodynamic interaction bringing about a qualitatively different pathway to disorder. We consider a hexagonal arrangement as shown in Fig. 3.6, and assume that each particle interacts with its nearest neighbor only. Using Eq. (3.11) we can write
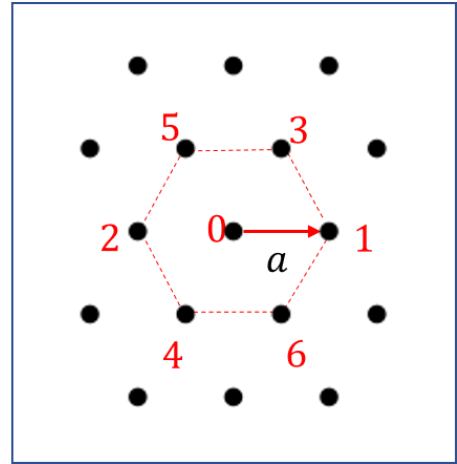
Figure 3.6. NN *interactions for hexagonal lattice*

$$\Omega_k = \begin{bmatrix} \Omega_x \\ \Omega_y \end{bmatrix} \sim 4 \left[\sin\left(\frac{a}{2} k.\hat{x}\right) - \sin\left(a \frac{1}{2} k_x - a \frac{\sqrt{3}}{2} k_y\right) - \sin\left(a \frac{1}{2} k_x + a \frac{\sqrt{3}}{2} k_y\right) \right]$$

$$\Omega_k = \begin{bmatrix} \Omega_x \\ \Omega_y \end{bmatrix} = 2 \left[\begin{bmatrix} \cos 0 \\ \sin 0 \end{bmatrix} \sin\left(\frac{a}{2} k.\hat{x}\right) + \begin{bmatrix} \cos 3\pi \\ \sin 3\pi \end{bmatrix} \sin\left(-\frac{a}{2} k.\hat{x}\right) + \begin{bmatrix} \cos \pi \\ \sin \pi \end{bmatrix} \sin\left(\frac{a}{2} k.\hat{x} + \frac{\sqrt{3}}{2} ak.\hat{y}\right) + \right.$$

$$\left. \begin{bmatrix} \cos 2\pi \\ \sin 2\pi \end{bmatrix} \sin\left(-\frac{a}{2} k.\hat{x} + \frac{\sqrt{3}}{2} ak.\hat{y}\right) + \begin{bmatrix} \cos -2\pi \\ \sin -2\pi \end{bmatrix} \sin\left(-\frac{a}{2} k.\hat{x} - \frac{\sqrt{3}}{2} ak.\hat{y}\right) + \begin{bmatrix} \cos -\pi \\ \sin -\pi \end{bmatrix} \sin\left(\frac{a}{2} k.\hat{x} - \frac{\sqrt{3}}{2} ak.\hat{y}\right) \right]$$

Therefore, the dispersion relation for the hexagonal crystal is

40

$$\omega_{\boldsymbol{k}} = \pm 8 \left| \sin\left(a\frac{1}{2}k_x\right)\left(\cos\left(a\frac{1}{2}k_x\right) - \cos\left(a\frac{\sqrt{3}}{2}k_y\right)\right)\right| \tag{3.19}$$

which exhibits a remarkable pattern of critical points (Fig. 3.7 c): (i) a single vHS is positioned exactly at the $\boldsymbol{k} = 0$ center of the BZ (point Γ), and (ii) the Dirac points (M) extend into a web of zero-frequency lines, connecting the vHSs. These Dirac cones are flattened into "wedges" stretched along the Γ-M direction.
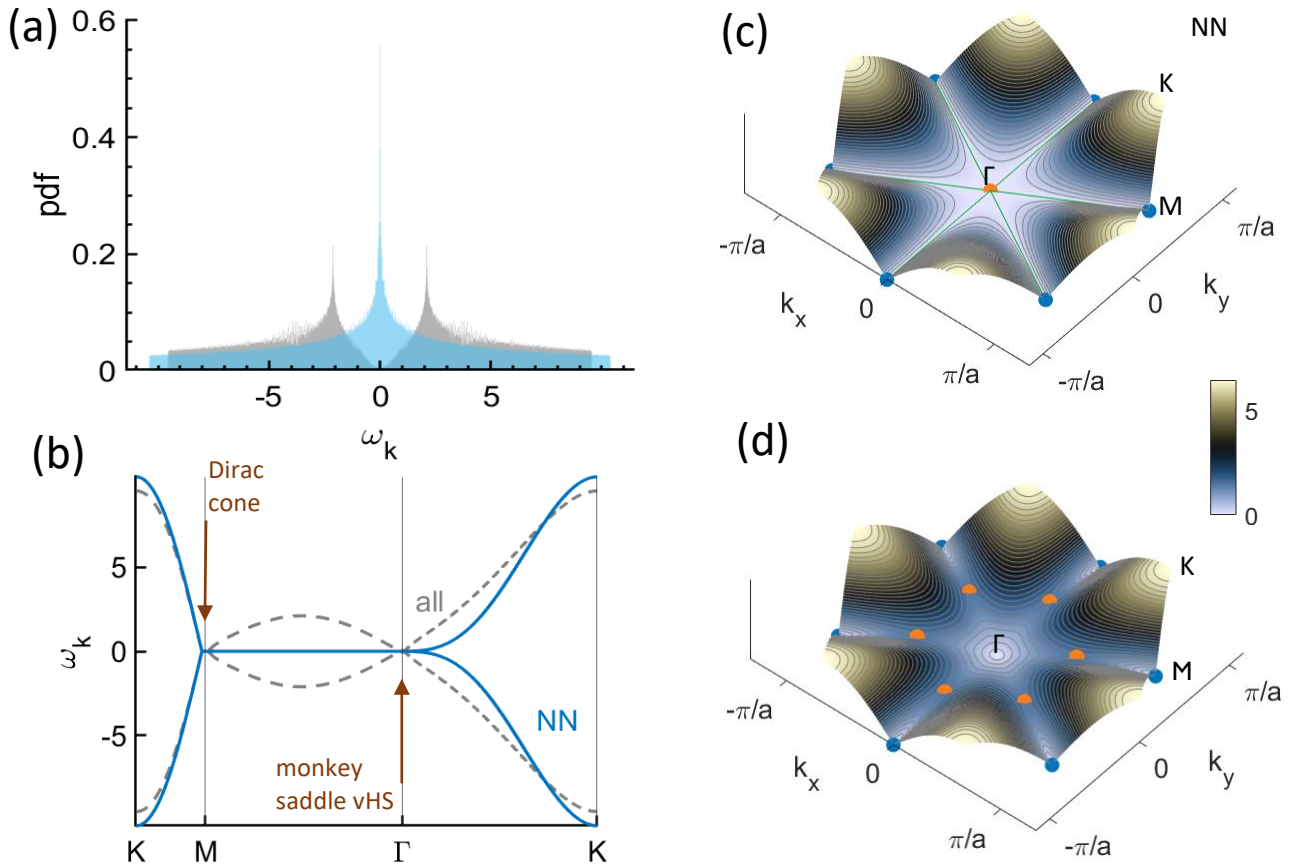
Figure 3.7. *(a) Density of states for hexagonal lattice shows power law divergence in the nearly flat band* $g(\omega)\sim\omega^{-1/3}$*. (b) Band structure comparison for NN and all interaction. (c) Dispersion plot showing first BZ, six Diract points (blue), and six standard vHS (orange). (d) Dispersion plot for NN interaction showing a "monkey saddle" vHS at the centre (orange) connected to six Dirac cones (gray).*

For Hexagonal crystals, at Dirac points $\omega_{\boldsymbol{k}} = 0$, using Eq. (3.19)

$$\left| \sin\left(a\frac{1}{2}k_x\right)\left(\cos\left(a\frac{1}{2}k_x\right) - \cos\left(a\frac{\sqrt{3}}{2}k_y\right)\right)\right| = 0$$

$$\sin\left(a\frac{1}{2}k_x\right) = 0 \rightarrow k_x = 0$$

$$\cos\left(a\frac{1}{2}k_x\right) - \cos\left(a\frac{\sqrt{3}}{2}k_y\right) = 0 \rightarrow k_x = \sqrt{3}k_y$$

$$\alpha = \tan^{-1}\left(\frac{k_y}{k_x}\right) = \pm 30^o$$

Six Dirac points occur at $(\beta_1, \beta_2) = (0, \pm 1), (\pm 1, 0), (\mp 1, \pm 1)$ for nearest neighbor interaction, as shown in Fig. 3.7. These are the midpoints of the 1st BZ edges.

Importantly, the vHS of the hexagonal crystal is a "monkey saddle" [64], a multicritical Lifshitz point where three canonical vHSs fuse into an elliptical umbilic catastrophe [65]. The long-wavelength expansion of dispersion around this vHS is $\omega_k \sim \pm k^3|\cos 3\varphi|$ (in polar coordinates $k = (k, \varphi)$), representing two interlacing monkey saddles (Fig. 3.7 b). The physical significance of the monkey saddle is the formation of a nearly-flat band with vanishing group velocity and curvature, $\partial_k\omega = \partial_k^2\omega = 0$. The outcome is a power-law divergence of the density of states $g(\omega) \sim \omega^{-\frac{1}{3}}$ (Fig. 3.7 a), much stronger than the

Figure 3.8. PSD for hexagonal lattice in a simulation starting from a white-noise.

logarithmic divergence at canonical vHSs. Due to such extreme slowing down of the excitations occurring in flat bands, multicritical and extended vHSs are known to induce strong correlations and were proposed as a mechanism underlying high-Tc superconductivity [65-70].

With all long-range interactions included, the symmetry of the double monkey saddle is broken, as it splits into six canonical vHSs, and the Dirac cones regain their standard shape. Nevertheless, the band remains relatively shallow in the Γ-M direction (Fig. 3.7 d), as verified in the simulation (Fig. 3.13). The evolution of the power spectral density (PSD) in a simulation starting with a white noise exhibits strong amplification of slow excitations in the flat band around the saddle-monkey vHS (Fig. 3.8).

Following the progression of a hexagonal hydrodynamic lattice, we see a melting transition governed by the flat band. The dominant modes that appear in the structure factor $S(\boldsymbol{k})$ at the time of the melting transition are long-wavelength excitations sitting in the monkey saddle around each Bragg peak (Fig. 3.10). This flat band spectrum is amplified as the system approaches the melting transition, as manifested in the widening peaks (most notably at t=10τ), in comparison the square lattice (Fig. 3.9), a radial modulation emerges and eventually becomes the structure factor of the disordered phase.

3.5   Structure factor for the square and hexagonal lattice.

The observation of pairing phenomena in both disordered and ordered phases puts forward a possible role of these excitations in the emergence of disorder. To examine this hypothesis, we performed numerical simulations, starting from a perfectly ordered crystal and following the progression of its structure and dynamics (Fig. 4.6 & 4.7). At each time step, the structure factor $S(\boldsymbol{k})$, the squared Fourier transform of the configuration, and its angular-averaged form $S(k) = \langle S(\boldsymbol{k}) \rangle_{|\boldsymbol{k}|=k}$ are evaluated. In crystals, the natural timescale is $\tau = \frac{a^3}{uR^2}$, the typical time it takes a perturbation to propagate a distance a. At first, only Bragg peaks are noticeable in the structure factors $S(\boldsymbol{k})$ and $S(k)$. After a typical time of a few τ, peaks emerge at the Dirac cones (the midpoints X between the Bragg peaks), which correspond to the acoustic pairing spectrum. The emergence of these Dirac peaks concurs with the appearance of a ring-shaped modulation in $S(\boldsymbol{k})$ and $S(k)$. As the melting progresses, this annular pattern reveals itself as the structure factor of the disordered system, fittingly peaking at $k = \frac{\pi}{R}$ corresponding to the particle's hardcore diameter $2R$. Altogether, this demonstrates the link between the pairing phenomena in the crystal and the emergence of the disordered phase, and the significant role of quasiparticle excitations in this non-equilibrium melting transition. The structure factor $S(\boldsymbol{k})$ is computed by transforming each frame of particle configuration into a high-resolution image, where each particle is represented by a small circle of diameter $l = 2R$, to avoid the effects of the form factor. Then, the squared modulus of the Fourier transforms of the image yields $S(\boldsymbol{k})$. At the beginning of the simulation, only the Bragg peaks corresponding to the perfect crystal are apparent. For example, the peaks of the square lattice are at $k = \left(\frac{\pi}{a}\right)\{2m, 2n\}$ for all integers m and n. As the dynamics progress, the amplitude of the Bragg peaks decreases, and other patterns emerge, most importantly peaks at the Dirac cones or flat bands. In the square lattice, the Dirac points are at $k = \left(\frac{\pi}{a}\right)\{m, n\}$, where m is odd and n is even or vice versa. These correspond to the radial positions $k = |\boldsymbol{k}|$ in $S(k)$, $k = \frac{\pi}{a}\{1, \sqrt{5}, 3, \sqrt{13}, \sqrt{17}, 5, \sqrt{29}, \sqrt{37}, \sqrt{41}, \sqrt{45}, 7, \}$. After the crystal is completely melted, all these peaks vanish, and $S(\boldsymbol{k})$ is dominated by the disordered state, exhibiting an annular peak around $k = \frac{2\pi}{l}$. In this regime, the angle-averaged structure factor $S(k)$ is a Fourier transform of the radial pair correlation function, $g(r)$. To calculate the radial pair correlation function $g(r)$ in Fig. 3.11, we count the number of particles, $dn(r)$, within an annular region $2\pi r\, dr$ around each particle in the ensemble, where periodic boundary conditions are employed to avoid finite size effect. Then, the pair correlation function is computed as a double average, over all particles in the system in multiple simulations, which is normalized by the number of particles in an uncorrelated system, $g(r) = \langle dn(r) \rangle / (2\pi r\, dr \cdot \rho)$. MATLAB programs for simulation of the square, hexagonal lattice, structure factor $S(\boldsymbol{k})$, pair correlation function $g(r)$ is present in the algorithm section.
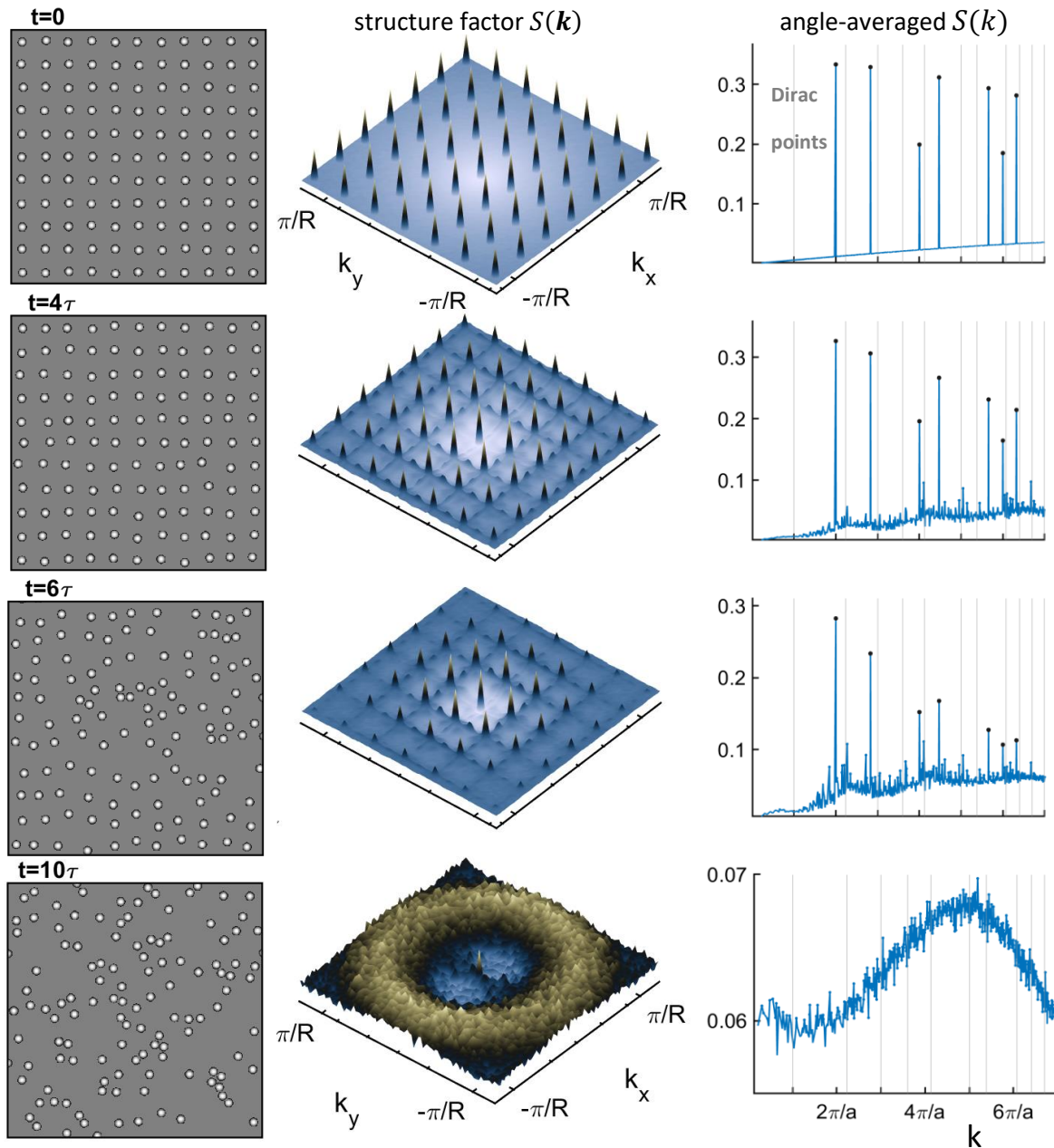
Figure 3.9. *Simulation of a square lattice with lattice constant a=5R at t=0 ,2,4 and 12τ. Left:
Real space configuration. Middle: The 2D structure factor $S(\boldsymbol{k})$. The Dirac peaks emerge in the X
midpoints between Bragg peaks. Right: angle-averaged sturcture factor $S(k)$ showing positions of
Dirac peaks (vertical gray lines) and Bragg peaks (black dots).*
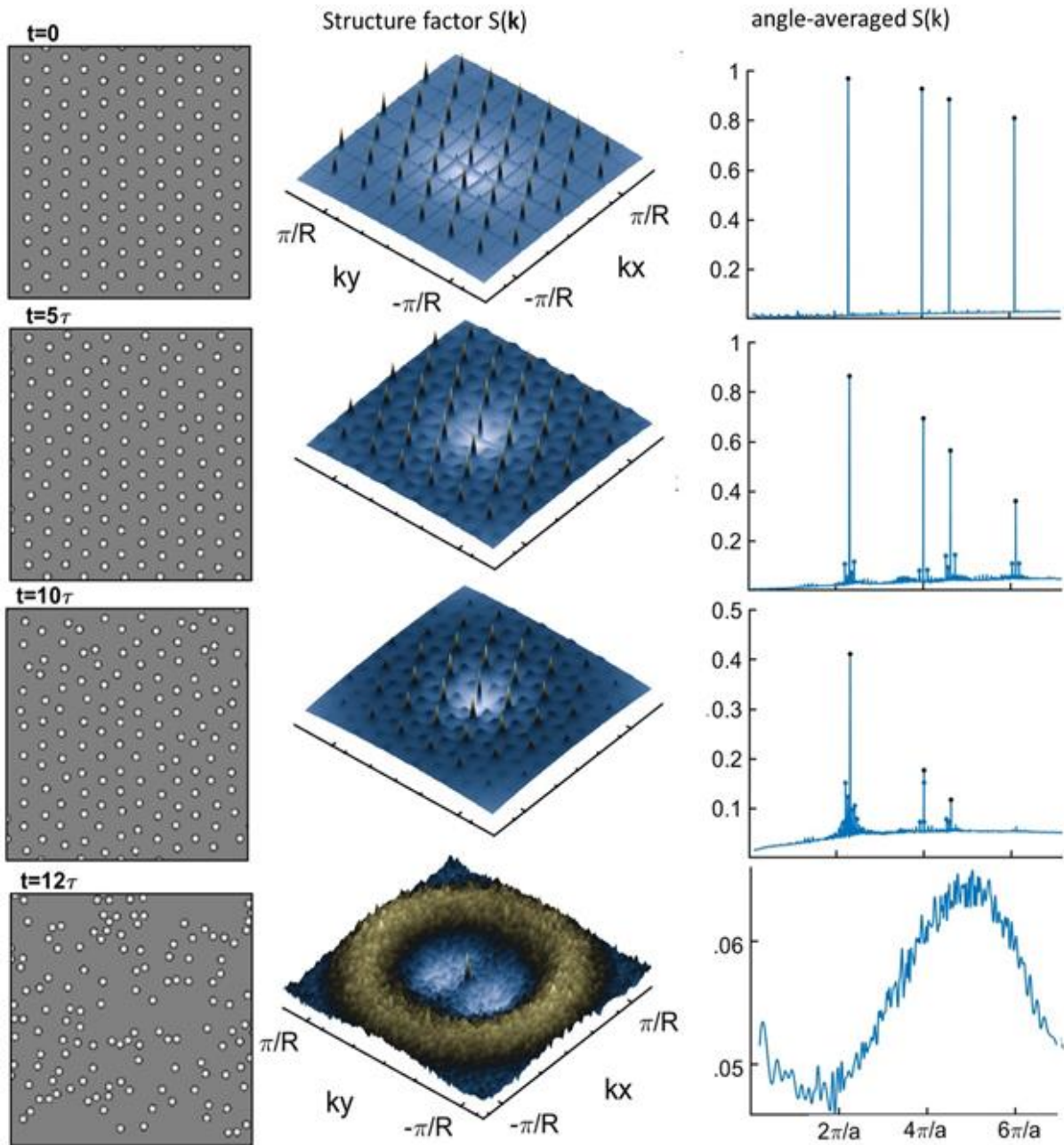
Figure 3.10. *Simulation of a hexagonal lattice with lattice constant a=5R at t=0 ;5 ;10 ;12τ. Left:*
Real space configuration. Middle: The 2D structure factor $S(\mathbf{k})$. Flat bands appear as widened peaks
around the Bragg points. Right: angle-averaged structure factor $S(k)$ with Bragg peaks denoted by
black dots. Notable are the emergent flatband modes, especially around the first peak.
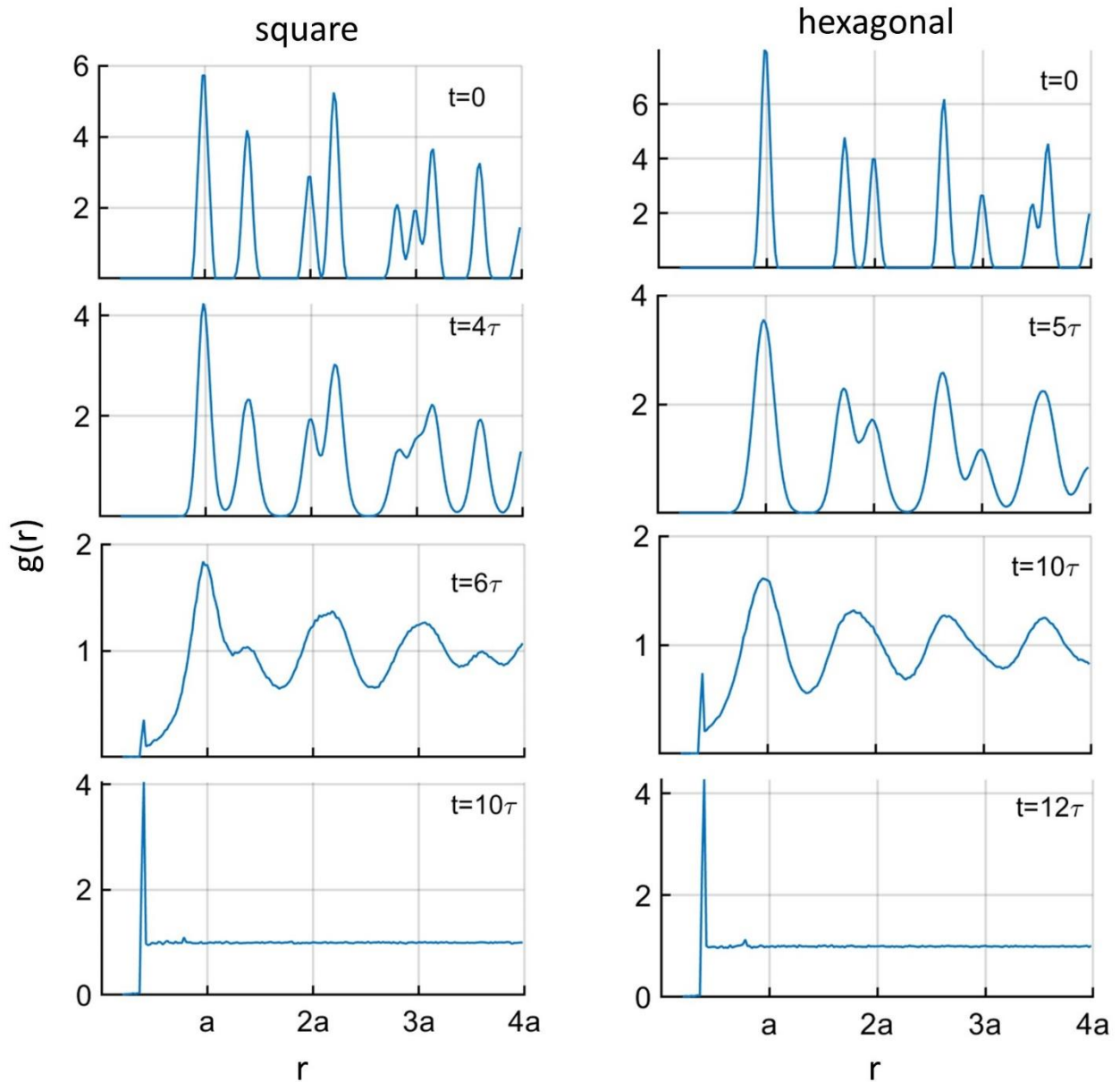
Figure 3.11. *The pair correlation function $g(r)$ computed in simulations of square (left) and hexagonal (right) lattices. Times are measured in units of $\tau = \frac{a^3}{ul^2}$. Both lattices include 51×51 particles.*

3.6 Pair-induced melting

To gain further insight into the path to melting, we simulated the dynamics of a perfect crystal doped with a single defect (an isolated quasiparticle (Figs. 3.13-14)). This quasiparticle defect functions as a single excitation in a perfect crystal which is a ground state. Dirac quasiparticle is coasting horizontally while exciting an avalanche of new quasiparticles, mostly arranged in pairing waves (i.e., Dirac phonons with $k = k_D$). This "Mach cone" of pairing is trailing behind the original quasiparticle that traverses

the crystal supersonically. This is because the defect quasiparticle is a finite-amplitude disturbance, which moves faster than sound due to hydrodynamic interaction (whose traveling speed is the Dirac velocity, the slope of the Dirac cone). The ~45° angle of the cone indicates a Mach number of ~1.4. After about 6τ, a pair-rich band stretches along the crystal. Then, collisions among pairs and phonons eventually lead to the breakup of any remaining crystalline order and the emergence of a fully developed random phase. This melting process is driven by anharmonic terms in the equations of motion, beyond the linear Schrodinger equation in Eq. (3.10). The emergence of Dirac peaks in $S(\boldsymbol{k})$ and quasiparticle avalanches reveal the pairing as the mechanism inducing the non-equilibrium melting transition.

We also followed the evolution of a hexagonal crystal (Fig. 3.14) doped with a single pair. Unlike the quasiparticle avalanche in the square crystal in Fig. 3.13, the pair remains to wobble around its original position, surrounded by a sea of excited flat-band phonons, for an extended period of ~20τ. The quasiparticle stays put due to the ultraslow group velocity in the flat band $\partial_k \omega = 0$. Then, many pairs rapidly emerge, presumably via multi-phonon collisions, inducing a swift melting of the crystal.

The more collective nature of the transition is a sharp change in the slope of exponential growth of the disorder parameter, the mean square deviation (MSD) from the crystal positions (Fig. 3.12 a). In comparison, the MSD of the square lattice grows continuously and super-exponentially. The square crystal MSD curves overlap when scaled by $\tau \sim a^3$. In contrast, the hexagonal MSD curves overlap when normalized by a timescale $\tau \sim a^{7/2}$ (Fig. 3.12 b), another manifestation of the dissimilar nature of these two melting transitions
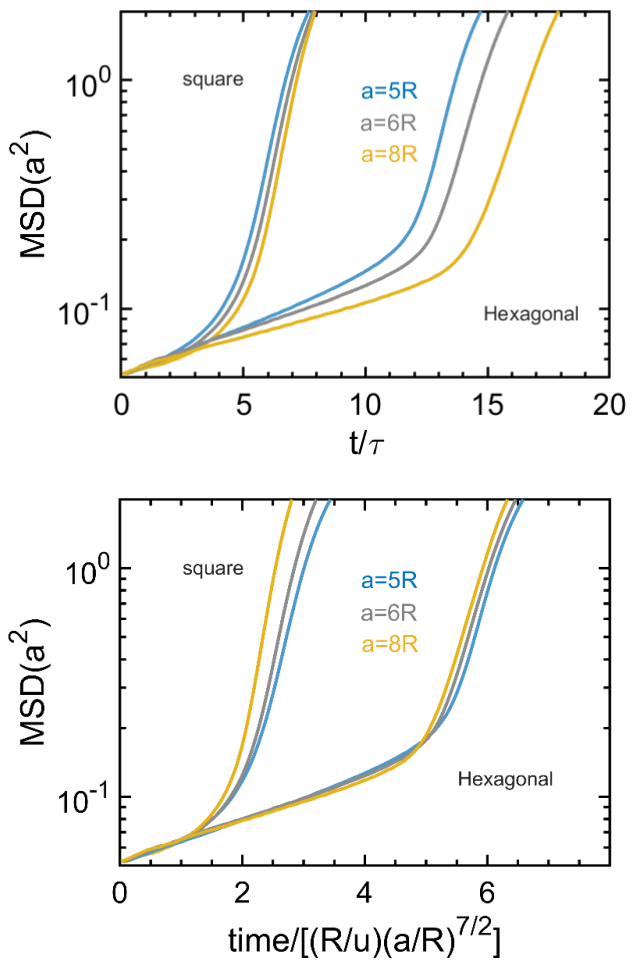
Figure 3.12. Progression of the mean square deviation (MSD) in square and hexagonal crystals for a= 5, 6 and 8R. *(a)* Time is measured in units of $\tau = a3/(ul^2)$. *(b)* Time is measured in units of $(R/u)(a/R)^{7/2} = \tau(a/R)^{1/2}$.
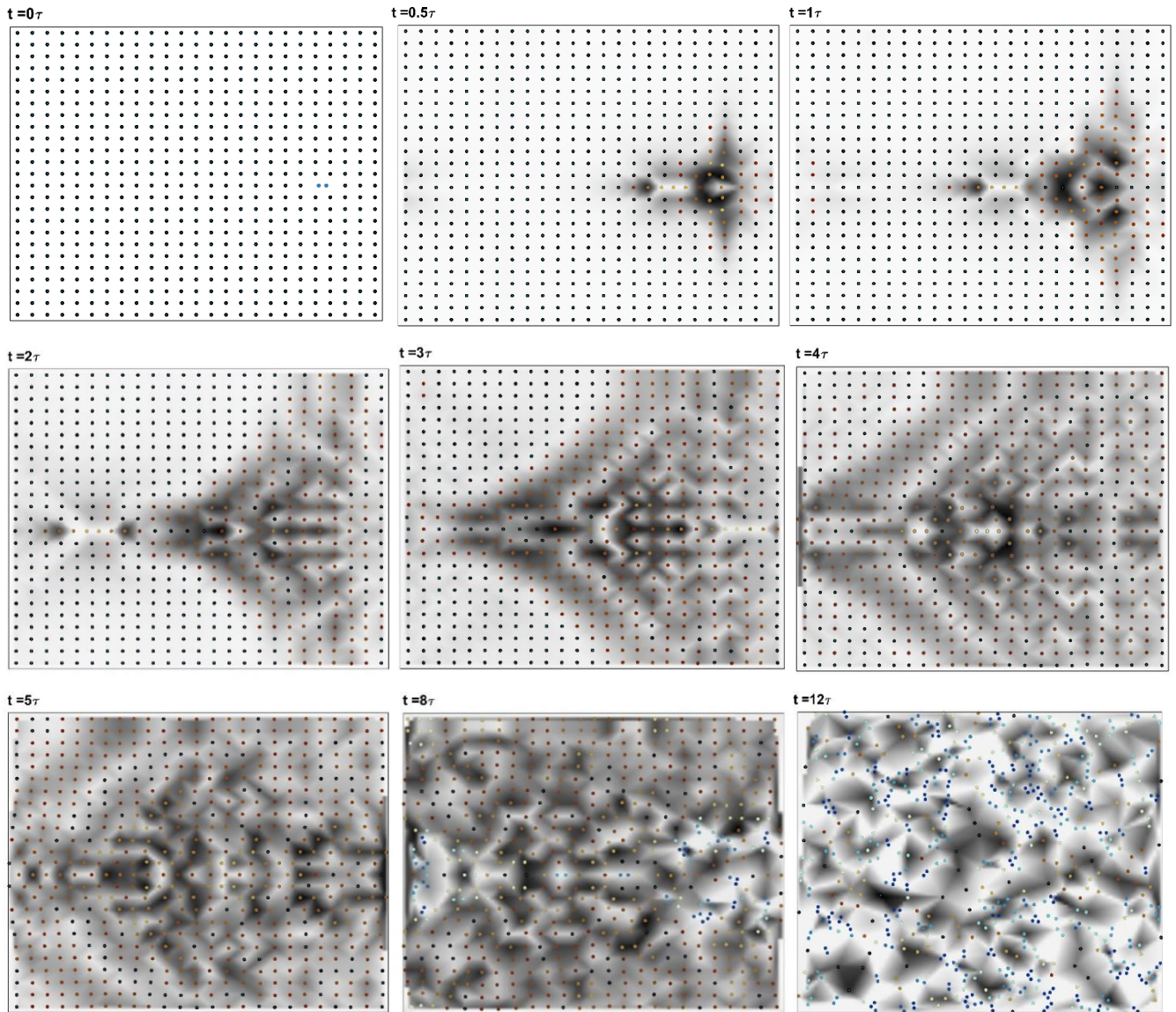
Figure 3.13 *Time evolution of square crystal with a single horizontal pair defect. The Dirac quasiparticle is coasting horizontally while exciting an avalanche of new quasiparticles, mostly arranged in pairing waves. "Mach cone" of pairing is trailing behind the original quasiparticle.*
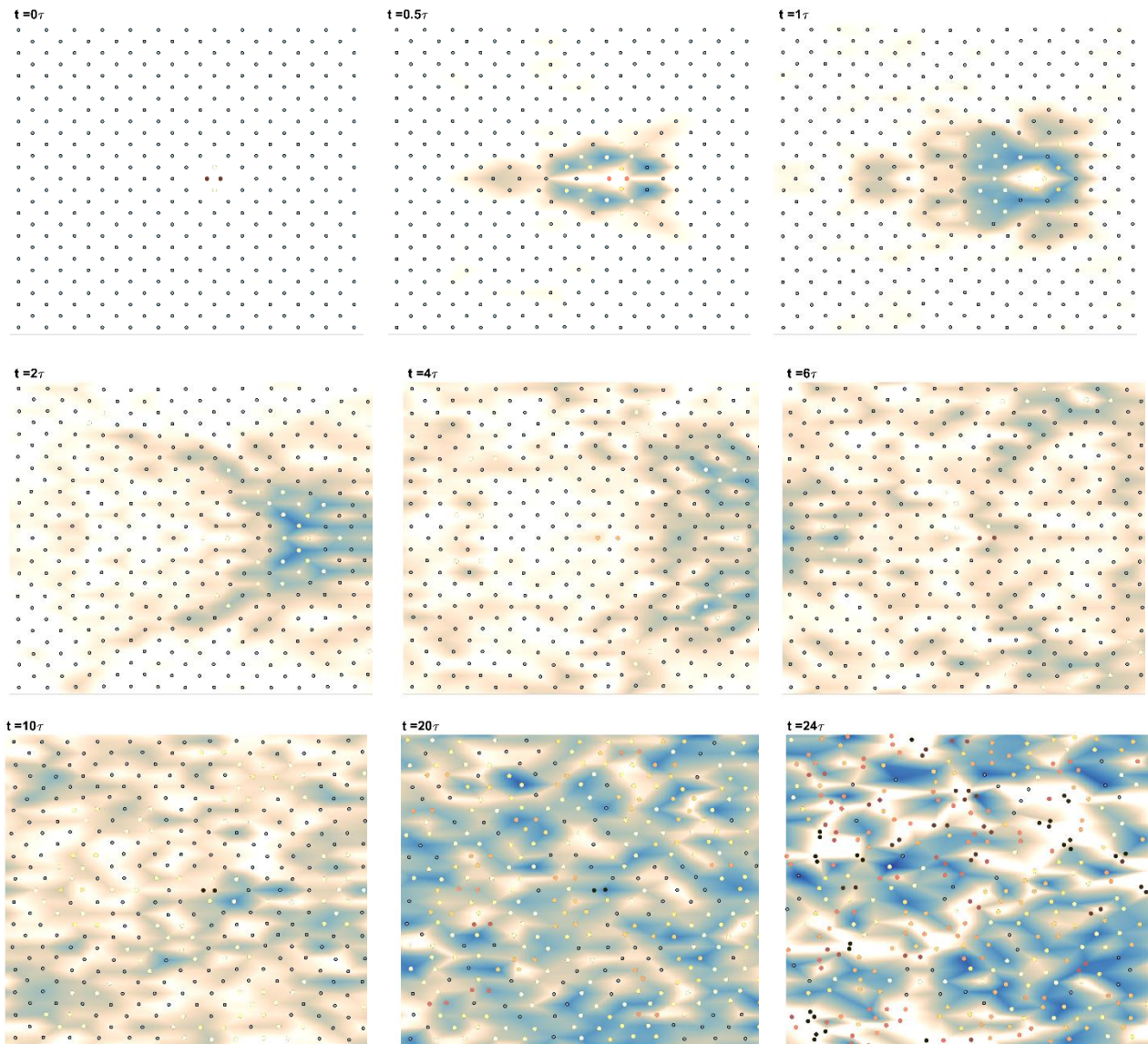
Figure 3.14 *Time evolution of hexagonal crystal with horizontal pair defect at the centre of the crystal. Pair remains wobbling around the original position exciting a sea of flat band phonons for extended period ~20τ .*

3.7   Dispersion modes in square and hexagonal lattices.

Dispersion spectrum and power spectral densities for square and hexagonal lattices are obtained by simulating the fluctuations of crystal arrangement for a finite amount of time such that lattice nodes remain stable. Fourier transform of the lattice deviations from the mean positions (or nearest neighbor distances) yields two three-dimensional arrays (2D in k and 1D in ω). Figures 3.15-16 show dispersion plots (Top) and corresponding maximal power spectral density $PSD\left(k_{xx}, k_{xy}, \omega\right)$ for each k_{xx}, k_{xy}. These results verified the analytical findings in Section 3.2.
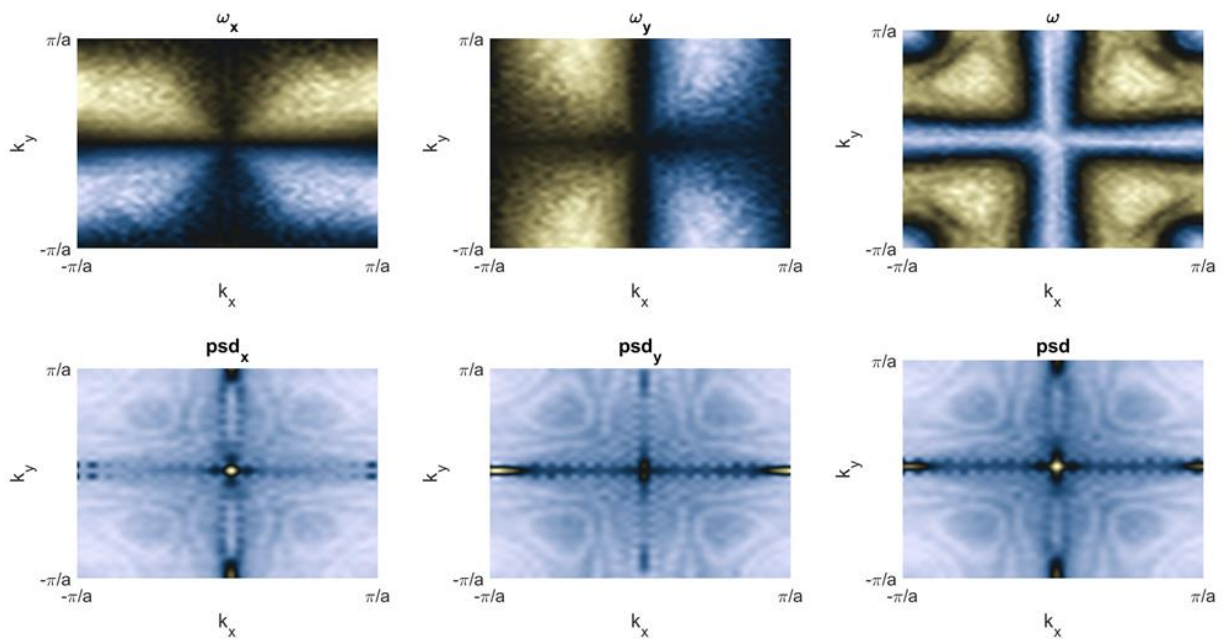
Figure 3.15. Top: dispersion spectrum for square lattice, computed using deviation method. Bottom: corresponding power spectral densities.
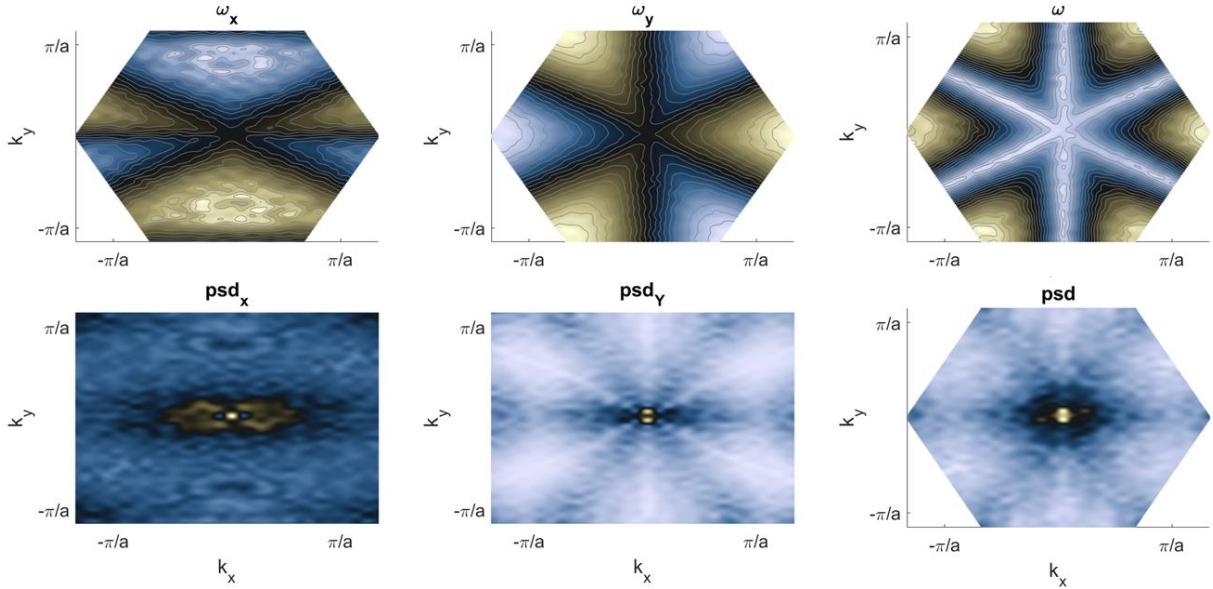
Figure 3.16. *Top: dispersion spectrum for hexagonal lattice plotted using deviation method. Bottom: corresponding power spectral densities showing peaks around k=0.*

3.8 Dirac cones

Dirac cones, named after Paul Dirac, are features that occur in some electronic band structures that describe unusual electron transport properties of materials like graphene and topological insulators. In these materials, at energies near the Fermi level, the valence band and conduction band take the shape of the upper and lower halves of a conical surface, meeting at what are called Dirac points. Dirac cones are a forbidden crossing point, where the energy of valence and conduction bands are not equal anywhere in the two-dimensional lattice k-space except at zero-dimensional Dirac points. As a result of the cones, electrical conduction can be described by the movement of charge carriers which are massless fermions. Dirac systems are characterized by a band-crossing point, from which the bands disperse linearly. Therefore, to see the Dirac cones, one can expand Eq. (3.11) around the Dirac point.

$$\Omega_k \sim \Omega_{k_D} + \nabla_k \Omega_k . dk = \nabla_k \Omega_k . dk \text{ , where } \Omega_{k_D} = 0 \text{ and } dk = k - k_D$$

$$\Omega_x \sim \boldsymbol{\nabla}_k \Omega_x \equiv \begin{bmatrix} c_{xx} \\ c_{xy} \end{bmatrix} = 2 \sum_{j \neq 0} (-1)^{\beta_1 \alpha_1^j + \beta_2 \alpha_2^j} \begin{bmatrix} \cos \theta_j \\ \sin \theta_j \end{bmatrix} \frac{\cos 3\theta_j}{\bar{r}_j^2} \tag{3.20}$$

$$\Omega_y \sim \nabla_k \Omega_y \equiv \begin{bmatrix} c_{yx} \\ c_{yy} \end{bmatrix} = 2 \sum_{j \neq 0} (-1)^{\beta_1 \alpha_1^j + \beta_2 \alpha_2^j} \begin{bmatrix} \cos \theta_j \\ \sin \theta_j \end{bmatrix} \frac{\sin 3\theta_j}{\bar{r}_j^2} \tag{3.21}$$

51

In this calculation, we consider all hydrodynamic interactions. Here, the α_1^j and α_2^j are the indices of the lattice positions, $r_j = \alpha_1^j a_1 + \alpha_2^j a_2$, with the basis vectors, a_1 and a_2. Since the gradients at the Dirac point are orthogonal, $\nabla_k \Omega_x \cdot \nabla_k \Omega_y = 0$, the resulting cone satisfies the equation $\omega_k^2 = \left(c_{xx}^2 + c_{yx}^2\right)dk_x^2 + \left(c_{xy}^2 + c_{yy}^2\right)dk_y^2$. Therefore, the shape of the Dirac cone for square crystal is elliptic. For hexagonal crystals, at Dirac points $\omega_k = 0$, using Eq. (3.18).

3.9   Van Hove singularities and density of states

Van Hove Singularity (vHS) is a singularity (non-smooth point) in the density of states (DOS) of a crystalline solid. The wavevectors at which the singularities occur are often referred to as critical points of the Brillouin zone. For three-dimensional crystals, they take the form of kinks (where the density of states is not differentiable). The most common application of the vHS concept comes in the analysis of optical absorption spectra. The occurrence of such singularities was first analyzed by the Belgian physicist Léon van Hove in 1953 for the case of phonon densities of states. vHS points are located at the saddle points on which DOS diverges. Therefore, group velocity vanishes at vHS point.

$$v_g = \nabla_k \omega = 0 \tag{3.22}$$

For square crystals, using Eq. (4.17) we can write

$$\frac{\partial \omega}{\partial k_x} = \frac{1}{2}\left(\sin^2 k_x + \sin^2 k_y\right)^{-\frac{1}{2}} \sin 2k_x = 0 \tag{3.23}$$

$$\frac{\partial \omega}{\partial k_y} = \frac{1}{2}\left(\sin^2 k_x + \sin^2 k_y\right)^{-\frac{1}{2}} \sin 2k_y = 0 \tag{3.24}$$

$$\Rightarrow \sin(2k_x) = 0, \quad \sin\left(2k_y\right) = 0$$

Thus $v_g = 0$ occurs at $(k_x, k_y) = (0,0), \left(\pm\frac{\pi}{2}, 0\right), \left(0, \pm\frac{\pi}{2}\right), \left(\pm\frac{\pi}{2}, \pm\frac{\pi}{2}\right)$. The saddle points (Fig. 3.17) are the group of points on a two-dimensional surface where the slopes in the orthogonal direction are all zero, but not a local extremum. For a given real-valued function $z = f(x, y)$ at the saddle point Hessian matrix $M = \begin{bmatrix} f_{xx} & f_{xy} \\ f_{yx} & f_{yy} \end{bmatrix}$ is indefinite implying xMx^T is neither positive nor negative for any arbitrary column vector x. To compute the Hessian matrix for the above result we need to further evaluate $\omega_{xx}, \omega_{xy}, \omega_{yx},$ and ω_{yy} using Eqs. (3.23) and (3.24) for the above set of points.

(a) Saddle Point
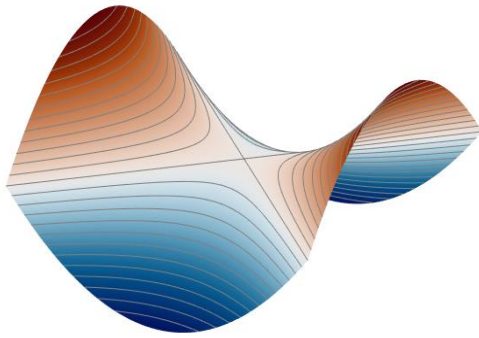
(b) Monkey Saddle
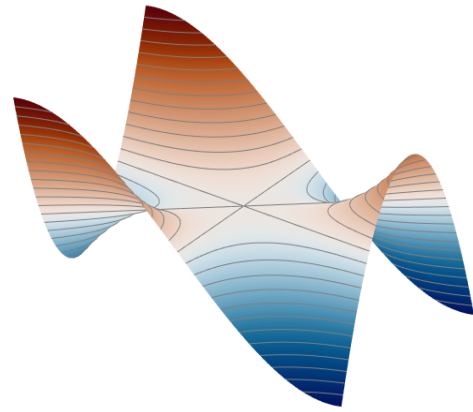
Figure 3.17. *(a) Function $z = x^2 - y^2$ has a saddle point at (0,0), where gradient vanishes in both orthogonal directions. However, it is not local extremum. (b) Function $z = x^3 - 3xy^2$ has a monkey saddle point at (0,0) where Hessian matrix becomes indefinite.*

$$\omega_{xx} = \frac{\partial^2 \omega}{\partial k_x^2} = -\frac{1}{4}\left(\sin^2 k_x + \sin^2 k_y\right)^{-\frac{3}{2}} \sin^2 2k_x + \frac{1}{2}\left(\sin^2 k_x + \sin^2 k_y\right)^{-\frac{1}{2}} 2 \cos 2k_x$$

$$\omega_{yx} = \frac{\partial^2 \omega}{\partial k_y \partial k_x} = -\frac{1}{4}\left(\sin^2 k_x + \sin^2 k_y\right)^{-\frac{3}{2}} \sin 2k_x \sin 2k_y = \omega_{xy}$$

$$\omega_{yy} = \frac{\partial^2 \omega}{\partial k_y^2} = -\frac{1}{4}\left(\sin^2 k_x + \sin^2 k_y\right)^{-\frac{3}{2}} \sin^2 2k_y + \frac{1}{2}\left(\sin^2 k_x + \sin^2 k_y\right)^{-\frac{1}{2}} 2 \cos 2k_y$$

The corresponding Hessian matrix is

$$\begin{bmatrix} \omega_{xx} & \omega_{xy} \\ \omega_{yx} & \omega_{yy} \end{bmatrix} \sim \begin{bmatrix} \cos 2k_x & 0 \\ 0 & \cos 2k_y \end{bmatrix}$$

Thus, Gaussian curvature is positive at $(0,0)$, $\left(\pm\frac{1}{2}\pi, \pm\frac{1}{2}\pi\right)$ and $\left(\mp\frac{1}{2}\pi, \pm\frac{1}{2}\pi\right)$ and negative at $\left(\pm\frac{1}{2}\pi, 0\right)$ and $\left(0, \pm\frac{1}{2}\pi\right)$. Since Hessian matrix xMx^T is indefinite at these points, the vHS points are $k_{vHS} = \left(\pm\frac{1}{2}\pi, 0\right)$ and $\left(0, \pm\frac{1}{2}\pi\right)$.

For hexagonal crystals, to find the vHS point we can make a long-wavelength (small k limit) expansion of the dispersion relation in Eq. (3.16) around $k = 0$

$$\omega_k \approx \pm 8\left|\frac{1}{2}k_x\left(1 - \frac{1}{2}\left(\frac{1}{2}k_x\right)^2 - 1 + \frac{1}{2}\left(\frac{\sqrt{3}}{2}k_y\right)^2\right)\right|$$

$$= \pm\frac{1}{2}\left|k_x(-k_x^2 + 3k_y^2)\right| = \pm\frac{1}{2}\left|k_x(k_x^2 - 3k_y^2)\right|$$

$$= \pm\frac{1}{2}\left|k^3 \cos\phi \, (\cos^2\phi - 3\sin^2\phi\right|$$

$$\omega_k = \pm\frac{1}{2}k^3|\cos 3\phi| , \quad \text{where } k = |\mathbf{k}| = \left(k_x^2 + k_y^2\right)^{\frac{1}{2}} \tag{3.25}$$

In the last equation, ω_k is proportional k^3. Therefore, ω_k is very flat around $k = 0$ and $|\omega_k|$ increases rapidly with the increase of k. Due to the presence of $|\cos 3\phi|$, there are six depressions in the azimuthal direction, suggesting two interlaced monkey saddles. Group velocity around $k = 0$ (long-wavelength limit) can be written from the above expression.

$$\omega_x = \frac{\partial\omega_k}{\partial k_x} = k_x^2 - 3k_y^2 + 2k_x^2 = 3\left(k_x^2 - k_y^2\right)$$

$$\omega_y = \frac{\partial\omega_k}{\partial k_y} = -6k_x k_y$$

$$\omega_{xx} = \frac{\partial^2\omega_k}{\partial k_x^2} = 6k_x$$

$$\omega_{xy} = \partial^2\omega_k/\partial k_x \partial k_y = -6k_y$$

$$\omega_{yy} = \frac{\partial^2\omega_k}{\partial k_x \partial k_y} = -6k_x$$

The corresponding Hessian matrix is $\begin{bmatrix} \omega_{xx} & \omega_{xy} \\ \omega_{yx} & \omega_{yy} \end{bmatrix} \sim \begin{bmatrix} 6k_x & 0 \\ 0 & -6 \end{bmatrix}$. Therefore, both the group velocity and Gaussian curvature vanish at $k = 0$. This means the vHS point is $\mathbf{k}_{vHS} = (0, 0)$. The bands around this vHS are two interlacing "monkey saddles", $\omega_{\mathbf{k}} = \pm \frac{1}{2} k^3 |\cos 3\varphi|$ with zero Gaussian curvature. Around the monkey saddle, the norm of the gradient can be written as $|\nabla_{\mathbf{k}} \omega| \cong \frac{3}{2} k^2$. The density of states around the monkey saddle diverges as a power law.

$$g(\omega) = \left(\frac{a}{2\pi}\right)^2 \iint \delta(w - \omega(\mathbf{k})) \, dk_x dk_y \tag{3.26}$$

$$= \frac{3}{2\pi^2} \int \frac{dk_\omega}{|\nabla_{\mathbf{k}} \omega|} = \frac{3}{2\pi^2} \int \frac{dk_\omega}{\frac{3}{2} k^2} = \frac{1}{\pi^2} \int \frac{dk_\omega}{k^2} \sim \int \frac{\omega^{-\frac{2}{3}} d\omega}{\omega^{\frac{2}{3}}}$$

$$g(\omega) \sim \omega^{-\frac{1}{3}}, \tag{3.27}$$

Power-law divergence of DOS here is much stronger than the typical logarithmic divergence at vHS in 2D crystals.

3.10 Comparison of hexagonal lattice spectrum with graphene

The present findings demonstrate that quantum matter concepts - quasiparticles, van Hove singularities, and flat bands provide insight into the many-body dynamics of a classical dissipative system. It is instructive to consider the similarities and dissimilarities to graphene. The hydrodynamic interactions in the flowing crystal yield Dirac cones as in graphene. However, the cones are the outcome of the intrinsic parity symmetry of the hydrodynamic force, f($-r$) = f(r), whereas, in graphene, the cones result from the crystal symmetry of the honeycomb lattice, which consists of two interpenetrating hexagonal lattices. Thus, the analog of the graphene pseudo-spin is the
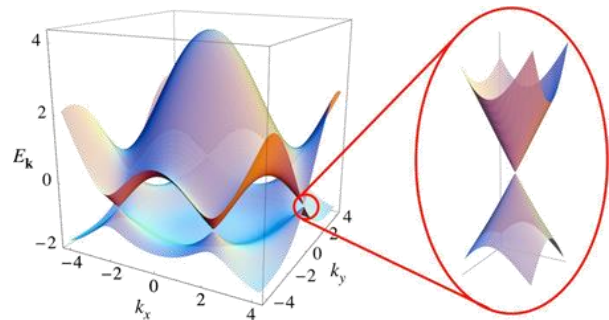
[Castro Neto et al. 2011]
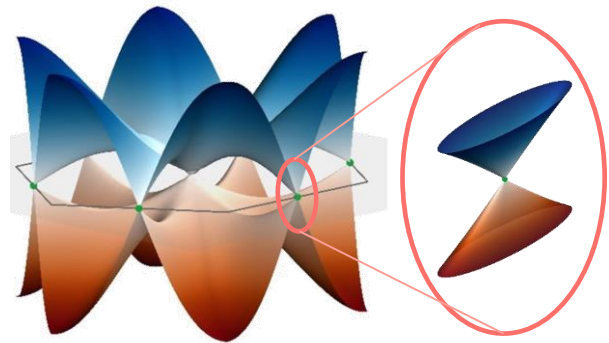
Figure 3.18. *Top: graphene energy spectrum and energy bands close to one Dirac point. Bottom: hexagonal lattice band structure*

polarization vector of the excitations ψ_k. The different underlying symmetries give rise to distinct spectra. In graphene, the vHSs occur on the boundary of the BZ, at the M points, and the Dirac cones are at the K corners. In the hydrodynamic hexagonal lattice, however, vHSs occur inside the BZ and Dirac cones occur at M points.

3.11 Discussion

Exact solutions for the steady-state motion of a pair, of finite-size spheres, were found in the 20th century [6,71] (the 21st for a quasi-2D geometry. [30,72]). But it is tempting to assume that the stability of the pair, a direct outcome from the symmetry of the Stokes equation, was already known to Stokes himself. So, in hindsight, the hydrodynamic pairs are incredibly old classical quasiparticles. In classical condensed matter, the collision time is typically too short to allow long-lived particle-like excitations, such as the quasiparticles observed in a low-temperature quantum matter [73]. Nevertheless, the present system generates a macroscopic fraction of such particle excitations in the form of hydrodynamic pairs. The pairs are stable enough to be seen as compound particles with a well-defined velocity because, effectively, the system is a dilute ensemble of dipole-like particles, even though their interactions are mediated by the surrounding dense fluid. The flat band and the multicritical vHS exhibited in hydrodynamic crystals with threefold symmetry are of special interest in many-body physics. As demonstrated in the present system, the excitations in the flat band become extremely slow, leading to strong correlations and collective modes, which give rise to a sharper melting transition. Flat bands were recently found in bilayer graphene twisted at a specific magic angle [74] or buckled [75]. We observed similar divergences in the density of excitations of a driven hydrodynamic system, raising the possibility that other emergent many-body phenomena of 2D electronic systems may be revealed in classical dissipative settings. As for future directions, the present findings propose that quantum matter notions can be widely useful for examining emergent many-body phenomena, particularly non-equilibrium phase transitions, in a variety of classical dissipative systems, ranging from soft matter, driven [76] and active [77,78] alike, to complex plasma, [79] reaction-diffusion, [80] chemotaxis, [81,82] and ecology.

4   MATLAB PROGRAMS for COMPUTATION

4.1   Simulation code for the hydrodynamic interaction of particles

This code increments the current particle position by calculating the particle speed depending on their current position and returns the incremented positions after applying hard boundary conditions for each timestep.

```matlab
function [x,y]=Sim_1(x,y,dt,L,W,Tstep)
%x, y are column vectors containing particle coordinates
%L,W are the length/width of the channel
% dt=R/u_iso with u_iso=1,
% Tstep, Total no of Time steps for which particle positions are incremented
N=length(x);
xk=zeros(1,N);
yk=zeros(1,N);
% xk  is column vectors to store \sum(x^2_ij-y^2_ij/r^4_ij
% yk  is column vectors to store \sum(2*x_ij*y_ij/r^4_ij
for jj=1:Tstep
   % repeat calculation for required no of Tstep
for i=1:N
   % N-Particles
   xm=x-x(i);  % shifting origin to particle position.
   ym=y-y(i);  % shifting origin to particle position.
    for j=1:N
    %  avoiding edge effect on particles near the edges.
   if xm(j)>L/2, xm(j)=xm(j)-L;  end
   if ym(j)>W/2, ym(j)=ym(j)-W;  end
   if xm(j)<-L/2, xm(j)=L+xm(j); end
   if ym(j)<-W/2, ym(j)=W+ym(j); end
   end
     rm=(xm.^2+ym.^2);
     rm(rm<4)=4; %diameter square, hard boundary 1
     xy=2.*xm.*ym./rm.^2;      xx=(xm.^2-ym.^2)./rm.^2;
    xx(i)=[];  xy(i)=[];     xk(i)=sum(xx);     yk(i)=sum(xy);
  end
```

```matlab
% incrementing particle positions
x=x-xk.*dt;
y=y-yk.*dt;
 % periodic boundary conditions,
for i=1:N
if x(i)>L, x(i)=x(i)-L; end
if y(i)<0, y(i)=W+y(i); end
if y(i)>W, y(i)=y(i)-W; end
if x(i)<0, x(i)=L+x(i); end
end
end
%Preventing particles from fusing into each other.
[x,y]=hard_boundary(x,y);
end
function [x,y]=hard_boundary(x,y)
n=length(x);
cc=0;
% checking for first neighbor distance
r1=FirstNeigh(x,y)
rm=min(r1);
while rm<2
for i=1:n
dx=x-x(i); dy=y-y(i);
r=(dx.^2+dy.^2).^0.5;
r(i)=1000;
[rm,j]=min(r);
   if rm<2
     dx=x(j)-x(i); dy=y(j)-y(i);
    [the,~]=cart2pol(dx,dy);
     xd=2*cos(the);      yd=2*sin(the);
     x(j)=x(i)+xd;       y(j)=y(i)+yd;
     dx=x-x(j);          dy=y-y(j);       r=(dx.^2+dy.^2).^0.5;
      r(i)= max(r);      [rm,k]=min(r);
   if rm<2
       dx=x(k)-x(j);     dy=y(k)-y(j);
        [the,~]=cart2pol(dx,dy);
```

```matlab
        xd=2*cos(the);        yd=2*sin(the);        x(k)=x(j)+xd;        y(k)=y(j)+yd;
    end
    end
end
% checking for first neighbor distance
r1=FirstNeigh(x,y);
rm=min(r1);
cc=cc+1;
if cc>20, rm=2; end
% avoiding the possibility of indefinite repetition
end
end
function r1=FirstNeigh(x,y)
n=length(x);
r1=x;
for i=1:n
   dx=x-x(i); dy=y-y(i);   r=(dx.^2+dy.^2).^0.5;
   r(i)=[];   r1(i)=min(r);
 end
end
function [x,y,ay,L,W]=Triangular(n,ax)
% Generate triangular assembly of particles,
% return column vectors x,y containing particle coordinates.
% n is the number of particles in a single row with the period ax
% L, W are length and width of assembly, ay is period in the y direction.
ay=ax*sqrt(3);
x=0:ax:n*ax; y=0:ay:n*ay;
[x,y]=meshgrid(x,y);
y1=y+ay/2;   x1=x+ax/2;
y2=y+ay; x2=x+ax; nt=2*(n+1);
x=zeros(nt,n+1); y=zeros(nt,n+1); k=1;
for i=1:2:nt
   x(i,:)=x1(k,:);   x(i+1,:)=x2(k,:);   y(i,:)=y1(k,:);   y(i+1,:)=y2(k,:);   k=k+1;
end
x=x(:); x=x'; y=y(:);   y=y'; L=ax*(n+1); W=ay*(n+1);
end
```

4.2 Structure factor by an imaging method

This code converts the configuration of particles to k-space image. Eliminate particle finite size effect while keeping the resolution in the real space (Fig 3.9-10).

```matlab
function [kx,ky,fx]=fourierspace(x,y,L,W,sf)
% Generating an image from particle data
% Image size= Length*Width*Scalingfactor
% Particle Size = Scaling Factor/2
ImgGen=image_gen(x,y,L,W,sf);
%% Fourier transform
fx=fft2(ImgGen);  [m,n]=size(fx);
fx=abs(fx); fx=fx/(n*m);  fx=fftshift(fx);
 %% Defining kx,ky
m1=floor(m/2); kx=(-m1:m1).*(2*pi*sf/m);
if length(kx)>m,   kx(end)=[];  end
n1=floor(n/2); ky=(-n1:n1).*(2*pi*sf/n);
if length(ky)>n,   ky(end)=[]; end
%% Truncating kx>pi, ky>pi to avoid any wavelength shorter than particle Size
km=pi;
xin=abs(kx+km); [~, in]=min(xin); kx(1:in-1)=[]; fx(1:in-1,:)=[];
xin=abs(kx-km); [~, in]=min(xin); kx(in+1:end)=[]; fx(in+1:end,:)=[];
xin=abs(ky-km); [~, in]=min(xin); ky(in+1:end)=[]; fx(:,in+1:end)=[];
xin=abs(ky+km); [~, in]=min(xin); ky(1:in-1)=[]; fx(:,1:in-1)=[];
end


function b=image_gen(x,y,s,w,sf)
 x=x.*sf; y=y.*sf; s=s*sf; w=w*sf;
 s=ceil(s); w=ceil(w);  b=zeros(s,w);
r=sf/2; % particle size
for j=1:length(x)
cx=round(x(j)); cy=round(y(j)); spx=cx-sf; fpx=cx+sf; spx(spx<1)=1; fpx(fpx>s)=s;
spy=cy-sf; fpy=cy+sf;  spy(spy<1)=1; fpy(fpy>w)=w;
for ii=spx:fpx
   dx=(ii-x(j))^2;
   for jj=spy:fpy
      cc=dx+(jj-y(j))^2;     b(ii,jj)=r^2-cc;
```

```matlab
        if b(ii,jj)<0, b(ii,jj)=0; end
    end
end
end
```

4.2.1 Angle-averaged structure factor.

```matlab
function [kk,psdk]=Psd_K(kx,ky,psd,L,W)
 % this function converts two dimensional psd(kx,ky) to psd(k)
%with k=(kx^2+ky^2).^0.5;
 [m,n]=size(psd);
xo=find(kx==0); yo=find(ky==0); k=zeros(m,n);
 for i=1
   kxi=(i-xo)*2*pi/L;
  for j=1:n
     kyj=(j-yo)*2*pi/W;
     k(i,j)=(kxi^2+kyj^2).^0.5;
   end
end
 k=k(:); tt=[k,psd]; tt=sortrows(tt,1); k=tt(:,1);
 psd=tt(:,2);  n=length(k); ck=zeros(n,1); j=1;
for i=2:n
   dk=k(i)-k(i-1);
   if dk==0
     ck(j)=ck(j)+1;
   else
     j=j+1;
   end
end
ck(1)=1; ck(ck==0)=[]; ck=ck+1; ck(1)=1;
n=length(ck); kk=zeros(n,1); psdk=kk; j=1;
for i=1:n
   sp=j; ep=ck(i)+j-1;
   kk(i)=sum(k(sp:ep))/ck(i);    psdk(i)=sum(psd(sp:ep))/ck(i);   j=j+ck(i);
end
end
```

4.3   Power spectrum

4.3.1 Square geometry.

This code converts column vectors of particle positions at a given time to a two-dimensional mesh with particles arranged in order of their x and y coordinates, Deviation of particles' first neighbors in the x and y direction from lattice position is evaluated. These two-dimensional meshes for each time step are combined into a single three-dimensional array to form time series. Fourier transform of time series gives dispersion relation and power spectrum plots (Fig 3.15-16).

```
function [dx,dy]=meshes(x,y,L)
% This function creates meshes dx, dy from column vectors x,y for the square arrangement of
particles, size of the assembly is L*L.
nx=length(x); n=sqrt(nx);
xm=zeros(n,n); ym=zeros(n,n);
k=1;
for i=1:n
   xm(i,:)=x(k:k+n-1);    ym(i,:)=y(k:k+n-1);    k=k+n;
end
dx=perturb(xm,L); dy=perturb(ym,L);
end


function dx=perturb(xm,L)
 [m,n]=size(xm);  dx=zeros(m,n);
 for i=1:n
    for j=1:m
      j2=j-1;
     if j==1, j2=m; end
      ddx=xm(i,j)-xm(i,j2);
      if (ddx)<-L/2, ddx=ddx+L;   end
      if (ddx)>L/2, ddx=ddx-L;   end
      dx(i,j)=ddx;
    end
 end
end
```

4.3.2 Triangular geometry.

```matlab
function [dx,dy]=meshes_xy(x,y)
% x,y are column vectors that contain particles coordinated in triangular
% geometry ordered with respect to particle position in the assembly.
% dx,dy are two-dimensional mesh containing near neighbor distance in x,y
% direction. For n-rows column vector triangular lattice contain sqrt(n/2) particle along both axis.
n=length(x); nc=sqrt(n/2); nr=2*nc; k=1:2:nr; kx=k; ky=1:nr:n; xm=zeros(nr,nr); ym=zeros(nr,nr);
%xm,ym are two-dimensional mesh with a triangular arrangement
for i=1:2:nr
   xm(i,kx)=x(k);    xm(i+1,kx+1)=x(k+1);
   ym(i,kx)=y(ky);      ym(i+1,kx+1)=y(ky+1);
  k=k+nr;   ky=ky+2;
end
dx=perturb(xm,L,ax); dy=perturb(ym,W,ay);
 end
function dx=perturb(xm,L,ax)
[m,~]=size(xm); dx=zeros(m,m);
for i=1:m
  ip=i+1; im=i-1;
  if i==m, ip=1; end
  if i==1, im=m; end
for j=1:m
    jj=j+1;
  if j==m, jj=1; end
  if xm(i,j)~=0
    ddx=xm(ip,jj)-xm(i,j);
  else
    ddx=xm(ip,j)-xm(im,j)-ax/2;
  end
    if ddx<-L/2,  ddx=ddx+L; end
    if ddx>L/2,  ddx=ddx-L; end
    dx(i,j)=ddx;
end
end
end
```

4.4 Radial distribution function

The following code calculates the radial distribution (Fig 3.11) for the assembly of particles in planar geometry.

```
function gr=radial_fun(x,y,rp,L,W)
%x,y are column vectors containing the coordinates of each vector
%rp is the column vector of radial distance for which gr is to be evaluated
%L,W length and width of the assembly
m=length(rp); gr=zeros(m,1); n=length(x);
rho=n*pi/(W*L); % density of particles
for i=1:n
 % xm, ym distance vectors for each particle with respect to ith particle.
xm=x-x(i); ym=y-y(i);
 %% This section transforms the structure to Periodic for avoiding the finite size effect.
for j=1:n
    if xm(j)>L/2, xm(j)=xm(j)-L;  end
    if ym(j)>W/2, ym(j)=ym(j)-W;  end
    if xm(j)<-L/2, xm(j)=L+xm(j); end
    if ym(j)<-W/2, ym(j)=W+ym(j); end
end
rm=(xm.^2+ym.^2).^0.5; rm(i)=[];
np=Particle_count(rm,rp); %counting particle density with respect to ith particle
gr=gr+np./(rho); % adding to global sum over all particles.
 end
  gr=gr./n;
end
 %%
function np=Particle_count(rm,rp)
% this function returns dn(rp)/2pi*rp*dr by counting number of particles
% around the center of ith particles for which rm is evaluated.
rm=sort(rm);  rm(rm>rp(end))=[]; n=length(rp); np=zeros(n,1);
for k=1:n-1
    dr=2*pi*rp(k)*(rp(k+1)-rp(k));    cp=rm;   cp(cp<rp(k))=[]; cp(cp>=rp(k+1))=[];
    np(k)=length(cp)/dr;
end
end
```

4.5 Density dispersion along the flow direction.

This function divides the field of view into small length elements along the flow direction and measures density in length. Fourier transform of the differential density is used to compute density dispersion for both experimental and simulation data. Results are shown in Fig 2.8.

```
function [dp,xf]=dens(xk,L,dL)
%xk is a two-dimensional array (T*N) containing particles x-coordinates in time.
%L is the length of the window. dL is the length of the small area element.
%dp is a two-dimensional array (T*n) containing the density of particles in each area element
dL,n=L/dL.
%xf is the Fourier transform of dp.
[T,N]=size(xk); n=floor(L/dL); dp=zeros(T,n);
for i=1:T
    for k=1:n
    for j=1:N
        if xk(i,j)>(k-1)*dL && xk(i,j)<=k*dL
        dp(i,k)=dp(i,k)+1;
        end
    end
    end
end
xf=fft2(dp); xf=abs(xf);
end
```

4.6 Perturbation in a one-dimensional chain along the flow direction

The following function solves the eigenmatrix Eq. (2.29). For perturbation in a one-dimensional chain of particles, results are shown in Fig 2.12.

```
function [wx,wy]=Eigen_Mat(x)
% x is a column matrix containing particle coordinates arranged in a one-dimensional chain.  wx, wy
are eigenvalues for small perturbations in velocities.
n=length(x);
xd=zeros(n,n);
for i=1:n
    for j=1:n
```

```matlab
    if j~=i
    xij=x(j)-x(i); xd(i,j)=1/xij^3;
    end
  end
end
for i=1:n
  xd(i,i)=-sum(xd(i,:));
end
xd=xd.*3/pi^2;
W=eig(xd);
%  W=W./(1i);
wx=real(W); wy=imag(W);
 end
```

4.7   Pairs horizontal and vertical velocity data.

The following functions are used to plot data for horizontal and vertical pairs as a function of inclination with the flow direction. Results are shown in Fig 2.9. Position data for each particle is stored in two-dimensional arrays xk, yk of size N, T. Function returns a data table containing velocity, pair-separation, and inclination with the flow.

```matlab
function tt=Data_table(xk,yk)
[vx,vy,r1,r2,the1,the2,L1,L2]=Pairs_data_1(xk,yk);
[N,T]=size(vx);
the2=the2.*180/pi; the1=the1.*180/pi; tt=zeros(T,10);  ii=1;
 for i=1:T-1
   for j=1:N
     k=L1(j,i);
     if r1(j,i)>0 && L1(k,i)==j
       L1(j,i)=j;          tt(ii,1)=r1(j,i);
     if abs(the1(j,i))>90 % positive inclination pairs
        tt(ii,2)=the1(k,i);   tt(ii,3)=vx(j,i);   tt(ii,4)=vx(k,i);   tt(ii,5)=vy(j,i);   tt(ii,6)=vy(k,i);
        tt(ii,7)=r2(j,i);        tt(ii,8)=r2(k,i); tt(ii,9)=the2(j,i); tt(ii,10)=the2(k,i);
     else
        % shifting origin to make to trailing particle in pair for
        % negative inclination pairs.
        tt(ii,2)=the1(j,i);   tt(ii,3)=vx(k,i);   tt(ii,4)=vx(j,i);   tt(ii,5)=vy(k,i);   tt(ii,6)=vy(j,i);
```

66

```matlab
        tt(ii,7)=r2(k,i);    tt(ii,8)=r2(j,i);    tt(ii,9)=the2(k,i);        tt(ii,10)=the2(j,i);
    end
        ii=ii+1;     r1(k,i)=0;
     end
   end
 end
  tt=sortrows(tt);  [NP,~]=size(tt);   cc=zeros(Np,1);
for i=1:NP
    tt(i,11)=(tt(i,3)+tt(i,4))/2; %  mean pair vx;
    tt(i,12)=(tt(i,5)+tt(i,6))/2;  %  mean pair vy;
    % deletion pairs
    if tt(i,7)<10, cc(i)=1; end %pairs 2nd neighbour<10R deleted
    if tt(i,8)<10, cc(i)=1; end %pairs 2nd neighbour<10R deleted
    if tt(i,1)>6, cc(i)=1; end  %pairs ist neighbour> 6R deleted
    if tt(i,1)<2, cc(i)=1; end  %pairs ist neighbour< 2R deleted
   end
    tt(cc==1,:)=[];
end
function [vx,vy,r1,r2,the1,the2,L1,L2]=Pairs_data_1(xk,yk)
%xk,yk contains particle coordinates in time
[N,T]=size(xk);
% pnx=pnx.*cali;
% pny=pny.*cali;
vx= zeros(N,T); % instantaneous horizontal velocity for each particle
vy= zeros(N,T); % instantaneous vertical velocity for each particle
r1=zeros(N,T);  % first neighbour distance for each particle
r2=zeros(N,T);  % 2nd neighbour distance for each particle
L1=zeros(N,T);   % first neighbour Label for each particle
L2=zeros(N,T);   % 2nd neighbour Label for each particle
the1=zeros(N,T); % first neighbour inclination for each particle
the2=zeros(N,T);  % 2nd neighbour inclination for each particle
for i=2:T-1
  [r1(:,i),r2(:,i),the1(:,i),the2(:,i),L1(:,i),L2(:,i)]=first_neigh1(x,y);
  vx(:,i)=xk(:,i)-xk(:,i-1);   vy(:,i)=yk(:,i)-yk(:,i-1);
end
end
```

```
%%
function [r1,r2,the1,the2,L1,L2]=first_neigh1(x,y)
N=length(x); r1=zeros(N,1); r2=zeros(N,1); the1=zeros(N,1); the2=zeros(N,1);
L1=zeros(N,1); L2=zeros(N,1);
for i=1:N
dx=x-x(i); dy=y-y(i);
rc=(dx.^2+dy.^2).^(0.5);
the=atan(dy/dx);  tt=[rc,the,1:N];
tt=sortrows(tt,1);
r1(i)=tt(2,1); r2(i)=tt(3,1); the1(i)=tt(2,2); the2(i)=tt(3,2); L1(i)=tt(2,3); L2(i)=tt(3,3);
end
end
```

4.8   Pairs auto-correlation function.

This function computes autocorrelation for pairs using Eq. (2.26). Results are shown in Fig. 2.10 for experimental and computational data.

```
% xk, yk  is the matrix of particle positions in time and space.
uiso=1;
thre=2*dt*uiso; % Max distance traversed by particles in single time step
mT=1.5*floor(L/(uiso*dt));
%L:length of field view, mT:max no of timesteps needed to travel length L
[xb,yb]=order1(xk,yk,thre);
%this function sort xk, yk to identify each particle by computing forward
%motion of a particle in a horizontal direction
pinfo=info(xb,yb,thre,mT,25);
%pinfo: table for identifying each particle while it passes Field of view.
%column 1 contains particle serial no, column 2 contains time label
%particle first tracked, column3 contains the time label when the particle passed
% out-of-field view
%mT: maximum no of time steps needed for a particle to cross the field of view.
%cT: cut off time, minimum no of time steps particle tracked sequentially
%to be qualified for the calculation of the correlation function
[r1,r2,Labels]=neigh_matrix(xb,yb);
%compute first and 2nd neighbor matrix corresponding to each xb,yb
%label identifies the location of neighbors
```

```
[CT,rm,tc]=CorrelationTable(Labels,r1,MinL,MaxR,mT);
%compute correlation table for each neighboring pair
%r1: pairs separation,
%rm mean pair distance
%tc: exponential decay time of pair correlation function
%CT: matrix of  pairs separation in time sorted in order of increasing rm
%MinL=20R pair tracked together for at least 20R
%MaxR=20R maximum pair separation to compute correlation function<20R
%%
function [xb,yb]=order1(xb,yb,thre)
[m,n]=size(xb);
for i=1:m-1
x=xb(i:i+1,:); y=yb(i:i+1,:);
for j=1:n
if x(1,j)==0, else
[jo,x,y]=find_x(j,x,y,thre);
if jo~=0
   yb(i+1,j)=y(2,jo);    xb(i+1,j)=x(2,jo);
   x(2,jo)=0;    y(2,jo)=0;
end
end
end
end
end


function [jo,x,y]=find_x(j,x,y,thre)
 dx=x(2,:)-x(1,j); dy=y(2,:)-y(1,j);
 dy(dx<=0)=10; dx(dx<=0)=10;
 r=dx.^2+dy.^2; r=r.^0.5;
 [r,jo]=min(r);
 if r>thre, jo=0;  end
 if r<=0, jo=0;  end
end
%%
 function pinfo=info(xk,yk,thre,mT,cT)
[T,N]=size(xk);  %T=Total no of time steps, N: total no of particles
```

```
pinfo=zeros(1,3);
pc=0; % particle count
for i=1:N
    j=1;
    while j<T
    if xk(j,i)~=0
    pc=pc+1; % particle count
    sT=j;  % start time
    eT=j+mT; % end time
    if eT>T, eT=T; end
    x2=xk(sT:eT,i);    y2=yk(sT:eT,i);
    eT=findeT(x2,y2,thre);  % calling function to trace the particle final time
    %before it disappears from the field of view.
    pinfo(pc,1)=i; pinfo(pc,2)=sT;  pinfo(pc,3)=eT+sT;
    j=eT+sT+1;
    else
        j=j+1;
    end
    end
end
 pinfo=DeleteParticles(pinfo,cT); %deleting particles tracked for smaller steps
 end
 function eT=findeT(x,y,thre)
% this function calculates the end time for a particle when it disappears from
% field of view
% x contains the time sequence of the particle's horizontal position.
% y contains the time sequence of the particle's vertical position.
%thre maximum distance a particle can cover in a single time step to be
%identified as the same particle, it should be chosen much as a fraction of
%particle diameter
 n=length(x);
 if n==1, eT=0;
else
r=0; dx=1; i=0;
while dx>0 && r<thre && i<n-1
    i=i+1;
```

```matlab
    dx=x(i+1)-x(i); dy=y(i+1)-y(i);
    r=dx^2+dy^2; r=r^0.5;
    end
  if i==n-1, eT=i;
    else, eT=i-1; end
 end
end
 function pinfo=DeleteParticles(pinfo,ct)
%deleting particles tracked for smaller steps
d=(pinfo(:,3)-pinfo(:,2));
pinfo(:,4)=d;
pinfo=sortrows(pinfo,4,'descend');
[n,~]=size(pinfo);
while pinfo(n,4)<ct && n>0
    n=n-1;
end
pinfo=pinfo(1:n,:);
end
%%
function [r1,r2,Labels]=neigh_matrix(xb,yb)
[T,L]=size(xb);
r1=zeros(T,L);
r2=zeros(T,L);
Labels=zeros(T,L);
xb(xb==0)=10000;
for jj=1:T
x=xb(jj,:); y=yb(jj,:);
r=zeros(L,L);
for i=1:L-1
    for j=i+1:L
        x1=x(j)-x(i);y1=y(j)-y(i);
        r(i,j)=(x1^2+y1^2)^0.5;
    end
end
    r=r'+r;
    r(r==0)=10000;
```

```matlab
    for i=1:L
    [mr,ind]=min(r(i,:));
    r1(jj,i)=mr;
    Labels(jj,i)=ind;
    r(i,ind)=10000;
    [mr,~]=min(r(i,:));
    r2(jj,i)=mr;
    end
end
end
%
%%
function [CT,rm,tc]=CorrelationTable(Labels,r1,MinL,MaxR,mT)
x=FirstNeihbourInfo(Labels,MinL,mT);
% x=First Neighboring table;
% Labels :first neighboring information in space and time
%r1: first neighbor distance
%MinL: Minimum length of time sequence pairs are together
%MaxR: Maximum Separation between the first neighbor to be evaluated
%sf: sampling frequency of observed rm
x(:,4)=x(:,3)-x(:,2);
x=sortrows(x,4);
i=1;
mt=x(i,4);
[n,~]=size(x);
while mt<MinL && i<n
   i=i+1;
   mt=x(i,4);
end
if i>1, x(1:i-1,:)=[]; end
CT=zeros(1,1);
pc=1;
for i=1:length(x)
Li=x(i,1); Ti=x(i,2); Te=x(i,3);   % selecting Particle
r=r1(Ti:Te,Li);        %
[rk,rm]=auto_correlation(r);
```

72

```matlab
    rk(rk<0.01)=[]; n=length(rk); CT(pc,1)=rm; CT(pc,2:n+1)=rk; pc=pc+1;
end
CT=DeleteRows(CT,MinL,MaxR); tc = Decaytime(CT);
rm=CT(:,1); CT(:,1)=[];
end
%%
function [rk,ym]=auto_correlation(y)
n=length(y); ym=mean(y); rk=zeros(1,n);
for k=0:n-1
    s1=y(1:n-k)-ym;    s2=y(1+k:n)-ym;    s1=s1.*s2;    rk(k+1)=sum(s1);
end
rk=rk./rk(1);
end
 function x=DeleteRows(x,MinL,MaxR)
x=sortrows(x,1); [n,~]=size(x); pc=0; DxR=zeros(1,1); m=1;
for i=1:n
    bc=0;    x1=x(i,:);    x1(x1==0)=[];
    if length(x1)>3
        if x1(2)~=1, bc=1; end
        if x1(3)<0.8, bc=1; end
        if length(x1)<MinL, bc=1; end
        if x1(1)>MaxR, bc=1; end
    else
        bc=1;
    end
    if bc==1
        pc=pc+1;        DxR(pc)=i;
    else
        if length(x1)>m, m=length(x1); end
    end
end
DxR(DxR==0)=[]; x(DxR,:)=[];
 [n,~]=size(x);
mL=1;
for i=1:n
    xr=x(i,2:end);
```

```matlab
    xr(xr<0.01)=[];
    if mL<length(xr), mL=length(xr); end
end
x(:,mL+2:end)=[];
end
 function [CT,rm,tc]=CorrelationTable(Labels,r1,MinL,MaxR,mT)
% x=First Neighboring table;
% Labels: first neighboring information in space and time
%r1: first neighbor distance
%MinL: Minimum length of time sequence pairs are together
%MaxR: Maximum Separation between the first neighbor to be evaluated
 x=FirstNeihbourInfo(Labels,MinL,mT);
x(:,4)=x(:,3)-x(:,2);
x=sortrows(x,4); i=1; mt=x(i,4); [n,~]=size(x);
while mt<MinL && i<n
   i=i+1;    mt=x(i,4);
end
if i>1, x(1:i-1,:)=[]; end
CT=zeros(1,1);
pc=1;
for i=1:length(x)
Li=x(i,1); Ti=x(i,2); Te=x(i,3);   % selecting Particle
r=r1(Ti:Te,Li);        % r separation of pairs
[rk,rm]=auto_correlation(r);
rk(rk<0.01)=[]; n=length(rk); CT(pc,1)=rm; CT(pc,2:n+1)=rk; pc=pc+1;
end
CT=DeleteRows(CT,MinL,MaxR);
%delete pairs data tracked for length smaller than MinL or with initial
%separation greater than MaxR
tc = Decaytime(CT);
rm=CT(:,1); CT(:,1)=[];
end
%%
function [rk,rm]=auto_correlation(r)
% computing auto-correlation of pairs
%r=time sequence of pair separation.
```

```matlab
%rm mean pair separation
n=length(r); rm=mean(r); rk=zeros(1,n);
for k=0:n-1
    s1=r(1:n-k)-rm;   s2=r(1+k:n)-rm;   s1=s1.*s2;   rk(k+1)=sum(s1);
end
rk=rk./rk(1);
end
 function x=DeleteRows(x,MinL,MaxR)
x=sortrows(x,1); [n,~]=size(x); pc=0; DxR=zeros(1,1); m=1;
for i=1:n
    bc=0;   x1=x(i,:);   x1(x1==0)=[];
    if length(x1)>3
        if x1(2)~=1, bc=1; end
        if x1(3)<0.8, bc=1; end
        if length(x1)<MinL, bc=1; end
        if x1(1)>MaxR, bc=1; end
    else
        bc=1;
    end
    if bc==1
        pc=pc+1;      DxR(pc)=i;
    else
        if length(x1)>m, m=length(x1); end
    end
end
DxR(DxR==0)=[]; x(DxR,:)=[]; [n,~]=size(x);
mL=1;
for i=1:n
    xr=x(i,2:end);   xr(xr<0.01)=[];
    if mL<length(xr), mL=length(xr); end
end
x(:,mL+2:end)=[];
end
 function tc = Decaytime(CT)
[n,~]=size(CT);
tc=zeros(n,1);
```

```matlab
for i=1:n
x1=CT(i,2:end);
x1(x1==0)=[];
if length(x1)>10
    tc(i) = ExpFit(x1);
else
    tc(i)=1;
end
end
end
function tc = ExpFit(x1)
%CREATEFIT(T,X1)
%  Create a fit.
%  Data for 'untitled fit 1' fit:
%      X Input : t
%      Y Output: x1
%  Output:
%      fitresul  t : a fit object representing the fit.
%      gof : structure with goodness-of fit info.
%  See also FIT, CFIT, SFIT.
 %  Auto-generated by MATLAB on 12-Aug-2020 16:59:41
 %% Fit: 'exp fit 1'.
t=1:length(x1);
[xData, yData] = prepareCurveData( t, x1 );
 % Set up fittype and options.
ft = fittype( 'exp1' );
opts = fitoptions( 'Method', 'NonlinearLeastSquares' );
opts.Display = 'Off';
opts.Lower = [1 -Inf];
opts.StartPoint = [1 -0.0310441641821506];
opts.Upper = [1 Inf];
 % Fit model to data.
[fitresult, ~] = fit( xData, yData, ft, opts );
tc=-fitresult.b; tc=1/tc;
end
```

5. SUMMARY

We studied the motion of colloidal particles in planar flow in a variety of configurations, boundary conditions, linear/square arrangements, ordered/disordered arrangements, and particle concentrations at different flow speeds. Experiments were done to confirm the nature of symmetric hydrodynamic forces in two dimensions and to observe the signs of pairing in a disordered phase. Measurements reveal a sub-population of long-lived particle pairs in a disordered phase. To understand the pairing behavior of the particles in planar flow, we used analytical modeling and computer simulation. It is observed that the collective behavior and dispersion of particles in planar flow are dominated by pairing. We used the concept of quasiparticles to explain the collective behavior of hydrodynamically interacting particles in two dimensions. Modeling and simulation of the ordered crystalline phase identify the pairs as quasiparticles, emerging at the Dirac cones of the spectrum. In square crystals, quasiparticles stimulate supersonic pairing avalanches, bringing about the melting of the crystal. In hexagonal crystals, however, where the intrinsic threefold symmetry of the hydrodynamic interaction matches that of the crystal, the spectrum forms a flat band dense with ultra-slow, low-frequency phonons whose collective interactions induce a much sharper melting transition. Hydrodynamic phonons in the hydrodynamic crystal are analogous to vibrational phonons in solid crystals, except for the fact that singularities in the hydrodynamic spectrum occur in the middle of the Brillion zone. The emergent singularities organize the spectral bands in geometric patterns reflecting the underlying symmetry breaking. It is also found that particle density fluctuation follows the dispersion relation similar to the one-dimensional chain of particles.

Appendix I

Two-dimensional source.

If a two-dimensional flow consists of outward radial flow in all directions from a single point, this point is called a simple source. If $2\pi m$ is the rate of volumetric flow, m will be defined as the strength of the source. If u_r is the radial velocity of the fluid at distance r from the source, then the flux out of the circle of radius r is $2\pi r u_r = 2\pi m$ and the complex velocity potential for the source will be $w = -m\log(z - z_o)$.
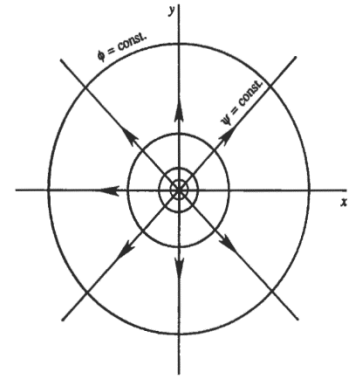
The motion of a uniform stream plus any number of sources can be expressed by the summation of corresponding complex potentials when no boundaries occur in the fluid. Thus the complex potential for a source in a uniform stream directed along the x-axis can be written as $w = -m\log z - Uz$. Hence the corresponding stream function is

$$\psi = -Uy - m\theta.$$
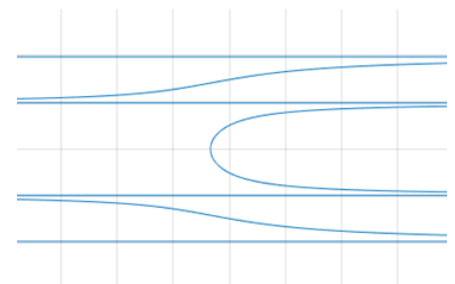
At the stagnation point where $\theta = \pi$, $y = 0$,

$\psi = -m\pi$. Therefore, the equation of streamline which passes through the stagnation point A and divides the flow into two parts is $-m\pi = -Uy - m\theta$.

At $\theta = 0$, $y = \frac{m\pi}{U} = h$.

Thus $y = h$ is an asymptote. For a flow past a half-body, due to the symmetry, there is another asymptote at $y = -h$. If the above streamline is replaced by a wall, then the complex potential above will give disturbance in the uniform flow due to the wall. The equation for the wall can be derived from the above.

$\frac{1}{x} = -\frac{1}{y}\tan\left(\frac{\pi y}{h}\right)$ and $OA = \frac{h}{\pi}$

A solid boundary inside the uniform stream described by the above equation can be equally replaced by a source of strength m.
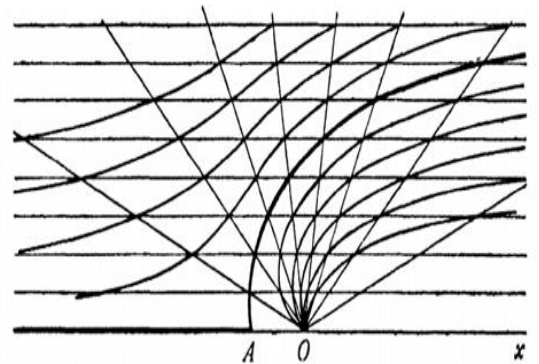
Source and equal sink in the stream

Complex potential for a source and a sink located in a uniform stream at separation $2a$ can be written as

$$w = Uz - m\log(z - a) + m\log(z + a)$$

thus

$$\frac{dw}{dz} = U - \frac{m}{z - a} + \frac{m}{z + a}$$

At the stagnation point, $\frac{dw}{dz} = 0$

$$U - \frac{m}{z - a} + \frac{m}{z + a} = 0$$

$$z = \sqrt{a^2 + \frac{2am}{U}}$$

Take $\qquad \frac{2am}{U} = b^2 - a^2 \implies z = \pm b$

Stream function for the above complex potential becomes

$$\psi = Uy - m\tan^{-1}\left(\frac{y}{x - a}\right) + m\tan^{-1}\left(\frac{y}{x + a}\right)$$

$$\psi = Uy - m\tan^{-1}\left(\frac{2ay}{x^2 + y^2 - a^2}\right)$$

We consider the streamline of $\psi = 0$ to represent the boundary where the flow of the uniform stream and the flow due to the source-sink combination cancel each other.

$$\tan\left(\frac{Uy}{m}\right) = \frac{2ay}{x^2 + y^2 - a^2}$$

$$x^2 + y^2 - a^2 = 2ay\cot\left(\frac{Uy}{m}\right)$$

This equation represents an equation of oval. Let's assume $y = c$ at $x = 0$.

$$c^2 - a^2 = 2ac\cot\left(\frac{2ac}{b^2 - a^2}\right)$$

If $a \to 0$, then $c = b$, and the oval becomes a circle of radius b. Thus when the source and sink are infinitesimally close to each other, they represent a solid circular boundary. Alternatively, flow past circular boundaries in the uniform stream can be equally replaced by the combination of source and sink that are infinitesimally close to each other. The stream function will then be written as

$$\psi = Uy - m\tan^{-1}\left(\frac{2ay}{x^2 + y^2 - a^2}\right)$$

79

Using Taylor expansion.

$$\psi = Uy - m\left(\frac{2ay}{x^2 - y^2 - a^2} + \cdots \ldots \ldots \ldots \right)$$

$$\psi = Uy - \left(\frac{U(b^2 - a^2)y}{x^2 + y^2 - a^2}\right)$$

$$\psi = Uy - \left(\frac{Ub^2 y}{x^2 + y^2}\right)$$

Velocities in x and y direction are given as

$$u_x = \frac{\partial \psi}{\partial y} = U - \left(\frac{Ub^2(x^2 - y^2)}{(x^2 + y^2)^2}\right)$$

$$u_x = U - \frac{Ub^2 \cos 2\theta}{r^2}$$

$$u_y = -\frac{\partial \psi}{\partial x} = -\left(\frac{Ub^2(2xy)}{(x^2 + y^2)^2}\right)$$

$$u_y = -\frac{Ub^2 \sin 2\theta}{r^2}$$

Appendix II

Dispersion relation along the horizontal direction

$$\dot{x}_i + \delta\dot{x}_i = -c_o \sum_{j\neq i}^{n} \frac{\left(x_{ij} + \delta x_{ij}\right)^2 - y_{ij}^2}{r_{ij}^4}$$

$$\dot{x}_i + \delta\dot{x}_i = -c_o \sum_{j\neq i}^{n} \left(\frac{x_{ij}^2 + \delta x_{ij}^2 + 2x_{ij}\delta x_{ij} - y_{ij}^2}{r_{ij}^4}\right), \quad \left(r_{ij} + \delta x_{ij}\right)^4 \sim r_{ij}^4$$

$$\dot{x}_i + \delta\dot{x}_i = -c_o \sum_{j\neq i}^{n} \left(\frac{x_{ij}^2 - y_{ij}^2}{r_{ij}^4} + \frac{2x_{ij}\delta x_{ij}}{r_{ij}^4}\right), \qquad \delta x_{ij}^2 \sim 0$$

$$\delta\dot{x}_i = -c_o \sum_{j\neq i}^{n} \left(\frac{2x_{ij}\delta x_{ij}}{r_{ij}^4}\right)$$

For the one-dimensional chain of periodic arrangement with period a and having infinite length, we can assume $r_{ij} = x_{ij} = ja$ and each δx_{ij} can be written in terms of n-nearest neighbors of ith particle on both sides.

$$\delta\dot{x}_i = -2c_o \left[\frac{\delta x_{(i+1)}}{a^3} - \frac{\delta x_{(i-1)}}{a^3} + \frac{\delta x_{(i+2)}}{(2a)^3} - \frac{\delta x_{(i-2)}}{(2a)^3} + \frac{\delta x_{(i+3)}}{(3a)^3} - \frac{\delta x_{(i-3)}}{(3a)^3} \cdots \cdots \frac{\delta x_{(i+n)}}{(na)^3} - \frac{\delta x_{(i-n)}}{(na)^3} \cdots \right]$$

Rewriting above equation

$$\delta\dot{x}_i = -2c_o \sum_{j=1}^{n} \left[\frac{\delta x_{(i+j)}}{(ja)^3} - \frac{\delta x_{(i-j)}}{(ja)^3}\right]$$

Using the plane wave equation

$$\delta x_i = A\exp\left(-i(kx_i + \omega_x t)\right)$$

$$\delta\dot{x}_i = -i\omega_x \delta x_i$$

$$i\omega_x \delta x_i = 2c_o A \sum_{j=1}^{n} \frac{\left(\exp\left(-i\left(kx_{i+j} + \omega_x t\right)\right) - \exp\left(-i\left(kx_{i+j} + \omega_x t\right)\right)\right)}{(ja)^3}$$

$$i\omega_x \delta x_i = 2c_o A \sum_{j=1}^{n} \frac{\left(\exp(-i(k(ja + x_i) + \omega_x t)) - \exp\left(-i((-kja + x_i) + \omega_x t)\right)\right)}{(ja)^3}$$

$$i\omega_x \delta x_i = 2c_o A \sum_{j=1}^{n} \frac{(\exp(-ikja) - \exp(ikja))}{(ja)^3} \exp(-i(kx_i + \omega_x t))$$

$$\omega_x = 4c_o \sum_{j=1}^{n} \frac{(\exp(-ikja) - \exp(ikja))}{i(ja)^3}$$

$$\omega_x = -\frac{6C_s}{\pi^2 a} \sum_{j=1}^{n} \frac{\sin(jka)}{j^3}. \quad \text{Here, } c_o = \left(\frac{3a^2}{2\pi^2}\right) C_s$$

Dispersion relation along the vertical direction

$$\dot{y}_i = -c_o \sum_{j \neq i}^{n} \left(\frac{\sin(2\theta_{ij})}{r_{ij}^2}\right) = -2c_o \sum_{j \neq i}^{n} \left(\frac{x_{ij} y_{ij}}{r_{ij}^4}\right)$$

$$\dot{y}_i + \delta\dot{y}_i = -2c_o \sum_{j \neq i}^{n} \left(\frac{x_{ij}(y_{ij} + \delta y_{ij})}{r_{ij}^4}\right)$$

$$\delta\dot{y}_i = -2c_o \sum_{j \neq i}^{n} \left(\frac{x_{ij} \delta y_{ij}}{r_{ij}^4}\right)$$

For the one-dimensional chain of periodic arrangement with period a and having infinite length, we can assume $r_{ij} = x_{ij} = ja$ and each δy_{ij} can be written in terms of n-nearest neighbors of ith particle on both sides.

$$\delta\dot{y}_i = -2c_o \left[\frac{\delta y_{(i+1)}}{a^3} - \frac{\delta y_{(i-1)}}{a^3} + \frac{\delta y_{(i+2)}}{(2a)^3} - \frac{\delta y_{(i-2)}}{(2a)^3} + \frac{\delta y_{i+3}}{(3a)^3} - \frac{\delta y_{(i-3)}}{(3a)^3} \dots \dots \frac{\delta y_{(i+n)}}{(na)^3} - \frac{\delta y_{(i-n)}}{(na)^3} \dots \right]$$

$$\delta\dot{y}_i = -2c_o \sum_{j=1}^{n} \left(\frac{\delta y_{(i+j)}}{(ja)^3} - \frac{\delta y_{(i-j)}}{(ja)^3}\right)$$

Using the plane wave equation,

$$\delta y_i = A \exp\left(-i(ky_i - \omega_y t)\right)$$

$$\omega_y = \frac{6C_s}{\pi^2 a} \sum_{j=1}^{n} \frac{\sin(jka)}{j^3}$$

Fourier expansion

$\omega_y = \frac{6C_s}{\pi^2 a} \sum_{j=1}^{N} \frac{\sin(jka)}{j^3}$

Fourier expansion for periodic function $f(x)$ with period L can be written as

$f(x) = \frac{a_o}{2} + \sum_n a_n \cos\left(\frac{n\pi}{L} x\right) + b_n \sin\left(\frac{n\pi}{L} x\right)$

Comparing the above two equations,

$$a_o = 0, \qquad a_n = 0, \qquad b_n = \frac{6C_s}{\pi^2 a}\left(\frac{1}{n^3}\right), \qquad \frac{\pi x}{L} = ka$$

If we assume, $x = \frac{ka}{2\pi}$, then $L = \frac{1}{2}$.

$f(x)$ can now be rewritten assuming $\frac{6C_s}{\pi^2 a} = A$

$f(x) = A \sum_n \sin\frac{(2\pi n x)}{n^3}$

The above function has a period of $L = 1/2$. Its plot for the first 100 terms in the range $0 < x < \frac{1}{2}$ is shown in Fig. (1) along with a polynomial fit.

Fitting model

$$f(x) = ax^3 + bx^2 + cx + d$$

$a = \quad 20.67 \ (20.67, 20.67)$

$b = \quad -31.01 \ (-31.01, -31.01)$

$c = \quad 10.34 \ (10.34, 10.34)$

$d = -1.475e - 06$

In simplified form,

$$f(x) = 10.34(Ax)(1 - 3x + 2x^2)$$

$$f(x) = C_s \left(\frac{2\pi x}{a}\right)(1 - 3x + 2x^2)$$

Substituting for $x = \frac{ka}{2\pi}$

$$f(x) = C_s k \left(1 - 3\left(\frac{ka}{2\pi}\right) + 2\left(\frac{ka}{2\pi}\right)^2\right) = \frac{6C_s}{\pi^2 a}\sum_n \sin\frac{(nka)}{n^3}$$
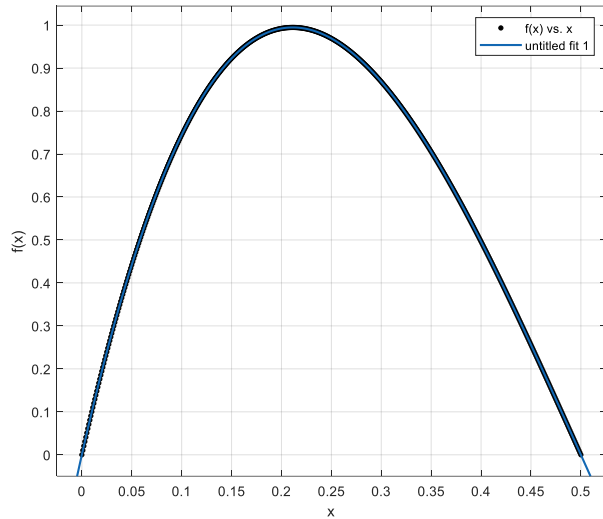

Fig. (1): plot for Eq. (3) and its polynomial fit

$$\omega = C_s k \left(1 + 2\left(\frac{ka}{2\pi}\right)^2 - 3\left(\frac{ka}{2\pi}\right)\right)$$

If we assume $C_s = 1, \ a = 1,$

$$C_s = \frac{2\pi^2}{3}\frac{c_0}{a^2} = 1, \qquad c_o = \frac{3}{2\pi^2}$$

$$\omega = k \left(1 + 2\left(\frac{k}{2\pi}\right)^2 - 3\left(\frac{k}{2\pi}\right)\right)$$

Appendix III

Matrix equation (1D).

In the carrier frame

$$\dot{x}_i = -c_o \sum \frac{1}{x_{ij}^2}$$

$$\frac{\partial \dot{x}_1}{\partial x_1} = \frac{3}{\pi^2} \sum \frac{1}{x_{1j}^3} \frac{\partial x_{1j}}{\partial x_1}$$

$$\frac{\partial \dot{x}_1}{\partial x_j} = \frac{3}{\pi^2} \frac{1}{x_{1j}^3} \frac{\partial x_{1j}}{\partial x_j}$$

$$\delta \dot{x}_1 = \frac{3}{\pi^2} \left[\left(\sum \frac{1}{x_{1j}^3} \right) \delta x_1 + \frac{1}{x_{12}^3} \delta x_2 + \frac{1}{x_{13}^3} \delta x_3 \ldots \right]$$

$$\delta \dot{x}_2 = \frac{3}{\pi^2} \left[\frac{1}{x_{12}^3} \delta x_1 + \left(\sum \frac{1}{x_{2j}^3} \right) \delta x_2 + \frac{1}{x_{23}^3} \delta x_3 \ldots \right]$$

$$\delta \dot{x}_3 = \frac{3}{\pi^2} \left[\frac{1}{x_{13}^3} \delta x_1 + \frac{1}{x_{23}^3} \delta x_2 + \left(\sum \frac{1}{x_{3j}^3} \right) \delta x_3 \ldots \right]$$

Matrix form

$$\begin{bmatrix} \delta \dot{x}_1 \\ \delta \dot{x}_2 \\ \delta \dot{x}_3 \\ \cdot \\ \cdot \end{bmatrix} = \frac{3}{\pi^2 \begin{bmatrix} \left(\Sigma \frac{1}{x_{1j}^3} \right) & \frac{1}{x_{12}^3} & \frac{1}{x_{13}^3} & \cdot & \cdot \\ \frac{1}{x_{12}^3} & \left(\Sigma \frac{1}{x_{2j}^3} \right) & \frac{1}{x_{23}^3} & \cdot & \cdot \\ \frac{1}{x_{13}^3} & \frac{1}{x_{23}^3} & \left(\Sigma \frac{1}{x_{3j}^3} \right) & \cdot & \cdot \\ \cdot & \cdot & \cdot & \cdot & \cdot \\ \cdot & \cdot & \cdot & \cdot & \cdot \end{bmatrix}} \begin{bmatrix} \delta x_1 \\ \delta x_2 \\ \delta x_3 \\ \cdot \\ \cdot \end{bmatrix}$$

References.

1. Sir Horace Lamb, Hydrodynamics (1879).

2. L.M. Milne-Thomson, Theoretical Hydrodynamics, (1962).

3. Happel and H. Brenner, Low Reynolds Number Hydrodynamics (1969).

4. J. K. G. Dhont, An Introduction to Dynamics of Colloids, Elsevier, Amsterdam, (1996).

5. Sangtae Kim and Seppo J. Karrila Microhydrodynamics Principles and Selected Application (1991).

6. M. Stimson and G. B. Jeffery, Proc. Roy. Soc. (London) A111, (1926) 110.

7. Smoluchowski, M. Bull. Inter. Acad. Polonaise sci Lett. lA, (1911) 28.

8. Raymond G. Cox and Howard Brenner, Chem. Eng. Sci, (1967) 22, 1752-1777.

9. Tamada, K., and H. Fujikawa, Quart, J. Phys. Soc. Japan, (1959) 14, 2, 202-216.

10. John Happel, A.I.Ch.E, (1957) 4, 2, 197-201.

11. John Happel, A.I.Ch.E, (1960) 6, 1, 129-133.

12. L.D. Reed and F.A. Morrison Jr., Int. J. Multiphase Flow, (1974) 1, 573-584.

13. Y. Grasseli and L. Lobry, Physics of Fluids, (1997) 9, 3929-3931

14. Jesus Santana-Solano, Angeles Ramirez-Saito, and Jose Luis Arauz-Lara, PRL, (2005) 95, 198301.

15. J.C. Meiners and S.R. Quake, Phy. Rev. Lett., (1999) 82, 10, 2211.

16. Boaz A.Nemet, Mark Cronin-Golomb, Opt. Lett., (2002) 27, 15, 1357-1359.

17. R.C Hidalgo, A. Goni-Arana, Phy. Rev.E, (2018) 97, 012611.

18. Arash Nikoubashman, Christos N. Likos and Gerhard Kahl Soft Matter, (2013) 9, 2603-2613.

19. J.C. Crocker, J. Chem. Phys., (1997) 106, 7, 2837.

20. Bianxiao Cui, Haim Diamant, Binhua Lin, and Stuart A. Rice, PRL, (2004) 92, 25, 258301.

21. B. Bonilla-Capilla, A. Ramírez-Saito, M. A. Ojeda-Lopez and J. L. Arauz-Lara, J. Phys.: Condens. Matter, (2012) 24, 464126.

22. K. O. L. F. Jayaweera, B. J. Mason and G. W. Slack, J. Fluid Mech., (1964) 20, 1, 121-128.

23. M. L. Ekiel-Jeżewskaa and B. U. Felderhof, Phys. Fluids, (2005) 17, 093102.

24. Yulia Sokolov, Derek Frydel, David G. Grier, Haim Diamant, and Yael Roichman, PRL, (2011) 107, 158302.

25. Yasuyuki Kimura, J. Phy. Soc. Japan, (2017) 86, 101003.

26. Michael Reichert and Holger Stark J. Phy: Condens. Matter, (2004) 16, S4085=S4094.

27. Tsevi Beatus, Tsvi Tlusty, and Roy Bar-Ziv, Nat. Phys, (2006) 2, 743.

28. Tsevi. Beatus, Tsvi. Tlusty and R. Bar-Ziv, Phys. Rev. Lett. (2009) 103, 114502.

29. Tsevi Beatus, Roy Bar-Ziv and Tsvi Tlusty, PRL, (2007) 99, 124502.

30. Tsevi Beatus, Roy H.Bar-Ziv and Tsvi Tlusty. Phys Reports, (2012) 516, 103-145.

31. Yael Roichman and David G. Grier, Phy. Rev. E, (2007) 75, 020401.

32. M. Baron, J. Bławzdziewicz, and E. Wajnryb, PRL, (2008) 100, 174502.

33. Alan Cheng Hou Tsang, Michael Shelley, and Eva Kanso, Soft Matter, (2018) 14, 945-950.

34. Stuart Henderson, Steven Mitchell, and Paul Bartlett. PRL (2002), 88, 088302.

35. J. Hansen and I.McDonald, Theory of simple liquids, Academic Press, London, (1986).

36. Slichter, C. S., "Theoretical Investigation of the Motion of Ground Waters," U. S. Geological Survey, 19th Ann. Rep., Part 2 (1899), pp. 301-384.

37. H. A. Lorentz, A general theorem concerning the motion of a viscous fluid and a few consequences derived from it. In: H. A. Lorentz Collected Works, Vol. IV The Hague: Martinus Nijhoff Publishers (1937) pp. 7-14.

38. Ladenburg, R. Ann. d. Phys. 23 (1907), 447.

39. Cunningham, E. Proc. Roy. Soc. (London) A83 (1910), 357.

40. Einstein, Ann. Physik 19 (1906), 289; with correction 34 (1911) 591.

41. Oseen, Hydrodynamik. Leipzig: Akademische Verlag, 1-27.

42. Smoluchowski, M. Bull. Intern. acado polonaise sci. lettres, lA (1911), 28.

43. Guth, E., Proc. International Congr. Appl. Mech. (1938), pp. 448-55.

44. D. Myksyn, D. Sc., Solution of Oseen Equation for an Inclined Elliptic Cylinder in Viscous Fluid (1937).

45. Dean, W. R., Proc. Camb. Phil. Soc. 40 (1944), 19.

46. Hasimoto, Journal of Fluid Mechanics, Volume 5, Issue 2, February (1959) pp. 317 – 328.

47. Howard Brenner, Chemical Engineering Science, (1962) Vol. 17, pp. 435446.

48. Dr. G. Segre and Dr A. Silberberg, Nature, Jan 21 (1961) Vol. 189.

49. R. G. Cox and H. Brenner, J.Fluid Mech. (1967), vol. 28, part 2.

50. M. E. O'Neill, Proc. Camb. Phil. Soc. (1969), 65, 543.

51. G. Is. Batchelor and J. T. Green, J. Fluid Mech. (1972), vol. 56, part 2, pp. 375-400.

52. N. Liron and S. Mochon, Journal of Engineering Mathematics, Vol. 10, No. 4, (1976).

53. P. Vasseur and R. G. Cox, J. Fluid Mech. (1977), vol. 80, part 3, p . 561-591.

54. Sangtae Kim, The Physics of Fluids 30, 2309 (1987); Doi: 10.1063/1.866120.

55. J. C. Meiners and Stephen R. Quake, PRL, (1999) 82 10, 2211-2214.

56. Eric R. Dufresne, et al., PRL, (2000) 85 15, 3317-3320.

57. Yujun Song, Daojian Cheng, Liang Zhao, Microfluidics: Fundamental, Devices and Applications.

58. Xiujun James Li, Yu Zhou, Microfluidic Devices for Biomedical Applications, Elsevier Science.

59. Hamed Amini, et al., Inertial microfluidic physics, Lab on Chip, 15 (2004).

60. Qikun Wang, Dan Yuan Weihua Li, Micromachines (2017) 8, 197; doi:10.3390/mi8070197

61. R. Di Leonardo, et al., Phys. Rev. E 78, 031406 (2008).

62. Harel Nagar and Yael Roichman, Phys. Rev. E 90, 042302 (2014).

63. Landau, L. Theory of the Superfluidity of Helium II. Phys. Rev. 60, 356–358 (1941).

64. Efremov, D. V. et al. Multicritical Fermi Surface Topological Transitions. Phys. Rev. Lett. 123, 207202 (2019).

65. Shtyk, A., Goldstein, G. & Chamon, C. Electrons at the monkey saddle: A multicritical Lifshitz point. Phys. Rev. B 95, 035137 (2017).

66. Kopnin, N. B., Heikkila, T. T. & Volovik, G. E. High-temperature surface superconductivity in topological flat band systems.

67. Isobe, H., Yuan, N. F. Q. & Fu, L. Unconventional Superconductivity and Density Waves in Twisted Bilayer Graphene. Phys. Rev. X 8, 041041 (2018).

68. Marchenko, D. et al. Extremely flat band in bilayer graphene. Sci Adv 4, eaau0059 (2018)

69. Gofron, K. et al. Observation of an "Extended" Van Hove Singularity in YBa2Cu4O8 by Ultrahigh Energy Resolution Angle-Resolved Photoemission. Phys. Rev. Lett. 73, 3302-3305 (1994)

70. McChesney, J. L. et al. Extended van Hove singularity and superconducting instability in doped graphene. Phys. Rev. Lett. 104, 136803 (2010).

71. Goldman, A. J., Cox, R. G. & Brenner, H. The slow motion of two identical arbitrarily oriented spheres through a viscous fluid. Chem. Eng. Sci. 21, 1151-1170 (1966)

72. Sarig, I., Starosvetsky, Y. & Gat, A. D. Interaction forces between microfluidic droplets in a Hele-Shaw cell. J. Fluid Mech 800, 264-277 (2016).

73. W¨olfle, P. Quasiparticles in condensed matter systems. Rep. Prog. Phys. 81, 032501 (2018).

74. Bistritzer, R. & MacDonald, A. H. Moir bands in twisted double-layer graphene. Proc. Natl. Acad. Sci. USA 108, 12233-12237 (2011)

75. Mao, J. et al. Evidence of flat bands and correlated states in buckled graphene superlattices. Nature 584, 215-220 (2020).

76. Beatus, T., Shani, I., Bar-Ziv, R. H. & Tlusty, T. Two dimensional flow of driven particles: a microfluidic pathway to the non-equilibrium frontier. Chem. Soc. Rev. 46, 5620-5646 (2017).

77. Shankar, S., Souslov, A., Bowick, M. J., Marchetti, M. C. & Vitelli, V. Topological active matter. arXiv:2010.00364 (2020).

78. Bowick, M. J., Fakhri, N., Marchetti, M. C. & Ramaswamy, S. Symmetry, thermodynamics, and topology in active matter. arXiv:2107.00724 (2021).

79. Ivlev, A. V. et al. Statistical Mechanics where Newton's Third Law is Broken. Phys. Rev. X 5, 011035 (2015).

80. You, Z., Baskaran, A. & Marchetti, M. C. Nonreciprocity as a generic route to traveling states. Proc. Natl. Acad.Sci. USA 117, 19767-19772 (2020).

81. Meredith, C. H. et al. Predator-prey interactions between droplets driven by non-reciprocal oil exchange. Nature Chemistry 12, 1136-1142 (2020).

82. Jee, A.-Y., Cho, Y.-K., Granick, S. & Tlusty, T. Catalytic enzymes are active matter. Proc. Natl. Acad. Sci. USA 115, E10812 (2018).

83. Champagne, N., Lauga, E., Bartolo, D. Soft Matter 7 (23), 11082, 2011.

Acknowledgment

I am extremely grateful to my esteemed supervisors, **Prof. Hyuk Kyu Pak** and **Prof. Tsvi Tlusty** for their continuous support, guidance, and patience during my Ph.D. study. Their immense knowledge and plentiful experience have encouraged me in all the time of my academic research. I would like to thank my friends, lab mates, and colleagues for the cherished time we spent together in the lab, and in social settings. I am also thankful to **Dr. Issac Michael** and **Prof. Yoon-Kyoung Cho** for their essential help in constructing the microfluidic channels. I am grateful to **Mr. Ki-Bom Nam** for his guidance in building the holographic optical tweezer.

I am thankful to the professional staff members of **IBS-CSLM**, for their cooperation in assisting with my experimental setup and administrative matters.

Finally, I would like to express my gratitude to my wife and my children. Without their tremendous understanding and encouragement over the past few years, it would be impossible for me to complete my study.